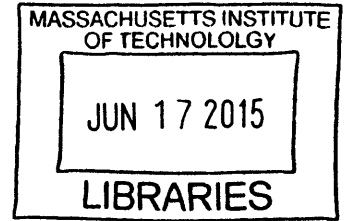Composition, Structure, and Performance of Nanocrystal Bulk Heterojunction Photovoltaics

by

Kevin J. Huang

B.S., Cornell University (2006)
M.S., University of Illinois, Urbana-Champaign (2007)

Submitted to the Department of Materials Science and Engineering in Partial Fulfillment of the
Requirements for the Degree of

Doctor of Philosophy

at the

MASSACHUSETTS INSTITUTE OF TECHNOLOGY

June 2015

Signature of Author ....
Department of Materials Science and Engineering
February 12, 2015

Certified by ....
Paula Hammond
David H. Koch Professor in Engineering
Thesis Supervisor

Accepted by ....
Angela Belcher
Professor, Biological Engineering and Materials Science and Engineering
Thesis Reader

Accepted by ....
Donald R. Sadoway
Chair, Departmental Committee on Graduate Students

1

Composition, Structure, and Performance of Nanocrystal Bulk Heterojunction Photovoltaics

by

Kevin J. Huang

Submitted to the Department of Materials Science and Engineering on February 12, 2015 in partial fulfillment of the requirements for the degree of Doctor of Philosophy in Materials Science and Engineering

ABSTRACT

We describe the fabrication and study of bulk heterojunction solar cells composed of PbS quantum dots and TiO_2. In particular, we study the effects that bulk heterojunction composition and structure have on resulting device performance.

We find that PbS and titania are extremely evenly distributed throughout our bulk heterojunction devices, such that charge carriers generated anywhere within the blend are well within a carrier collection length of the charge separating driving force required to separate them and enable their collection. Of the compositions we studied, we found that devices with a TiO_2-rich bulk heterojunction composition outperformed devices employing other compositions. As a result of the size difference between the PbS quantum dots and the titania nanocrystals which compose the blends, the likelihood of forming a truly complete, bicontinuous bulk heterojunction network is maximized at a TiO_2-rich blend composition.

We find that diffuse interfaces exist between adjacent layers of our devices as a result of interfacial surface roughness. Rather than being deleterious, this increased interfacial area extends the spatial extent of the depletion region over a greater volume of our devices. Our bulk heterojunction blends form well packed, high density binary particle mixtures, particularly at a TiO_2-rich composition. Device efficiency was maximized for bulk heterojunctions employing the smallest titania nanocrystals, an indication that at constant volume fractions, larger titania nanocrystals decrease the total number of titania particles available to form complete and continuous pathways through the depth of the bulk heterojunction. Furthermore, a peak in device performance was observed at intermediate blend layer thicknesses. This results from the balance between two opposing effects: an increase in light absorption and photocurrent with thicker bulk heterojunctions and an increased likelihood of charge carrier recombination with thicker bulk heterojunctions.

Finally, enhanced light absorption and current generation was observed at red and infrared wavelengths, validating the ability of bulk heterojunctions to spatially extend the reach of the charge separating driving force, such that the previously missed red and infrared photons may be captured.

Thesis Supervisor: Paula Hammond
Title: David H. Koch Professor in Engineering

Acknowledgments

Table of Contents

Table of Figures

Chapter 1: Introduction and Motivation

Energy has been a part of human society ever since the very beginning. Global primary energy consumption in 2013 was 533 EJ, up from 27.4 EJ in 1850 [1, 2], an increase of over 1800%. During the same time period, the world's population grew by "only" 460% [3]. As can be seen by the large disparity in growth rates, we as a society are consuming ever growing amounts of energy per person. Accordingly, methods and technologies for capturing, converting, storing, distributing, and consuming energy will only continue to increase in importance to match our simultaneously and ever increasing thirst for energy.

Presently, however, the vast majority of our energy is supplied from sources that are non-renewable and finite. These resources are also not evenly distributed around the world. Moreover, it is clear that our reliance on carbon-based sources of energy is causing extremely rapid and increasingly irreversible large scale changes to our climate. These factors, among others, are driving interest toward the development of novel and sustainable ways of producing energy, whether it's out of fear that our resources will soon run out, fear that our domestic sources of energy will dwindle and make us politically and economically reliant on foreign nations (not necessarily of our own choosing), or fear that we are forever damaging our world in ways that will last for centuries to come and may not be reversible.

Energy is a massive industry. With the global market estimated at a size of $6 trillion, energy is the third largest industry in the United States [4]. Aside from the clear financial and economic opportunity to capitalize on emerging technologies and business models for such a large industry, there's also an undercurrent of national competition that often pervades the discussion around "American" or "domestic" energy. And in the race to maintain leadership in the global economy, and by extension global politics, leadership in energy is a promising pathway.

This sort of nationalistic rhetoric can be particularly acute when oil prices are high, as they were in the summer of 2008 when oil was priced at over $140 per barrel [5] given that much of our nation's oil is imported, often from nations mired by political instability. Beyond oil, the security of our national electric power transmission and distribution grids is also of concern. Blackouts can result in significant economic loss while there's evidence that our national infrastructure, such as the power grid, is susceptible to attack [6]. And recent events unfolding in the Ukraine have once again shine a spotlight on the Russian supply of natural gas to Europe and the associated supply and security concerns that accompany that dependent relationship. National security or national "competitiveness" remains a driving force behind the development of new domestic and sustainable energy solutions.

But perhaps the greatest concern that is motivating (or should be motivating) a transition to more sustainable sources of energy is climate change. At the start of the industrial revolution, the atmospheric CO_2 concentration was approximately 280 ppm by volume. Largely as a result of human reliance on carbon based sources of energy that emit excessive amounts of CO_2, a long lifetime greenhouse gas, atmospheric CO_2 concentrations have already passed 400ppm. CO_2 concentrations haven't been this high in at least 800,000 years, if not upwards of 15 million years [7]. As a consequence of this, global mean surface temperatures continue to rise to unprecedented levels. With high confidence, this has and will continue to have numerous physical and environmental effects:

1. Dramatic increase in global average surface temperature

2. Decreased global snow and sea ice cover as well as decreased glaciation

3. Rising sea levels

4. Increased ocean acidification

5. Decreased ocean oxygenation

6. More extreme weather (dry and drought stricken regions will be more so, areas vulnerable to high precipitation events will be even more affected by them)

7. Increased fire frequency and intensity in vulnerable areas

8. Destabilization of gas hydrate and permafrost-based methane deposits (i.e., further release of methane)

From these effects, it is not difficult to extrapolate the severe impacts this will have on ecosystems around the world as well as on human society, particularly on food security and supply [8], water availability, human health [9], human conflict, human conflict with other animal species, the built environment and man-made infrastructure, and human industry. Climate change is unique in that it remains a challenge that affects not just some parts of society (e.g., only some geographic regions, only some socio-economic classes, or only some ethnicities), but all of it. And as a consequence, its impacts are so far ranging that estimation, quantification, and projection of all of them remains an ongoing process. Figure 1 presents some, but certainly not all, likely impacts of climate change on human society. Far from being a widely divided, the majority of climate scientists believe that climate change is largely caused by humans, that it imposes significant risks, and that immediate efforts should be taken to curb the emissions of greenhouses gases into the atmosphere [10].

Table 3.2. Examples of possible impacts of climate change due to changes in extreme weather and climate events, based on projections to the mid- to late 21st century. These do not take into account any changes or developments in adaptive capacity. The likelihood estimates in column two relate to the phenomena listed in column one. {WGII Table SPM.1}

Phenomenon[a] and direction of trend	Likelihood of future trends based on projections for 21st century using SRES scenarios	Examples of major projected impacts by sector			
		Agriculture, forestry and ecosystems {WGII 4.4, 5.4}	Water resources {WGII 3.4}	Human health {WGII 8.2, 8.4}	Industry, settlement and society {WGII 7.4}
Over most land areas, warmer and fewer cold days and nights, warmer and more frequent hot days and nights	*Virtually certain*[b]	Increased yields in colder environments; decreased yields in warmer environments; increased insect outbreaks	Effects on water resources relying on snowmelt; effects on some water supplies	Reduced human mortality from decreased cold exposure	Reduced energy demand for heating; increased demand for cooling; declining air quality in cities; reduced disruption to transport due to snow, ice; effects on winter tourism
Warm spells/heat waves. Frequency increases over most land areas	*Very likely*	Reduced yields in warmer regions due to heat stress; increased danger of wildfire	Increased water demand; water quality problems, e.g. algal blooms	Increased risk of heat-related mortality, especially for the elderly, chronically sick, very young and socially isolated	Reduction in quality of life for people in warm areas without appropriate housing; impacts on the elderly, very young and poor
Heavy precipitation events. Frequency increases over most areas	*Very likely*	Damage to crops; soil erosion, inability to cultivate land due to waterlogging of soils	Adverse effects on quality of surface and groundwater; contamination of water supply; water scarcity may be relieved	Increased risk of deaths, injuries and infectious, respiratory and skin diseases	Disruption of settlements, commerce, transport and societies due to flooding: pressures on urban and rural infrastructures; loss of property
Area affected by drought increases	*Likely*	Land degradation; lower yields/crop damage and failure; increased livestock deaths; increased risk of wildfire	More widespread water stress	Increased risk of food and water shortage; increased risk of malnutrition; increased risk of water- and food-borne diseases	Water shortage for settlements, industry and societies; reduced hydropower generation potentials; potential for population migration
Intense tropical cyclone activity increases	*Likely*	Damage to crops; windthrow (uprooting) of trees; damage to coral reefs	Power outages causing disruption of public water supply	Increased risk of deaths, injuries, water- and food-borne diseases; post-traumatic stress disorders	Disruption by flood and high winds; withdrawal of risk coverage in vulnerable areas by private insurers; potential for population migrations; loss of property
Increased incidence of extreme high sea level (excludes tsunamis)[c]	*Likely*[d]	Salinisation of irrigation water, estuaries and fresh-water systems	Decreased fresh-water availability due to saltwater intrusion	Increased risk of deaths and injuries by drowning in floods; migration-related health effects	Costs of coastal protection versus costs of land-use relocation; potential for movement of populations and infrastructure; also see tropical cyclones above

Notes:
a) See WGI Table 3.7 for further details regarding definitions.
b) Warming of the most extreme days and nights each year.
c) Extreme high sea level depends on average sea level and on regional weather systems. It is defined as the highest 1% of hourly values of observed sea level at a station for a given reference period.
d) In all scenarios, the projected global average sea level at 2100 is higher than in the reference period. The effect of changes in regional weather systems on sea level extremes has not been assessed. {WGI 10.6}

Figure 1. Example of some, but not all, likely human impacts of climate change [10].

One of the best ways of achieving this is to transition our global economy to non-carbon, sustainable sources of energy [11], as presently, fossil fuel use pervades our society. Coal comprised about 37% of net electricity generation for all sectors in the United States in 2014. Natural gas, another fossil fuel, composed about another 27%. The remainder was generated from nuclear (~19%) and various renewable energy technologies, predominantly conventional hydroelectric and wind [12]. Furthermore, of the approximately 253 million vehicles in the United States (as of 2011) [13], only about 68,000 don't rely on fossil fuels for propulsion (this does not include the approximately 2 million hybrid electric vehicles, which still partially rely on gasoline) [14].

Why Solar Energy

Of the various available non-carbon sustainable energy technologies, solar power may be the most appealing. It provides an unlimited supply of non-carbon energy, delivering over 4.3×10^{20} J of energy to earth every hour, significantly more than we consume in an entire year [15]. The extreme magnitude of this difference is illustrated in Figure 2. The global annual resource potential of solar energy is nearly 4 million EJ, which dwarfs, by several orders of magnitude, those of wind (>2,000 EJ) and biomass energy (~200 EJ). Further, it is vastly more energy that is consumed by the global population (~500-600 EJ) each year.
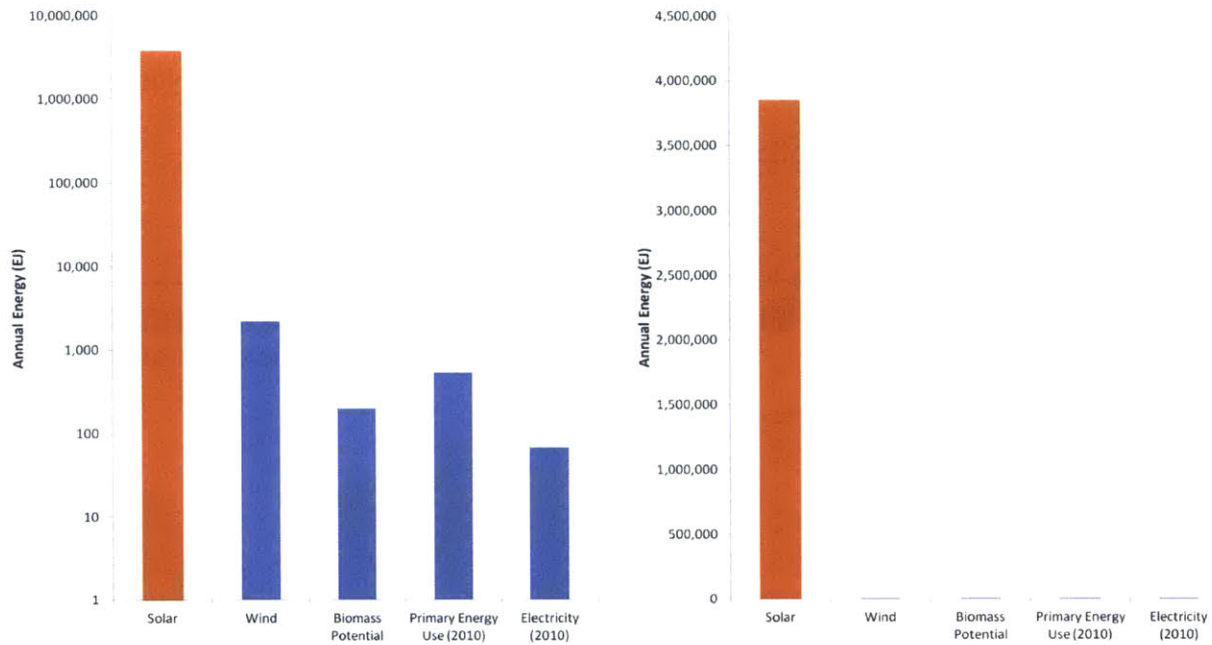
Figure 2. Global annual resource potential for various renewable energy technologies compared with global annual primary energy use and annual electricity use in 2010 [16-20].

The enormous availability of solar energy can be illustrated another way. Figure 3 presents a solar resource map of the United States, visually indicating how much sunlight is available for capture each day in the US. In the desert southwest, over 6 kWh/m^2 is available for capture, on average, each day. Put another way, 1.6% of the total US land area could generate enough energy from 10% efficient solar cells to supply energy for the entire United States [21]. Not limited to just the United States, solar energy is widely available around the world as well. For instance, Germany leads the world in total installed capacity of solar photovoltaics (described in more depth later) [22], despite having a solar resource potential comparable to that of Alaska (see Figure 4). Thus, while there are many regions around the world with extremely high levels of incident solar radiation of which they can take advantage (e.g., US southwest, Mediterranean, North Africa), such extreme resource potentials are by no means required in order to

13

meaningfully capture and use solar energy. The ubiquity of the solar resource around the world, in addition to its extremely high energy, is one of the most attractive aspects of solar energy as a candidate technology to replace polluting carbon-based energy sources.
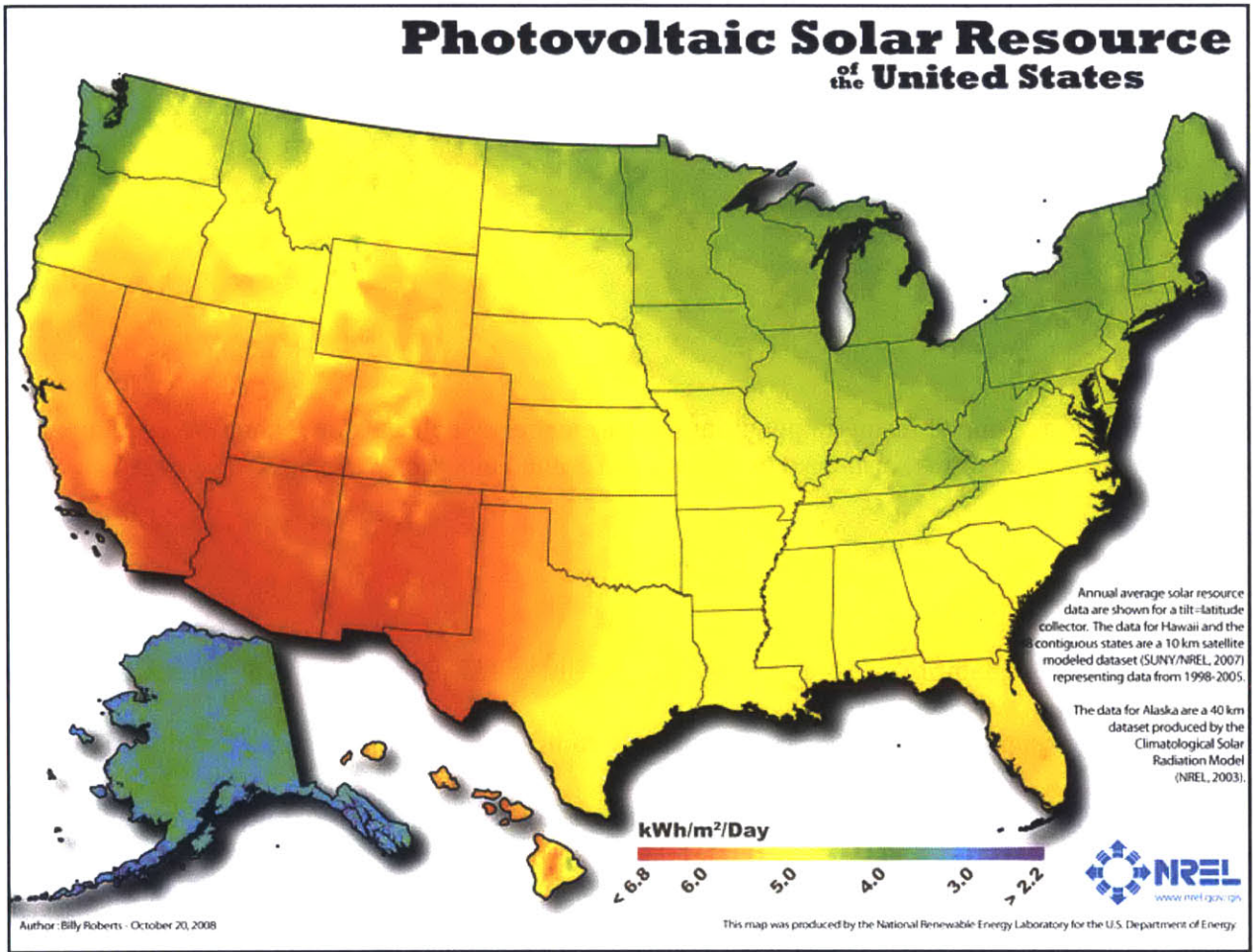
Figure 3. Solar resource potential for the United States [23].
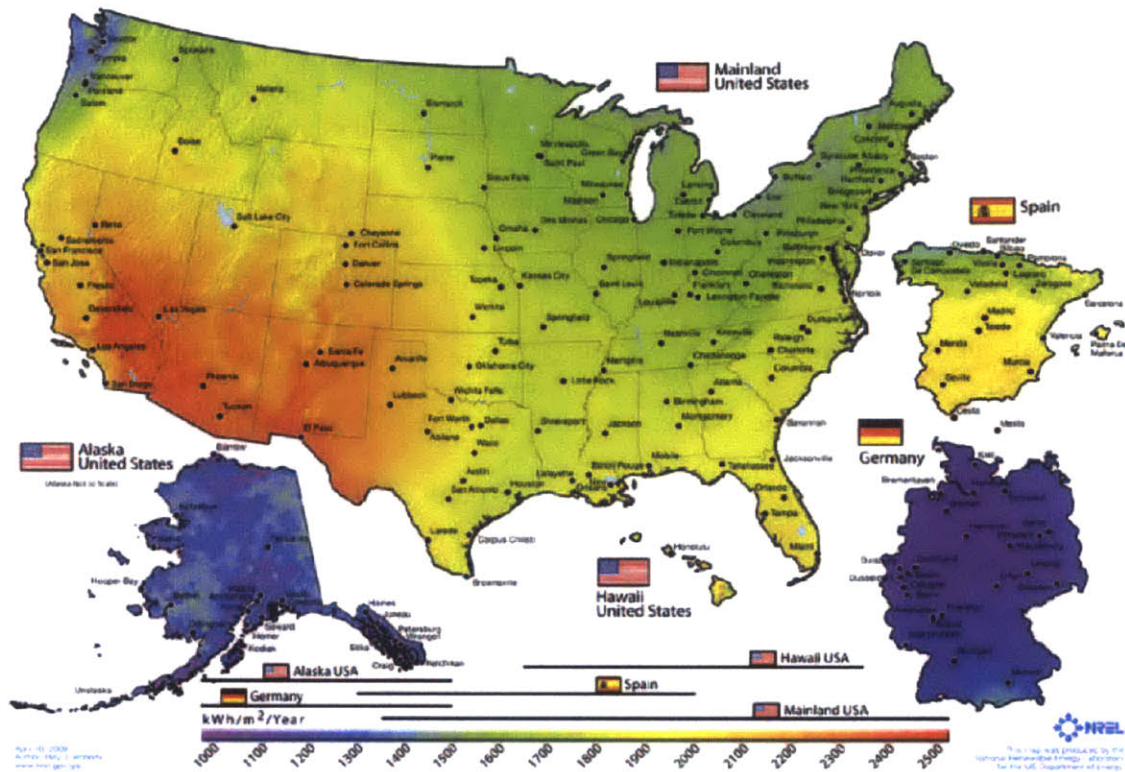
Figure 4. Solar photovoltaic resource potential for the United States, Spain, and Germany [24].

Given this massive resource potential, a wide variety of methods exist to capture and make use of incident solar radiation. The two primary methods can be categorized broadly as solar thermal and solar electricity production. The capture of solar radiation for its ability to provide heat has been used for centuries. Passive solar collectors, for instance, when placed in sunlight, can be used to directly heat air or water for use in buildings. Incident sunlight is absorbed by a material, often a darkly colored metal or other material with high thermal conductivity and visible light absorption. As it absorbs light, it heats up, subsequently transferring the heat to a suitable fluid

such as air or water, which is then transported away for use. In addition to direct use for building heating and hot water, passive solar collectors can also be used to cook food and distill water. While there's no doubt that passive solar collection and heating can have a large impact and role in a transition to a sustainable, decarbonized economy, electricity production from solar energy is perhaps even more valuable. Energy in the form of high value electricity may be used for a wide variety of applications and uses, including (but certainly not limited to) heating, cooking, and distillation. Furthermore, as a greater proportion of the world industrializes, an increasing fraction of world energy use will be carried by electricity, making the global transition to a sustainable source of electricity generation even more urgent and necessary.

Two methods exist by which to turn solar energy into electricity. Concentrated solar power (CSP) captures incident solar radiation and concentrates it through the use of lenses or mirrors to heat water or other high heat capacity fluids, the energy from which is then used to drive a steam turbine to generate electricity [25]. The three primary technologies to do this are illustrated in Figure 5. Parabolic trough CSP systems are composed of a linear series of parabolic mirrors that concentrate sunlight into a working fluid-filled tube located at the mirror's focal point. This heated fluid is used as the heat source for electricity generation. The trough itself rotates throughout the day along a single axis to track the sun's movement across the sky. By contrast, in a Stirling dish design, a single large reflective dish tracks the sun's movement along two axes. Sunlight is concentrated to the dish's focal point, where it is absorbed by a working fluid-filled receiver and used to drive a Stirling engine. Finally, like a Stirling dish CSP system, solar power towers rely on a field of mirrors (called heliostats) which also track the sun along two axes. They reflect light to a centrally located tower, atop which sits a working fluid-filled receiver that stores heat that is later used to produce electricity.
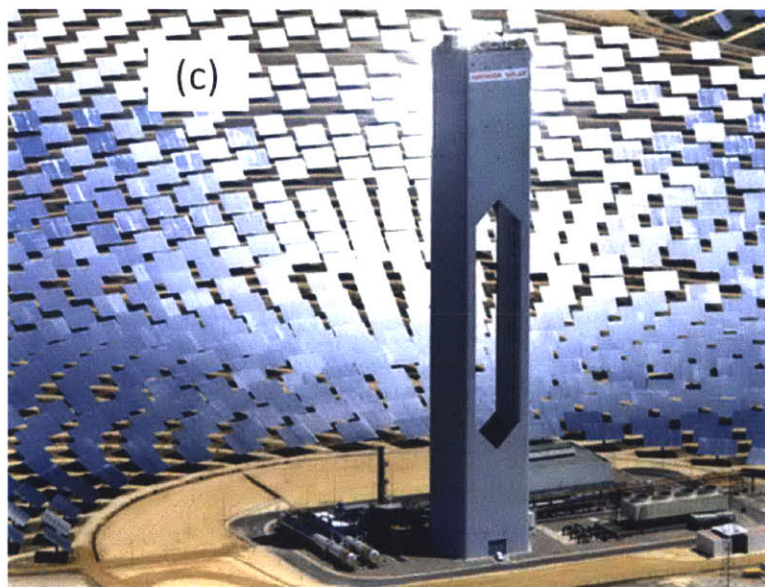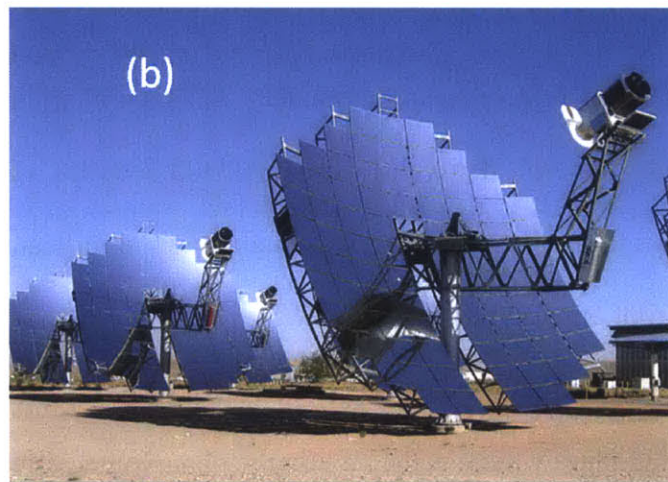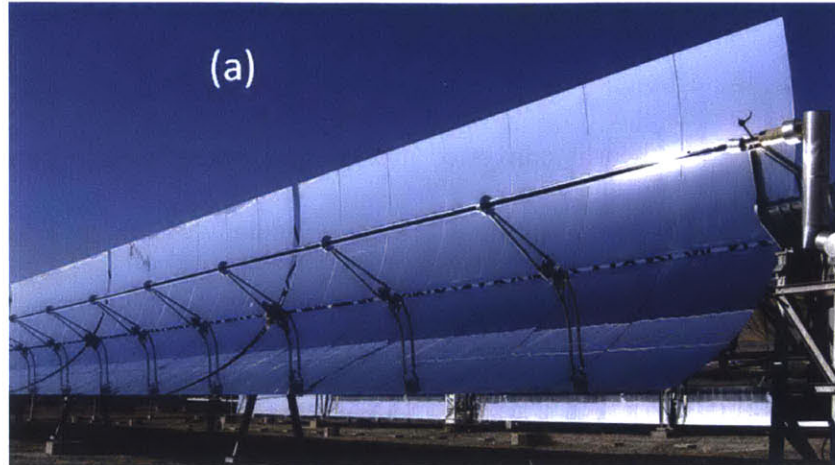
Figure 5. Various CSP technologies. (a) parabolic trough, (b) dish Stirling engine, (c) solar power tower [26-28].

The efficiency of such systems is dependent on the efficiencies of its constituent processes. This includes, for instance, the efficiency with which sunlight is converted into heat by the receiver, the efficiency with which that heat is converted into useful work, and the efficiency with which the electricity is generated from that work. While the efficiency of the work generating step is dependent on the temperature the working fluid is able to reach (which will vary), state-of-the-art CSP systems can convert sunlight to electricity with total efficiencies as high as 25% [29].

CSP, while currently being commercially deployed throughout the world to various degrees, still remains too costly, in general, to compete with current energy sources. In 2010, the levelized cost of electricity (LCOE) of CSP was approximately $0.21/kWh, while wholesale electricity prices in the United States are typically well less than $0.10/kWh [30]. Thus, to be competitive with existing power generation, the cost must be brought down significantly, with some sources indicating a target LCOE of approximately $0.06/kWh [31].

Alternatively, incident solar radiation can be converted directly (rather than indirectly, as in CSP) into electricity using photovoltaic cells. While the photovoltaic effect was first discovered in 1839, the first photovoltaic cell wasn't developed until 1954 [32]. A photovoltaic cell (or solar cell) is a solid state device in which light is absorbed by a semiconducting material. Those photons are then used by the material to generate excited charge carriers (electrons and holes) which are then separated and extracted from the cell as useful current. Solar cells convert light directly into electricity.

As shown in Figure 6, an extremely wide array of photovoltaic technologies exists, with a correspondingly large range of solar-to-electric power conversion efficiencies. The maximum theoretical efficiency a single p-n junction solar cell (using a 1.1eV semiconductor) can attain is limited to about 30%, as a result of the Shockley-Queisser limit, which accounts for various

unavoidable loss mechanisms, including non-absorption of below-bandgap light and the relaxation of above-bandgap charge carriers down to the band edges. Traditional silicon solar cells (with a bandgap of 1.1eV), have nearly reached their theoretical maximum efficiencies, currently holding record cell efficiencies as high as 27%. While silicon solar cells typically use hundreds of microns (in thickness) of semiconductor in the part of the cell that absorbs light and converts it to useful current, other so-called "thin film" technologies have been developed that use significantly less (orders of magnitude) material, typically a few microns or even a few hundred nanometers. This is significant given that materials cost constitutes a large fraction of total cell cost. Despite using far less material, thin film technologies have still achieved efficiencies nearly comparable to that of crystalline silicon solar cells. For instance, thin film cells based on copper indium gallium diselenide (CIGS) have reached efficiencies of nearly 22%, as have cells made from CdTe as the light absorbing material. Even newer, "emerging" technologies (that are also, incidentally, thin film technologies) exhibit significantly lower efficiencies than their more mature counterparts. For instance, solar cells based on organic materials such as semiconducting polymers and small molecules have achieved record efficiencies of just over 11%, while those comprised of quantum dots (nanocrystals which exhibit quantum confinement), and the focus of this work, have reached efficiencies of nearly 10%.
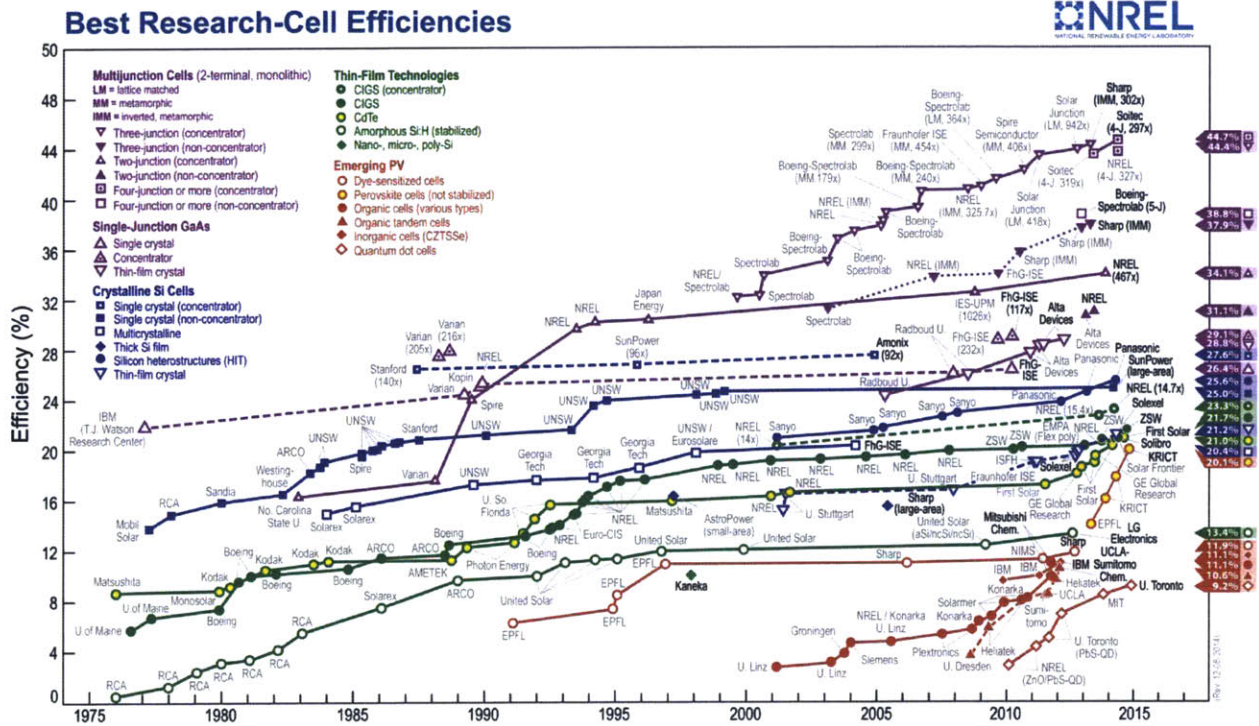
Figure 6. Certified record power conversion efficiencies for various types of photovoltaic cells over time [33].

Figure 7 presents a technology roadmap developed by Martin Green. In it, he plots current, first generation solar cell technology (such as silicon solar cells), second generation solar cells (such as organic, quantum dot, and other thin film photovoltaics), and third generation solar cells, which encompass devices that could harness new physical processes and phenomena to exceed the Shockley-Queisser limit [34]. Additionally, he indicates anticipated device efficiencies (in %) and manufacturing cost regimes (in $ / m^2) for each generation of technology, as well as lines of constant, installed module price (in $ / W). A generally accepted threshold for widespread commercialization and adoption is an installed price of $1/W. Technologies to the left of that line in Figure 7 are expected to be economically feasible enough to see widespread commercial deployment.
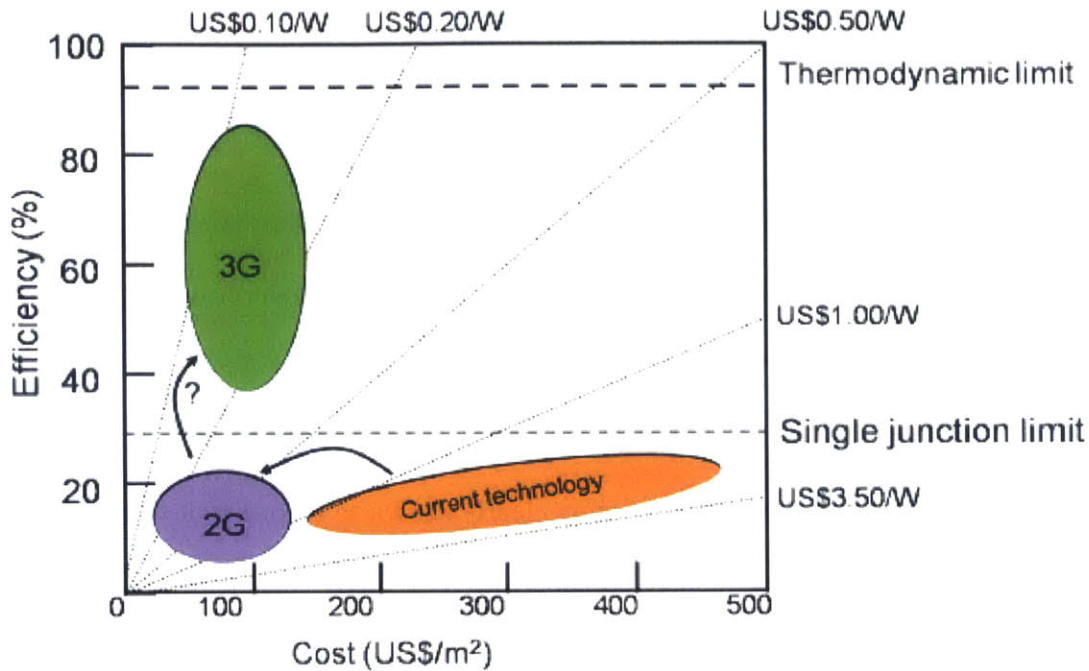
Figure 7. Photovoltaic technology roadmap plotting various generations of solar cell technology by their efficiency and manufacturing cost. Also indicated are various efficiency limits and important module cost thresholds [34].

As noted earlier, thin film and emerging technologies hold promise, not because they are capable of exceedingly high power conversion efficiencies, but because of significantly lower manufacturing costs that result in total installed prices well under $1/W. This results from two generally shared characteristics of second generation photovoltaic technologies. First, as indicated earlier, they require significantly less semiconducting material than traditional silicon solar cells. As a result, materials costs during manufacture are very low. Second, many, if not all, of these thin film and emerging technologies can or will be manufactured in ways that don't require capital equipment and processes that are very expensive, also typical for silicon solar cell manufacture. Furthermore, these inexpensive processing techniques can be applied and scaled to very large substrates, such that solar cells of very large area can be quickly and inexpensively

fabricated. Taken together, second generation technologies promise to have exceptionally low manufacturing costs, enabling them to be commercialized at competitive installation prices.

As schematically conveyed in Figure 7, the cost of current photovoltaic technology is not quite commercially competitive. Further evidence of this is found in the LCOE for utility scale photovoltaics (see Figure 8). As with CSP, the LCOE of solar cell-derived electricity at the utility scale is above $0.20/kWh (as of 2010), which must be brought down significantly to a level below $0.10/kWh in order to serve as a market-parity source of electricity. Additionally, while Figure 8 illustrates how the cost of photovoltaic-derived electricity has, indeed, fallen in the last few years, much of the cost reduction is clearly shown to be due to lower module costs, the part of the photovoltaic system that contains the solar cells. This further highlights the critical importance of the manufacturing cost in determining whether or not a particular solar cell technology can serve as a cost competitive large scale source of our electricity.
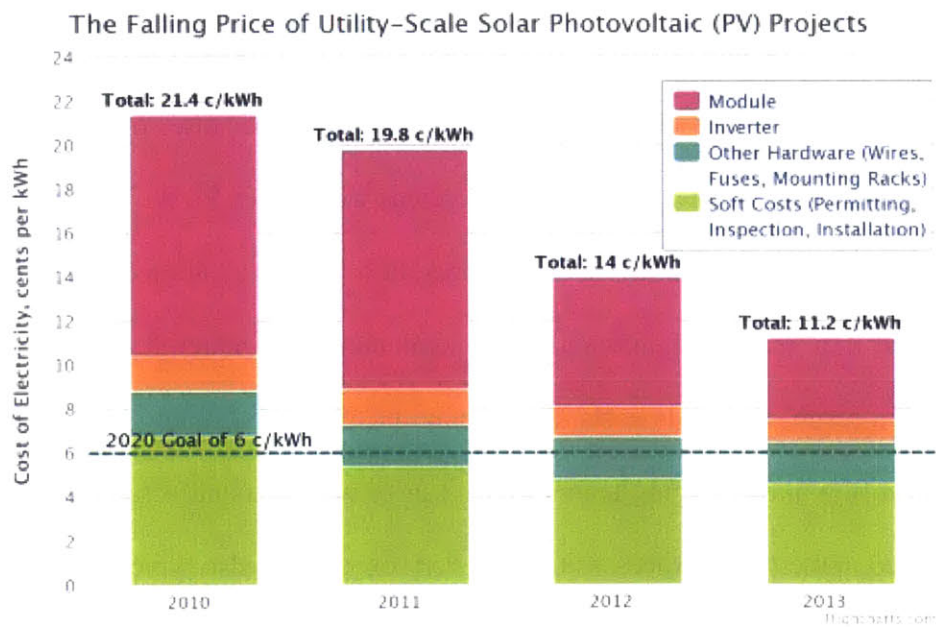
Figure 8. Levelized cost of electricity for utility scale photovoltaic power plants [35].

Fundamentals of Quantum Dot Photovoltaics

Photovoltaic devices based on colloidal quantum dots have exhibited rapid progress in both understanding and device performance in the short time they have been studied. They offer many advantages that have made their study of particular interest to solar cell researchers. They are easily solution synthesized and solution processed (both at reasonably low temperatures below 200°C). This latter attribute allows them to be incorporated into functional and high performance devices with comparative ease. Additionally, while efficient harvesting of the wide range of photon energies available from the solar spectrum has been the focus of solar cell development for years, regardless of specific photovoltaic technology, quantum dots allow for easing tuning of light absorption based merely on their size. Some QDs even allow for additional, potentially beneficial optoelectronic effects such as multiple exciton generation [36] and photon up- and down-conversion [37].

Advances in the understanding and performance of QD-based solar cells have generally fallen into one of two categories. The first has been a significantly improved understanding of the dot itself, specifically, its optoelectronic properties and how best to control and harness them. The second, and the focus of this work, has generally focused on improving the methods for charge separation and extraction, which includes (but is not limited to) novel device architectures.

An ongoing challenge in the development of new and ever higher performing solar cells is optimization of light absorption of the solar spectrum. Presented in Figure 9, the light hitting the earth spans a wide range of wavelengths from below 300nm to as high as 4000nm in the mid-infrared. For the purposes of standardized testing and reporting of performance data of solar cells, a reference spectrum called AM1.5G is used. Air mass 1.5 refers to the pathlength of the atmosphere through which the light travels before being incident upon the solar cell (1.5

"atmospheres" of thickness). For AM1.5, this corresponds to an incident solar zenith angle of 48.2°. The "G" refers to the "global" AM1.5 solar spectrum, which includes both direct sunlight as well as sunlight that has been diffused in the atmosphere.

As presented in Figure 9, semiconductors with different bandgaps absorb different fractions of the solar spectrum. Those with small bandgaps can absorb a lot of light and generate a lot of useful current in a solar cell, but at the expense of a low voltage. On the other hand, semiconductors with a large bandgap can produce devices with correspondingly large voltages, but because they absorb comparatively less light, they generate less current as well. As a result, "optimal" solar cells rely on semiconductors with an intermediate bandgap (1.1-1.4eV) such that a balance is struck between these two competing effects and the maximum power is generated.
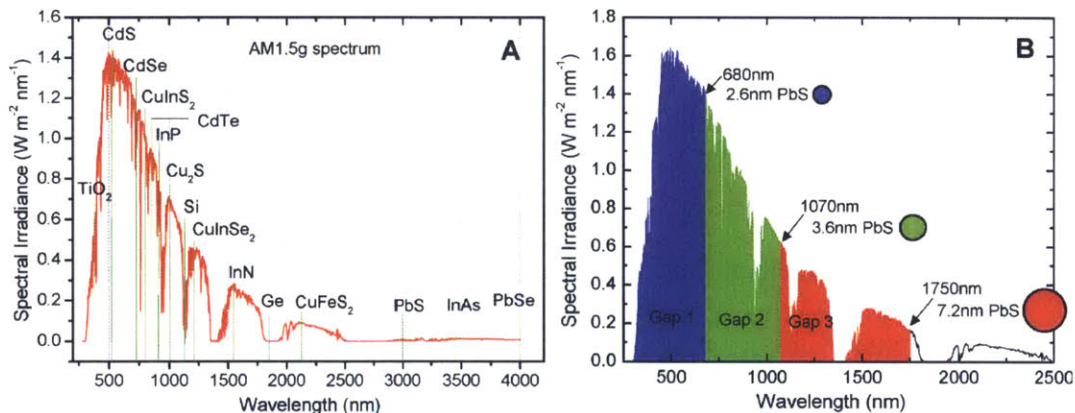
Figure 9. (a) AM1.5G solar spectrum with the bandgaps for various bulk semiconductors indicated. (b) Solar spectrum with various quantum dot size-dependent energy gaps indicated [38].

As previously alluded to, quantum dots possess an interesting electronic property called quantum confinement that makes them attractive for incorporation into solar cells. As the size of the semiconductor is decreased below a certain threshold at which the spatial confinement dimensions become comparable to the wavelength of the charge carrier wavefunction, the Bohr

exciton radius (18nm for PbS [38]), the allowed carrier energy states are no longer continuous, as in a bulk material. Instead, they become discrete and dependent on the physical dimensions of the confining material. As these physical dimensions shrink, the size of the particle for instance, the energy gap increases significantly [39, 40]. This effect is illustrated in Figure 9(b), in which PbS quantum dots of different sizes are shown to have different energy gaps, and, as a result, they absorb different fractions of the solar spectrum. While bulk PbS has a bandgap of only 0.37eV [41], because of quantum confinement, PbS quantum dots can be synthesized with energy gaps in the preferred "optimal" range for solar cells (1.1-1.4eV).

In practice, however, the energy gap of quantum dots is rarely completely empty. Surface defects and surface oxidation products on the dots introduce midgap energy levels that reside within the otherwise forbidden energy gap. These can act as very strong recombination centers where previously excited and separated electrons and holes are lost to carrier recombination [42]. As a result, the number of photogenerated charge carriers that are extracted decreases, ultimately decreasing the solar cell's photocurrent. How deep in the semiconductor's energy gap those midgap trap states appear depends on the type of defect that caused it. Exceptionally deep midgap states (a large energy difference with its associated allowed energy band) are the most deleterious to device performance. Charge carriers that fall into them require a great deal of energy to once again be excited and become free charge carriers (a low probability event). Carriers that are trapped in states that are shallower in the energy gap (less of an energy difference with its associated allowed energy band), however, have a higher probability of gaining the necessary energy to once again become an excited free charge carrier. To mitigate these midgap energy trap states, QDs are "passivated," often through the use of surface ligands. Because PbS quantum dots (the material used in this work) typically have a non-stoichiometric

shell that's lead-enriched [43, 44], thiol-based ligands are typically used, given their high affinity for Pb cations. Despite this, challenges remain in the use of thiol-based ligands. The metal-sulfur moieties can be susceptible to oxidation, severely limiting the lifetime of QD-based solar cells, particularly if they are unencapsulated and left exposed to ambient air [38]. Additionally, because thiol-based ligands preferentially bind to surface cations, the anions are still exposed to oxygen attack and may, themselves, introduce undesired midgap trap states due to incomplete passivation [45, 46].

Improvements to Quantum Dots

Improvements to the quantum dots themselves, most often to the way in which they're passivated by various types of ligands, has significantly enhanced the performance of these materials in functional solar cells.

For instance, Konstantatos, et al., in developing photodetectors, showed that it is possible to engineer a desired response time into their devices by exposing their PbS quantum dot films with various chemical treatments. Different treatments resulted in different surface oxides with various time constants for the release of charge carriers from the deep or shallow traps they produce. For example, butylamine treatment produced $PbSO_4$ and Pb-carboxylate oxides with trap time constants as high as 300ms. Formic acid produced similarly long lived midgap traps. Treatment with ethanethiol, however, produced only a single surface oxidation product, lead sulfite, which had a very desirable trap time constant of 27ms, appropriate for use in their photodetectors [47].

Barkhouse, et al., found similar benefits to treating their PbS QD solar cells with ethanethiol. Following exposure, the charge carrier mobility increases, as does the open circuit voltage and the external quantum efficiency, confirming previous reports that treatment of PbS QDs with thiol ligands can improve the overall power conversion efficiency of PbS based solar cells by an order of magnitude. Further, they confirm the idea that thiol treatment removes a great number of deep electron trap states, while leaving behind the far less deleterious shallow midgap traps [48].

In another report, Luther, et al., prepared PbSe quantum dot films that were then treated with 1,2-ethanedithiol (EDT). It was discovered that EDT does, in fact, displace oleic acid on the PbSe surface. As a result, a large volume loss was observed in the films, presumably due to replacing a relatively long chain ligand with a very short one, thereby decreasing the insulating space between adjacent quantum dots. This benefits their use in electronic devices, as adjacent particles become more electronically coupled. Furthermore, upon EDT treatment, Luther found that the previous crystalline order of the untreated films was removed, resulting in a disordered random close packing [49].

While investigating charge carrier mobilities in solids of PbSe quantum dots, Liu, et al., found that mobilities decreased expotentially as the length of the attached alkanedithiol ligands increased. In particular, they found that the carrier mobility can change by several orders of magnitude as the length of the ligand changes by only 5-6 angstroms, with the highest mobilities being observed for films treated with EDT. This result is consistent with the model of hopping carrier transport from dot to dot through an insulating ligand matrix that is often seen in quantum dot solids [50].

In a slightly different approach, Bae, et al., treated PbSe quantum dots with solution phase molecular chlorine. They found that the Cl_2 preferentially etches out surface anions on the quantum dots and reactions with Pb to form a very thin shell of $PbCl_x$. This shell effectively passivates the dots by preventing the generating of deleterious surface oxidation products that would otherwise introduce deep midgap trap states. This was confirmed by an increase in photoluminescence efficiency, given that fewer charge carriers were lost to non-radiative recombination with surface defects [51].

More recently, the use of atomic ligands to passivate quantum dot surfaces has allowed for the fabrication of consistently higher efficiency QD-based solar cells than is typically possible with the more traditional organic ligand passivated quantum dots. Tang, et al., developed a method by which PbS dots are passivated completely by atomic ligands. During PbS quantum dot synthesis, the surface anions are passivated with Cd from a complex of cadmium-tetradecylphosphonic acid. Later, during film formation or device fabrication, a solid state ligand treatment is conducted in which surface cations are passviated with bromide from a complex of cetyltrimethylammonium bromide. The stark differences in ligand sizes are illustrated in Figure 10 [52].
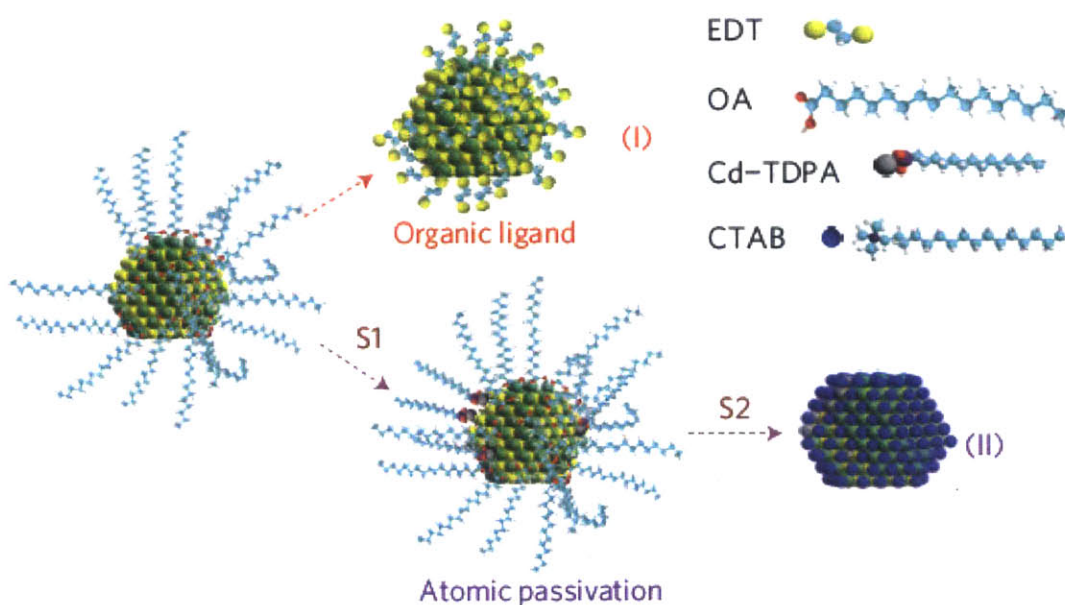
Figure 10. Schematic illustration comparing the molecules (and their respective sizes) involved in the traditional organic ligand passivation as well as the newly developed atomic ligand passivation scheme [52].

Solar cells fabricated from these atomic ligand passivated dots were able to reach as high as 6% overall power conversion efficiency. A major reason for this is the significant improvement in carrier mobility that atomic ligand passivated dots exhibit over their organic ligand passivated counterparts. For instance, a nearly order of magnitude improvement in carrier mobility was observed for electrons in atomic ligand passivated PbS films over the best organic ligand, 3-mercaptopropionic acid (MPA), which itself, exhibited an equally large enhancement in carrier mobility over EDT. It was clear from their study that Br⁻ capped PbS quantum dots had a distribution of midgap trap states that was much shallower than that typically seen in organic ligand passivated dots, resulting in significantly improved carrier mobilities and, ultimately, device performance [52].

Soon thereafter, the same research group reported a "hybrid passivation" approach in which PbS quantum dots were passivated with both atomic and organic ligands. There were then able to fabricated solar cells with efficiencies as high as 7%. In this hybrid approach, Cl⁻ anions are introduced onto the surface of the as-synthesized oleate-capped quantum dots at the very end of the synthesis procedure, while the dots are still in solution phase. The halide ligands fill in the empty trenches on the surface of the dot that weren't able to be passivated by oleate during nanocrystal growth. Then, during film deposition and device fabrication, a solid state ligand exchange process was carried out in which oleate was replaced with MPA. The final devices thus had dots passivated with both organic MPA molecules and with chloride anions [53].

Improvements in Charge Extraction

While many of the leaps in quantum dot photovoltaic device performance stemmed from an improved understanding of and control over the ligands and surface passivation of the dots themselves, thereby engineering the midgap trap distribution in the dots, other advances have come from new device architectures and the engineering of the interfaces between the various materials in the photovoltaic device stack. That is, they have come from improved means of separating and ultimately extracting charge carriers from the photoactive layer.

For instance, in the earliest quantum dot solar cells, Schottky type structures were used in which the semiconductor was bound by a transparent electrode and shallow work function metal. An internal electric field is created at the metal-semiconductor junction, giving the device its rectifying characteristics [54-56]. This is illustrated schematically in Figure 11.
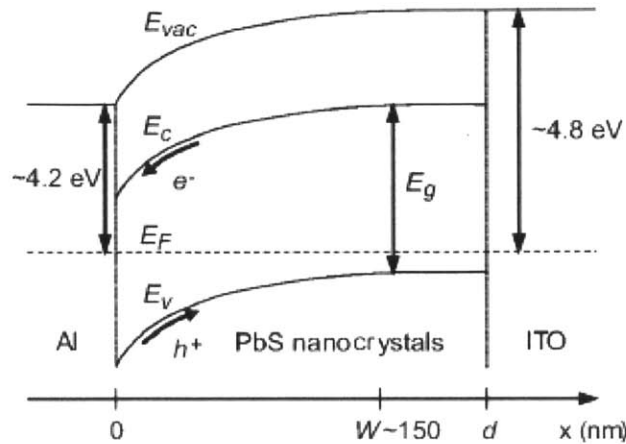
Figure 11. Schematic energy band diagram of a Schottky junction solar cell comprised of PbS quantum dots. E_c = conduction band, E_v = valence band, E_{vac} = vacuum energy level, E_F = Fermi level, E_g = bandgap [55].

Performance of these devices remained stifled by the inherent shortcomings of this device structure, however. For instance, the internal electric field is localized to the metal-semiconductor junction deep at the back of the cell, where comparatively few photons are absorbed. Rather, many more photogenerated charge carriers are created shallow in the cell, near the transparent electrode. The absorption coefficient generally decreases with increasing light wavelength and the incident solar spectrum over the absorbable wavelength range contains many more high energy photons [38] that are thus absorbed in the shallowest regions of the cell, far away from the charge-separating Schottky junction. As a result, many of the carriers generated can't be efficiently separated and extracted.

To address this, a depleted heterojunction structure was introduced recently in which p-type quantum dots such as PbS are deposited on top of an n-type semiconductor such as TiO_2 or ZnO (wide bandgap n-type semiconductors are chosen to allow for optical transparency over the wavelength range of interest) in a bilayer or planar configuration. Thus, the heterojunction between the p-type and n-type materials produces a depletion region whose associated electric

31

field serves as a charge separating driving force in the same way the electric field of the Schottky junction did. However, unlike the Schottky junction, the depleted heterojunction is located much closer to the front of the cell (the side with the transparent electrode) where most of the photogenerated charge carriers are located [57-59]. A schematic illustration of the energy band diagram of a depleted heterojunction is presented in Figure 12.
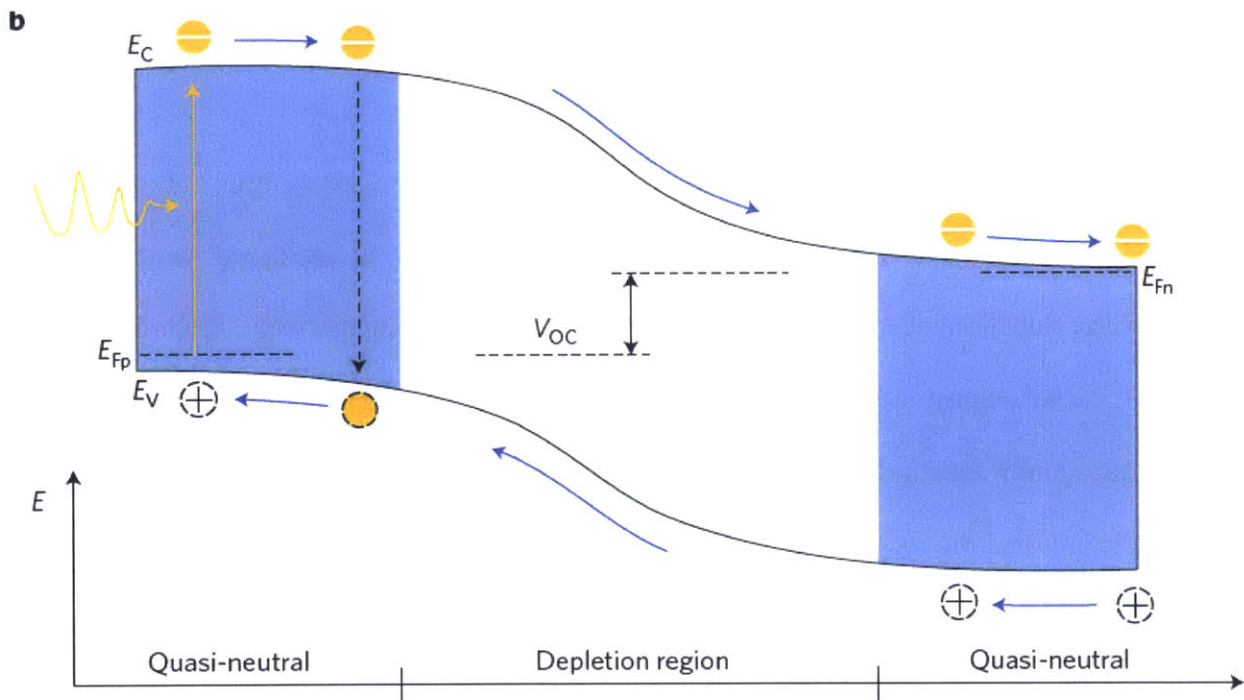
Figure 12. Schematic energy band diagram of a depleted heterojunction illustrating the charge-separating depletion region centered at the heterojunction interface [60].

While a significant improvement over the Schottky junction, this device structure is not without its own charge extracting limitations. Charge carriers generated outside the depletion region

must still be able to diffuse to it in order to be separated and extracted. However, the diffusion length in these quantum dot solids is typically 10-100nm [61]. Additionally, the width of the depletion region in PbS has been estimated to be around 100-150nm [42, 55]. Therefore, the thickness of a quantum dot film that can be used in a practical solar cell is limited to only about 250nm [62], an approximation of the upper limit of the carrier collection length. However, given the absorption coefficient of these quantum dot solids, complete light absorption requires as much as $1\mu m$ worth of light absorbing material [38, 63].

To address these challenges, a bulk heterojunction architecture may be borrowed from organic photovoltaics [64]. Unlike a depleted heterojunction, which adopts a bilayer or planar interface and, hence, is typically also referred to as a bilayer or planar heterojunction, the two semiconductors in a bulk heterojunction interpenetrate each other in some manner. This potentially allows for the use of much thicker optically absorbing layers, since the heterojunction interface is distributed across a much larger depth of the cell, rather than just a single depth as in a bilayer heterojunction. A computer generated illustration of a disordered organic bulk heterojunction is presented in Figure 13. As is easily seen, the intermixing of the p-type and n-type phases extends the heterojunction interface throughout the entire depth of the solar cell. This, in turn, allows the depletion region and its associated charge-separating electric field to occupy a significantly greater volume of the device. As a consequence, charge carriers generated anywhere in the cell have a high likelihood of reaching the depletion region at an interface between the two phases where they can then be separated and extracted.
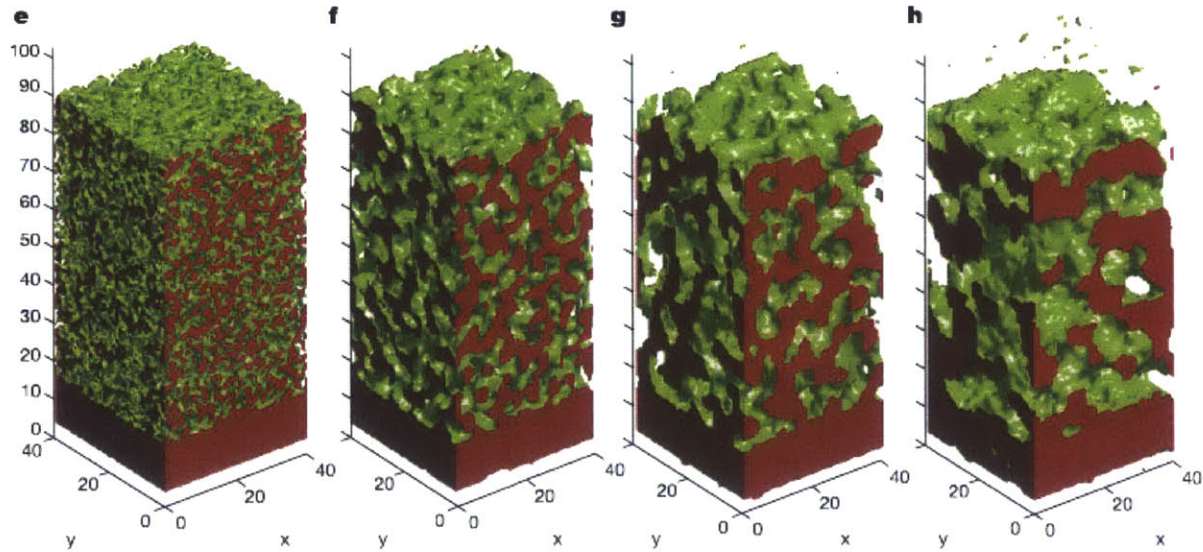
Figure 13. Computer simulated images of bulk heterojunction blends from an organic bulk heterojunction device [65].

Examples of attempts to create an ordered or disordered bulk heterojunction structure for use in quantum dot solar cells are presented in Figure 14. Unlike organic bulk heterojunctions in which the two semiconductors are typically mixed together beforehand and then spincast into blended solid films, many of the attempts to create quantum dot bulk heterojunction solar cells have focused on infiltrating the dots into some kind of porous n-type structure.
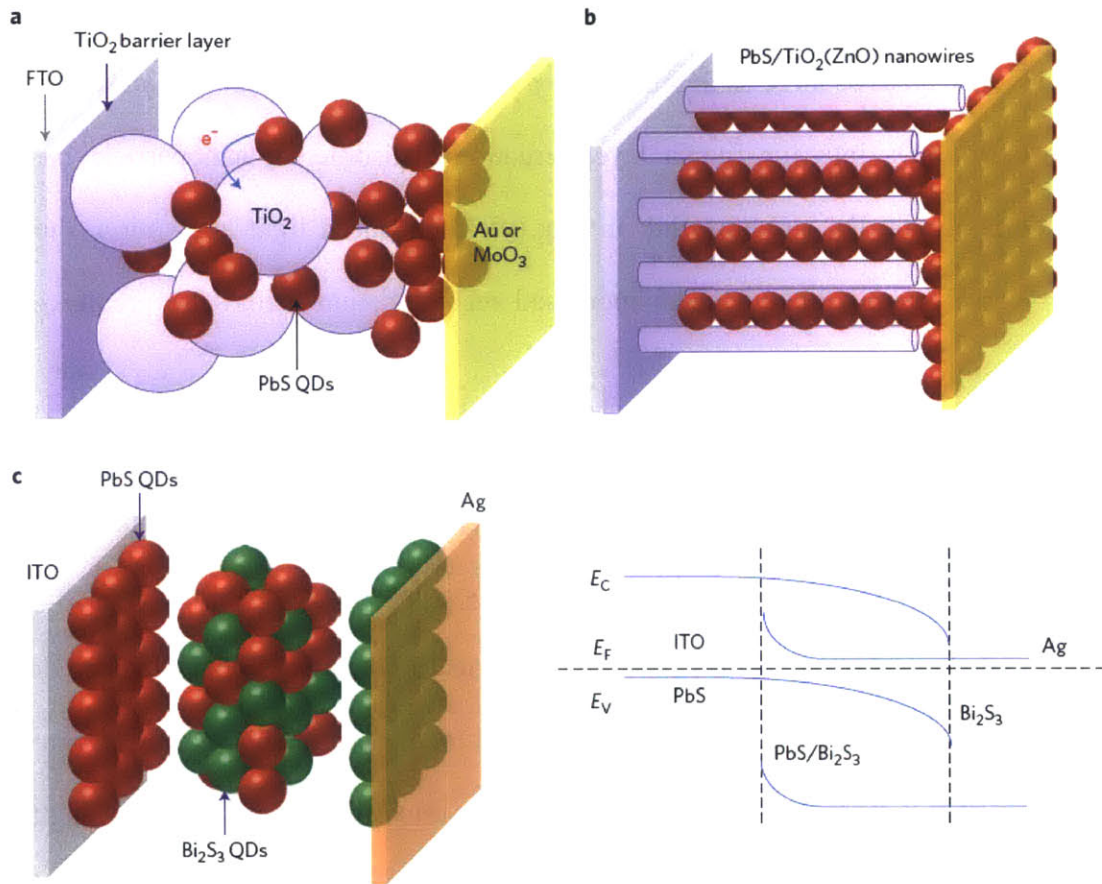
Figure 14. Examples of bulk heterojunction structures used in PbS quantum dot based solar cells. (a) disordered bulk heterojunction in which the QDs are infiltrated into a porous nanoparticle film, (b) ordered bulk heterojunction in which QDs are infiltrated into vertically aligned nanowires, (c) disordered bulk heterojunction in which two sulfide QDs are blended together and cast into a film [60].

For instance, Leschkies, et al., infiltrated PbSe quantum dots into ordered ZnO nanowires. The team found that with respect to the planar analogue of the same materials, the nanowire bulk heterojunction produced significantly higher photocurrent due to improved charge separation and extraction [66].

As illustrated in Figure 14(a), Barkhouse, et al., instead infiltrated PbS quantum dots into a porous TiO$_2$ nanoparticle layer, rather than nanowires. They first deposited a pure titania base

layer of small nanocrystals 10-30nm in size. On top of this, they deposited a diffuse layer of nanoparticles with sizes as large as 250nm. The porous nature of this nanoparticle layer allowed them to backfill QDs into the titania layer, creating a disordered, nanoparticle based bulk heterojunction. While the structure did, in fact, yield enhanced light absorption, the devices performed worse overall, likely due to increased recombination across the greatly increased interfacial area throughout the device [67].

While this attempt at creating a high efficiency bulk heterojunction was only partially successful, it did highlight the ever present need for more precise control over the film structure. As a result, the same research group later used electron beam lithography to template the growth of titania nanopillars with control over their pitch. They found that in order for high efficiency devices to be obtained, the distance between adjacent pillars had to, as described before, be approximately twice the sum of the depletion width (in PbS) and the minority carrier diffusion length. With this, they were able to obtain devices with efficiencies as high as 5.6% [68].

Through the use of a similar structure, solar cells with efficiencies as high as 7.3% were obtained. Lan, et al., created a vertical titania nanowire network from a template of ZnO nanowires. Unlike the well defined structure of the pillars, adjacent nanowires sometimes bundled together. Ultimate titania nanowire lengths reached approximately 300nm, as did the separation between various "bundles" of these nanowires. Because the bulk heterojuction, as intended, spatially extended the range of the depletion region to a greater volume of the device, they found they could use even thicker layers of PbS than can be used with a planar heterojunction without sacrificing performance [69].

Nanowire bulk heterojunction solar cells based on ZnO have also exhibited such performance gains. Jean, et al., used ZnO nanowires grown off a ZnO seed layer in a PbS-based nanowire

bulk heterojunction device. As others have as well, they observed increases in short circuit current density as well as a significant enhancement in overall power conversion efficiency when compared to bilayer ZnO-PbS solar cells. Their champion device reached an efficiency of 4.9% [62].

Wang, et al., similarly fabricated ZnO nanowire based bulk heterojunction solar cells; however, in their devices, the ZnO nanowires were grown to lengths over 1µm. Their best performing device, with an efficiency of just over 6%, had the smallest nanowire diameter and the highest nanowire density of the various samples they examined [70].

Finally, as depicted in Figure 15, an effort has been made to develop a quantum dot based solar cell that more closely mimics the structure and processing of organic bulk heterojunction solar cells. Rath, et al., mixed liquid dispersions of PbS quantum dots and Bi_2S_3 nanocrystals and then spincast this mixture directly into blended solid bulk heterojunction films. This mirrors the way in which organic bulk heterojunctions are typically fabricated by mixing, for example, a semiconducting polymer directly with a well matched fullerene in solution and then spincasting this mixture directly into a blended solid film. A significant, 3-fold improvement in the power conversion efficiency was observed for champion bulk heterojunction devices relative to their planar counterparts. Because of the nanostructured blending of the two different nanocrystals, charge carrier lifetimes increased. In this particular example, too, both phases were photoactive and absorbed light, a distinction not shared by other PbS quantum dot solar cells based on wide bandgap semiconductors like TiO_2 or ZnO [71].
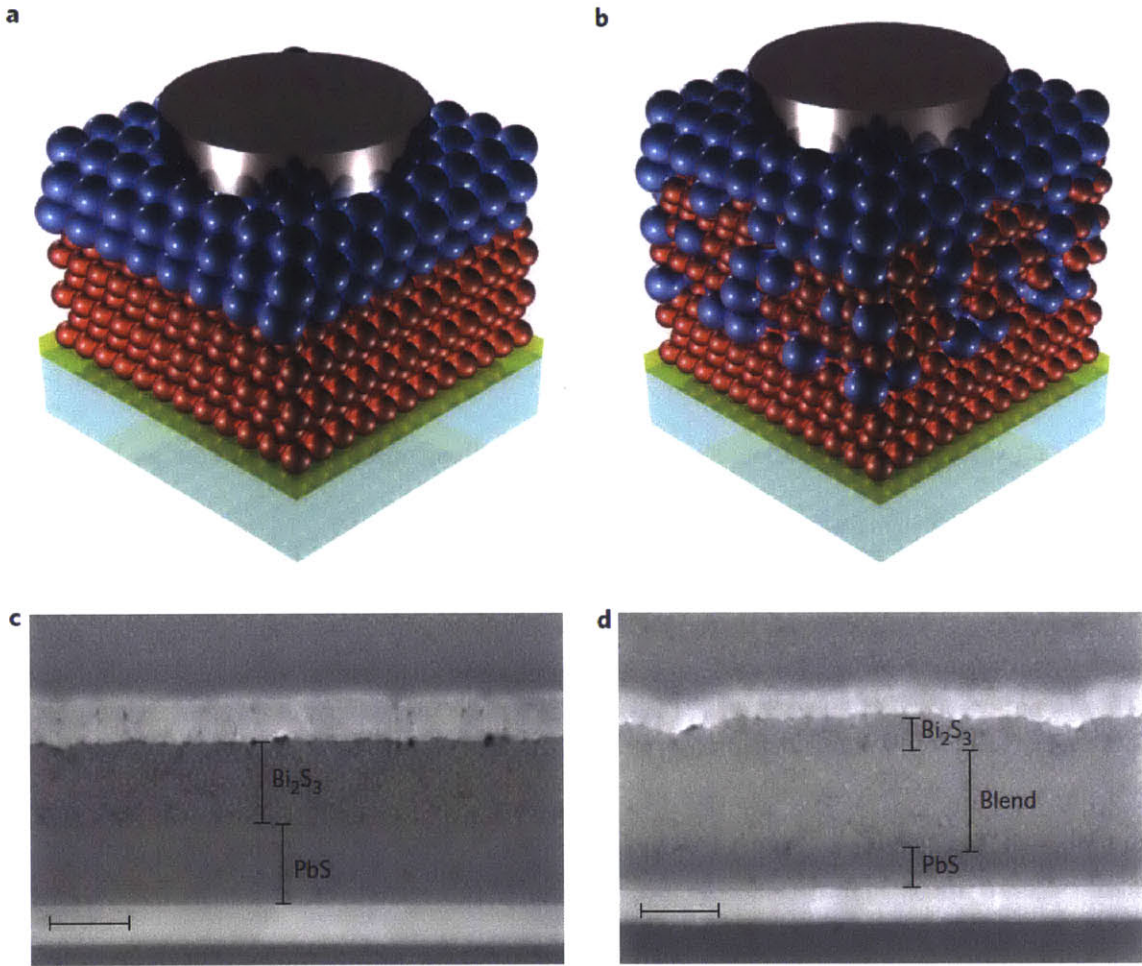
Figure 15. (a, c) Schematic illustration of a bilayer heterojunction of PbS and Bi_2S_3 nanocrystals and its accompanying cross sectional scanning electron micrograph, (b, d) schematic illustration of a bulk heterojunction of PbS and Bi_2S_3 nanocrystals and its accompanying cross sectional scanning electron micrograph [71].

Beyond the engineering of device architectures, much of the recent work in quantum dot solar cells has also focused on engineering the interfaces between the constituent materials themselves in an effort to produce even better charge separation.

For example, Liu, et al., were able to introduce dopants such as Zr and Sb into TiO_2 in order to tune the conduction band edge. By tuning this parameter, they were able to engineer the energy offset between TiO_2 and PbS. They were able to show that by increasing the electron affinity of titania, they could increase photocurrent and overall device efficiency. However, there was an optimal amount that the conduction band edge could be deepened, as deepening it too far would result in a decrease in the device's photovoltage. Using this technique, planar (not bulk heterojunction) devices with efficiencies as high as 5.6% were obtained [72].

Maraghechi, et al., were able to set a record efficiency (at the time) of 8.5% by making two changes to the typical PbS-TiO_2 bilayer heterojunction. First, they used a fluorine-doped tin oxide (FTO) electrode whose work function was shallower than that of FTO typically used in titania-based solar cells. Second, they used an extremely thin titania layer (10nm, rather than the more typical 100-300nm) deposited by atomic layer deposition. As a result, additional electrons are injected into the thin titania layer. As a result of this "charge transfer doping" of the TiO_2, the depletion width in the PbS layer increases (see Figure 16). The effect of this is clear. Rather than using a bulk heterojunction device architecture to expand the spatial extent of the charge separating depletion region, they engineered the doping of the electrode, which has the same effect, just as disparate levels of doping in a p-n junction results in different depletion widths on either side of the junction [73].
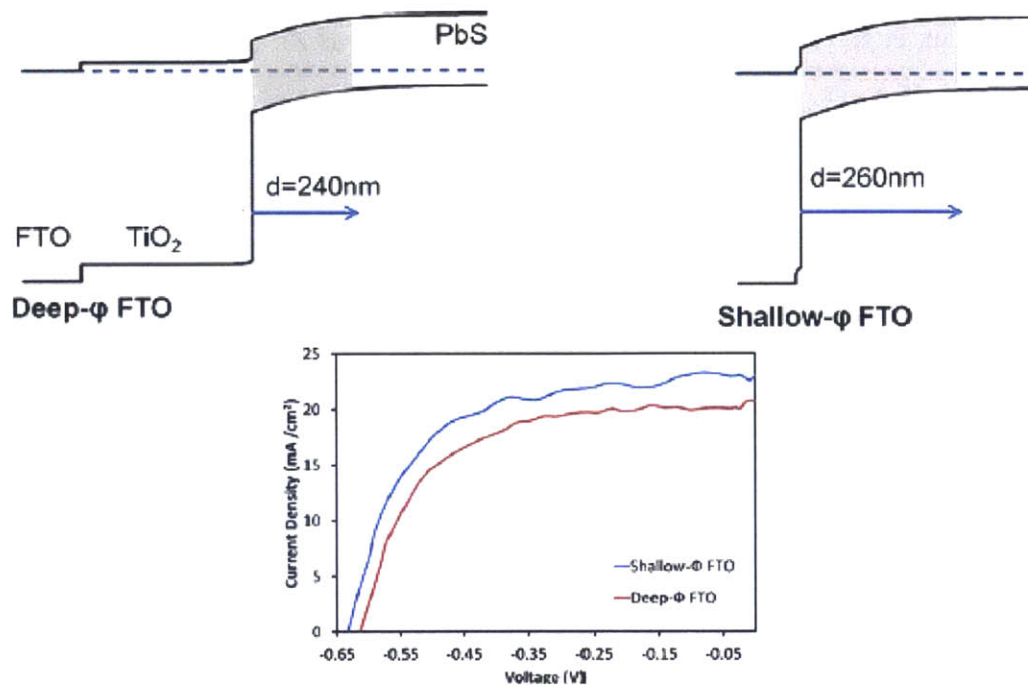
Figure 16. Schematic illustration of how the spatial extent of the depletion region in PbS (in grey and indicated by *d*) can be tuned by altering the work function of the underlying electrode, resulting in a significant leap forward to a new record device efficiency [73].

Additional work on the engineering of the electrode interface has resulted in enhanced device performance as well. For instance, a 65% increase in efficiency was observed when a MoO_x layer was inserted between the metal electrode and the PbS quantum dot layer. It was found that a dipole at the MoO_x-PbS interface enhanced energy band bending which results in more efficient hole extraction from PbS. That MoO_x has shallow midgap trap states likely contributed to the increased performance as well [74].

Similarly, another study on the effect of MoO_3 as an interfacial layer between PbS and the metal anode found that the MoO_3 eliminates a reverse-bias Schottky diode previously present at the interface and pins the Fermi level of the top contact. As a result, a high open circuit voltage is

obtained for a range of different anode materials, and similar increases in photocurrent and fill factor result in devices with enhanced efficiency [75].

Measuring Photovoltaic Device Performance

The two ways photovoltaic devices in this work will be tested are through J-V (current density-voltage) measurements and external quantum efficiency (EQE) measurements.

J-V measurements quantify the behavior of the cell under actual simulated solar illumination. Incident sunlight is simulated with a solar simulator that can output light that corresponds to the previously described AM1.5G solar reference spectrum at a light intensity of $100mW/cm^2$ and, ideally, a cell temperature of 25°C. During testing, the cell is illuminated and a bias voltage is applied to the device and swept over a range of values (e.g., -1 to 1V). The resulting current produced by the cell is then measured, producing a J-V curve of the general shape depicted in Figure 17, where current density is measured in mA/cm^2. Figure 17 also indicates the position of several key parameters often used to described the performance of a solar cell beyond it's overall power conversion efficiency. When no bias is applied, the maximum current generated by the illuminated cell is recorded as the short circuit current density, J_{sc} and is a measure of the ability of the cell to absorb light and extract charge carriers from the device. When the output current is zero, the device is said to be at open circuit. The voltage at this point is often a measure of the charge separating driving force present in the device. The maximum power point labeled in Figure 17 is the point along the J-V curve at which the power (the product of current and voltage) is highest. The ratio of this value to the product of J_{sc} and V_{oc} is the fill factor, which is

a measure of the "ideality" of the device. Devices with higher fill factors are closer to performing as an ideal solar cell would. Related to the fill factor are the series and shunt resistances (measured in Ωcm^2). The series resistance, estimated from the inverse of the slope of the J-V curve at the V_{oc}, is roughly a measure of the resistance through the cell, i.e., the resistance that charge carriers encounter as they travel through the cell. The shunt resistance, on the other hand, estimated from the inverse of the slope of the J-V curve at the J_{sc}, can serve as a measure of loss mechanisms in the solar cell. Ideally, a solar cell should have very low series resistance so charge carriers can easily traverse the cell and get extracted, as well as a very high shunt resistance to prevent charge carriers from being lost to various mechanisms such as short circuiting within the device or charge carrier recombination before they can be successfully extracted by the cell.
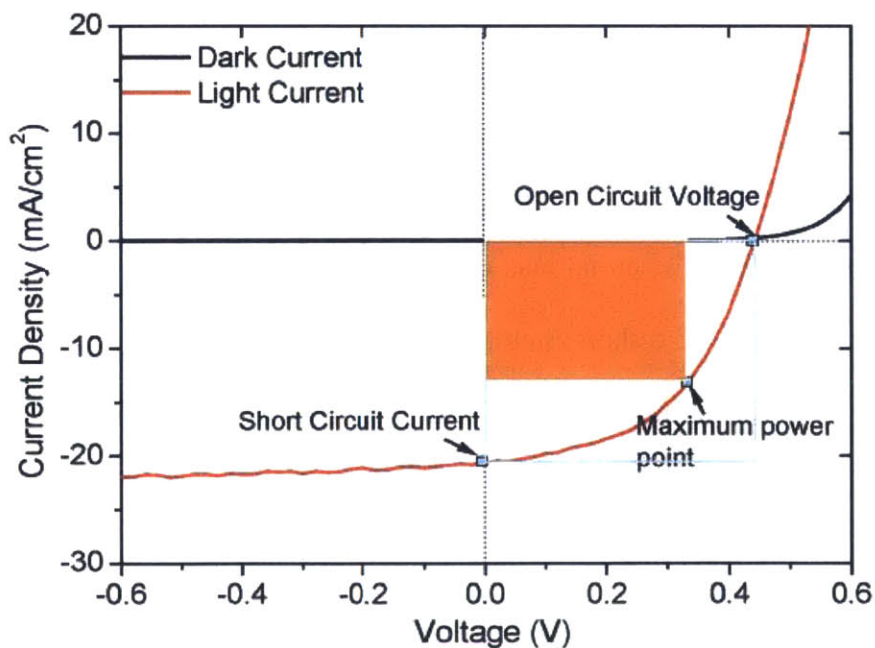
Figure 17. Schematic illustration of a model J-V curve from an illuminated solar cell [38].

The EQE is a measure of the number of electrons flowing through the external circuit per photon incident on the solar cell. It is measured under monochromatic illumination, which is then swept across the wavelength range of interest to compile an EQE spectrum. The EQE is closely related to the light absorption and photocurrent of the device, providing more detailed information regarding how well the device absorbs light and produces useful current at specific individual wavelengths of light.

A Look Ahead

It's clear from the preceding review that several routes exist to enhance the overall performance of quantum dot based solar cells, each with its own advantages and remaining obstacles. The work described here seeks to address the challenge of how to enhance charge separation and extraction in PbS quantum dot based solar cells. The previously described advances have done much to improve upon the early Schottky junction devices, which, while easy to fabricate, were fundamentally not physically designed to separate and extract the greatest number of photogenerated charge carriers. By pairing PbS with an n-type electron acceptor to form a depleted heterojunction, the internal electric field created by the depletion region (the charge separating drive force) was much more optimally positioned to separate and extract a greater number of photogenerated charge carriers. Yet, even this advance was limiting. Due to the practical limits on charge carrier collection length, PbS layers of only a few hundred nanometers may be used, an upper limit which is woefully mismatched to the amount of PbS required for complete light absorption (1 μm).

Our proposed solution is to further develop the bulk heterojunction concept. In this architecture, the p-type PbS phase and the n-type phase form an interpenetrating, intermixed, bicontinuous blend. The result is a dramatic increase in the spatial extent of the depletion region and its charge separating drive force across a significantly larger volume of the device. Ideally, this enables charge carriers generated anywhere in the active layer to easily reach the depletion region, separate, and get extracted from the device as useful current.

The idea to use a bulk heterojunction architecture to address previous shortcomings in charge carrier collection is not new. However, the vast majority of previous work has focused on separately engineering the structure of the n-type phase and the formation of the heterojunction itself. That is, n-type structures are developed, such as the growth of wide bandgap semiconductor nanowires or the deposition of porous semiconductor base layers, and then PbS quantum dots are separately backfilled or infiltrated into these structures. An ongoing challenge with this approach has been the quality of the interface between the PbS and the n-type material. Frequently, such approaches involve the infiltration of small PbS nanocrystals into a structurally complex host structure of bulk semiconductor. Incomplete infiltration, leading to void spaces and gaps throughout volume of the device (particularly at the interface), is a nontrivial concern (see Figure 18). Because the charge separating driving force on which the operation of these solar cells relies is localized to the interface, the quality of the contact between the p-type and n-type phases is paramount. Furthermore, it is optimal for PbS to be infiltrated as deep into the device as possible, i.e., as close to the transparent electrode as possible. It is at those depths that the majority of charge carriers are generated. The ability for the quantum dots to infiltrate deep into the device and form the kind of high quality interface we require is made even more challenging due to the complexity of some of the host structures into which they're being

backfilled (such as mesoporous nanoparticle networks and disordered nanowire forests). Pores and gaps in the n-type host structures may easily become clogged and filled with QDs before they're able to infiltrate completely into the device, leaving incompletely filled voids underneath. Additionally, for a photovoltaics processing method to be commercially feasible, the raw and source materials need to be exceptionally inexpensive (such as is the case for silicon), or the processing methods themselves must be extremely low cost, which often means very few and very simple steps. Ideally, if it were possible to form a bulk heterojunction in a single step as is done with organic photovoltaics, rather than two separate steps (deposition or formation of the n-type host, followed by infiltration of PbS dots into the host structure), that would be preferable. While this may seem like a trivial difference within a university laboratory setting, when scaled up to the megawatt or gigawatt levels of annual production required to economically mass produce solar cells, halving the number of processing steps in the fabrication pipeline can save a significant amount of time and money.
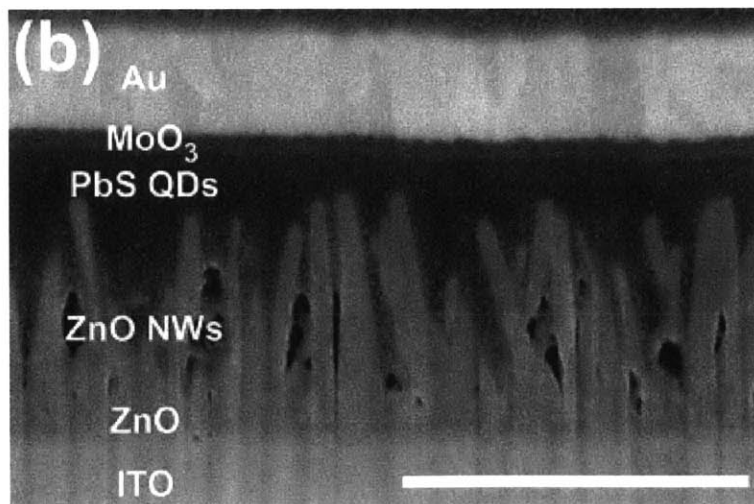
Figure 18. Cross sectional scanning electron micrograph of PbS QDs infiltrated into ZnO nanowires, indicating several large scale voids where incomplete infiltration has occurred [62].

Accordingly, this work addresses these two shortcomings. We have synthesized small titania nanocrystals which may be easily blended with PbS quantum dots in a single solution, in the same way donor and acceptor materials are mixed together in a single solution during the fabrication of organic bulk heterojunction solar cells. Thin films of these mixtures may then be spin cast, naturally forming a nanostructured bulk heterojunction thin film blend of PbS and titania in a single processing step. Films formed from these mixtures are well packed, minimizing the occurrence of large scale voids that can plague devices made by the infiltration of QDs into complex n-type host structures. And because the titania nanocrystals are of the same approximate size (within an order of magnitude) as the PbS quantum dots, the resulting bulk heterojunction blends are extremely well mixed and nanostructured, ensuring that charge carriers generated within the blend are well within a carrier collection length (depletion width + diffusion length ≈ 250nm) of a heterojunction interface.

Chapter 2: PbS and TiO$_2$ Nanocrystals

In this chapter we describe the synthesis and characterization of the materials to be used in the fabrication of our bulk heterojunction solar cells. Monodispersed PbS quantum dots are synthesized over a range of sizes, which, as a result, absorb different fractions of the solar spectrum. The insulating long chain oleate ligands passivating the as-synthesized QDs are easily exchanged for a short chain organic ligand that is much more amenable to high performance device fabrication. The as-synthesized dots are also capped with atomic chloride anions, providing additional electronic passivation against deleterious deep midgap energy states.

Titania nanocrystals with a range of sizes (but within an order of magnitude of the size of our PbS quantum dots) are synthesized as well. As-synthesized, they are the preferred anatase phase without requiring a high temperature treatment. And while they are produced with high natural polydispersity, this, in fact, enables them to form more densely packed blends with our QDs. As with our PbS, the oleate ligands that provide dispersion stability to our nanocrystals can easily be exchanged for the same short chain organic ligand that has been shown to passivate deep midgap states in PbS, resulting in high performance solar cells.

Synthesis and Characterization of PbS Quantum Dots

Materials

1-octadecene (technical grade, 90%) (ODE), oleic acid (technical grade, 90%) (OA), lead (II) oxide (technical grade, 99.999%), cadmium chloride (99.99%), and hexamethyldisilathiane (synthesis grade) (TMS) were purchased from Sigma-Aldrich. 1-tetradecylphosphonic acid

(98%) (TDPA) was purchased from Alfa Aesar. Oleylamine (80-90 %) was purchased from Acros. All materials were used as received.

Methods

PbS quantum dot ("QD" or "dot") synthesis followed standard published methods [53, 76]. While several different approaches are typically used to synthesize PbS QDs for use in optoelectronic applications, the particular synthetic route we chose has been shown to produce exceptionally high performance QD solar cells due to the presence of two (rather than the more typical one) passivating ligands on the surface of the QDs. Perhaps the most frequently used synthetic route originally reported by Hines, et al., involves the capping of the QDs with oleate [76] to electronically passivate surface defect trap states as well as to introduce dispersion stability. Nearly a decade later, however, Ip, et al., modified that procedure to include a second capping ligand that filled the vacant voids on the QD's surface in between the original oleate ligands. This was possible given that the new ligand was a small atomic halide ion (chloride), rather than a long chain hydrocarbon. The new "hybrid passivated" QDs have better electronic defect passivation than the older organic passivated QDs, while still retaining the same organic solvent dispersion stability.

A metal halide precursor was first prepared by dissolving 0.3 g $CdCl_2$ and 0.033 g of TDPA in 5 mL of oleylamine in a three-neck flask and degassed at 100°C by pulling vacuum on the flask while it was under constant stirring and submerged in a hotplate-heated oil bath. The metal halide solution was then kept at 80°C under nitrogen to prevent solidification.

In a separate three-neck flask, 0.45 g of PbO, 1.5mL of oleic acid (the organic capping ligand), and 18 mL of ODE were degassed under vacuum at 125°C under constant stirring. A sulfur

48

precursor was prepared by mixing 0.18g of TMS (weighed out beforehand in an argon atmosphere glovebox) with 10mL of degassed ODE. The sulfur precursor solution was then rapidly injected into the lead solution reaction flask at the desired reaction temperature. Immediately after injection, the reaction mixture was removed from heat and allowed to cool down naturally to room temperature. When the mixture cooled down to 60-70 °C, 1 mL of the metal halide precursor solution was rapidly injected. Once the entire mixture reached room temperature, the QDs were purified and isolated through several centrifugation wash cycles. The QDs were first precipitated with acetone and isolated by centrifugation. The QDs were subsequently re-dispersed in toluene and precipitated again with excess acetone and methanol, followed by centrifugation. Finally, the QDs were washed several more times with methanol and stored as a dry powder in a vacuum dessicator.

For the purposes of this work, we only used reaction temperature to control QD size. The ultimate QD size may also be tuned by varying the ratio of oleic acid to ODE. Oleic acid not only serves as the passivating and stabilizing ligand for the QDs, but also, it provides nucleation sites during the reaction for the growth of the QDs. When there are a relatively greater number of OA molecules in solution (with all other factors remaining constant), there are more nuclei on which particles may grow. Thus, when a given amount of material is split up among more nuclei, each individual particle cannot grow as large. A greater OA/ODE ratio generally leads to smaller QDs, with other factors remaining unchanged.

Transmission electron microscopy (TEM) was performed on a JEOL 2010 TEM. Powder X-ray diffraction (XRD) spectra were obtained on a PANalytical X'Pert Pro X-ray powder diffractometer. X-ray photoelectron spectroscopy (XPS) analysis was performed on a PHI Versa-Probe II spectrometer with a scanning monochromated Al source (1,486.6eV; 50 W; spot

size, 200 μm). An argon source was used for sputtering and the zalar rotation was set at 1rpm. Fourier transform infrared spectroscopy (FTIR) was performed on a Jasco FTIR spectrometer. UV-vis absorption measurements were performed on a Beckman Coulter DU800 spectrophotometer.

Quantum Dot Structure

We first studied the synthesized QDs under TEM to gauge size and shape (Figure 19). The QDs appear spherical and relatively monodisperse, with an approximate size of 3nm, ideal for use in high performance solar cells. One of the key factors determining the monodispersity of the dots was the speed with which the sulfur precursor was injected into the heated lead precursor solution. Because the entire mixture is already under the high heat at which reaction and growth take place, slow injection of the sulfur leads to more polydisperse dots. As soon as sulfur enters the lead solution, it reacts with the lead oleate and dots begin to grow. In an idealized case in which all the sulfur enters the solution at precisely the same moment, dots begin growing at the same time and result in a highly monodisperse particle size distribution. However, if the sulfur is introduced slowly and over a prolonged time period, the dots that begin growing when the sulfur is first introduced will continue to grow throughout the length of the injection period. As a result, they will be much larger than dots that begin growing as a result of sulfur injected several moments later at the end of the injection period. This reality makes the actual mechanics and manual execution of PbS synthesis very important, something mastered with practice.
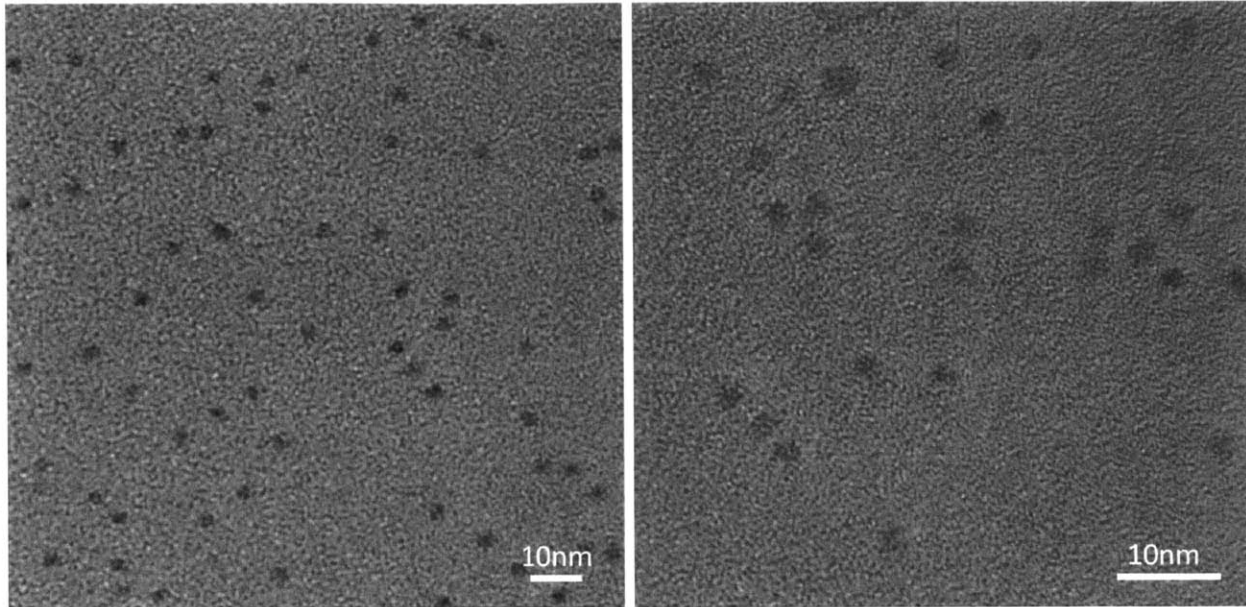
Figure 19. TEM micrographs of as-synthesized PbS quantum dots.

We further studied the dots with powder X-ray diffraction (Figure 20). The peaks (labeled in Figure 20) correspond to face-centered cubic PbS. Additionally, the broad peaks are consistent with a nanocrystalline material. By contrast, powder diffraction of single crystalline or very large grained crystalline materials exhibit high intensity peaks with very narrow widths. Given that our dots are only a few nanometers in diameters, the broad X-ray peaks observed in the diffractogram are consistent with our visual observations from the TEM as well as with previous studies [77].
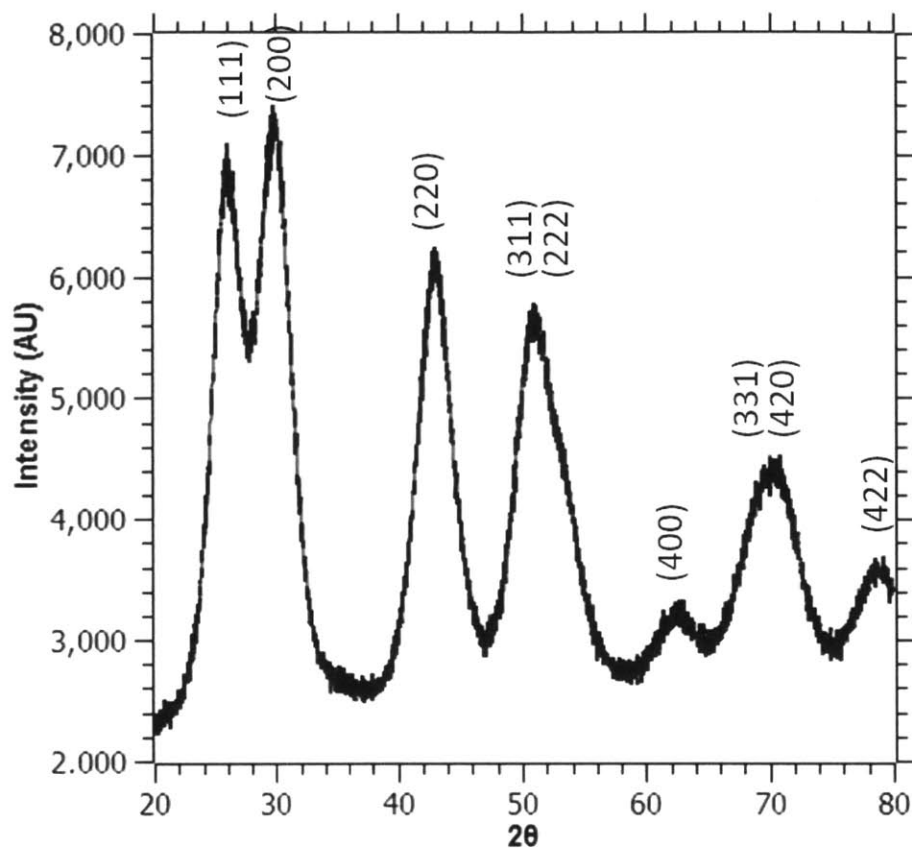
Figure 20. Powder X-ray diffractogram of as-synthesized PbS quantum dots.

Finally, we studied how the size and light absorption of our dots changed with different reaction temperatures. As presented in Figure 21, the quantum confinement nature of PbS dots in the studied size regime enables us to easily tune the size of the dots we use in our devices as well as the amount of light those dots absorb, a general property of materials that exhibit quantum confinement. In our particular case, because of lead sulfide's rather large Bohr exciton radius of 18nm, PbS particles with sizes less than that will exhibit quantum confinement [44]. As the particle size shrinks, the apparent energy gap of the semiconductor expands because the available

energy states are no longer continuous. They become discrete and, as such, size-dependent. As a result, the first excitonic peak in the UV-vis absorption spectrum, which corresponds to the apparent energy gap, will blue shift to higher energies. Table 1 summarizes these changes and how they are connected to the dot's synthesis temperature. For instance, the dots used for the devices fabricated in this work were synthesized at a reaction temperature (aka, the injection temperature, or the temperature at which the sulfur precursor is rapidly injected into the heated lead oleate solution) of 125°C. This results in dots that are approximately 3.1nm in diameter, which corresponds to an energy gap of about 1.3eV, in agreement with previous work in the literature [44, 67]. This is observed in UV-vis spectra as a peak in absorption at around 960nm. However, by increasing the reaction temperature to, say, 150°C, dots of up to 3.5nm in size can be made, corresponding to an energy gap of 1.18eV and an absorption peak at 1053nm. To further extend this explanation, as the particle size grows, the energy gap shrinks until quantum confinement no longer exists and the material exhibits its bulk energy gap (0.37eV for PbS) [41].
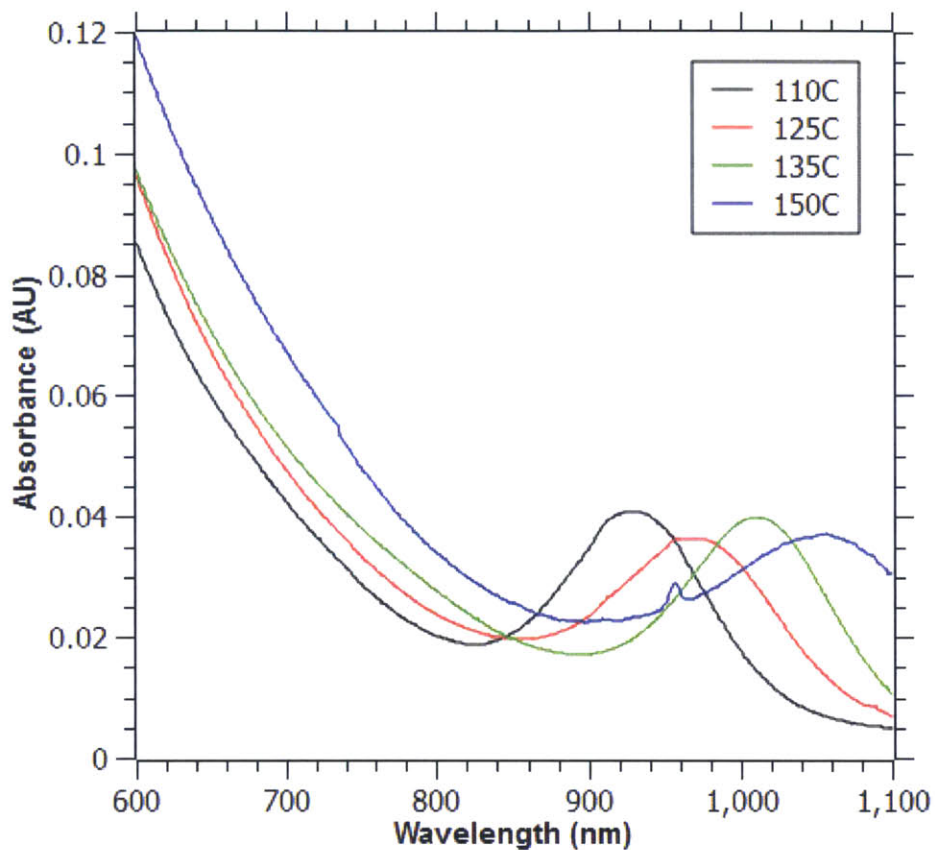
Figure 21. UV-vis absorption spectra of PbS quantum dots synthesized at different reaction temperatures.

Size [nm]	3.0	3.1	3.3	3.5
λ [nm]	930	959	1011	1053
Bandgap [eV]	1.33	1.29	1.23	1.18
Injection T [°C]	110	125	135	150

Table 1. Summary of how PbS quantum dot reaction temperature affects ultimate dot size and its resulting optical properties.

Because the particle size determines the particle's electronic energy gap and its subsequent ability to absorb light, tight control must be executed over the size distribution of the dots to be used in functional photovoltaic devices. Particle samples with a wide particle size distribution don't exhibit the well defined absorption peaks shown in Figure 21. Instead, the absorption profile is amorphous and gradual with no sharp peaks or features, a necessary condition for use of these materials in solar cells. Individual particles of different sizes will have energy band edges located at a range of different wavelengths. Thus, for particle collections with high polydispersity, no single band edge absorption dominates, and as a result, no absorption peak is observed. Using active materials with well defined energy gaps is also critical to ensuring that the device has a well defined photovoltage. The open circuit voltage (V_{oc}) of a solar cell is dependent on, among other things, the energy levels of the constituent semiconductors used in the device's photoactive layer. Accordingly, for a device to have a well defined V_{oc}, it must use semiconductors with well defined energy levels and energy band edges.

Quantum Dot Passivation

To be suitable for use in practical and functional solar cells, quantum dots must be electronically passivated by surface ligands. While the oleate ligands that the dots are synthesized with help them maintain exceptional dispersion stability in organic solvents like octane or toluene, they also serve to passivate electronic trap states inside the energy gap of the semiconductor. These energy trap states residing inside the otherwise forbidden energy gap can serve as defect sites where previously excited electrons and holes can easily recombine before they are extracted from the device as useful current. Well chosen passivating ligands can help to eliminate these deleterious trap states. It has been suggested that one reason for this is that these ligands, like

oleate, help prevent oxygen from reacting with the dot's surface, where they can produce various oxidation products like $PbSO_4$ or $PbSO_3$, particularly for smaller dots, and that it is these surface oxidation products that introduce unwanted energy midgap trap states into the energy gap [44]. So by preventing surface oxidation of the dots, ligands can prevent the introduction of electronic surface traps.

Figure 22 presents FTIR analysis of our PbS dots. As indicated, in the presented wavenumber range of interest, two strong absorption peaks are present at $2849cm^{-1}$ and $2918cm^{-1}$, which correspond to the symmetric and asymmetric stretching vibrations of the C-H bonds present in the long chain oleate molecules. However, when these ligands are removed by solid state ligand exchange with MPA during device fabrication, the peaks are notably depressed. This is consistent with our exchange of a long chain hydrocarbon for the much smaller MPA molecule. It is important to note that the peak at these wavenumbers isn't completely removed in the sample treated with MPA, likely indicating that short chain MPA remains surface bound to our dots as a passivating ligand.
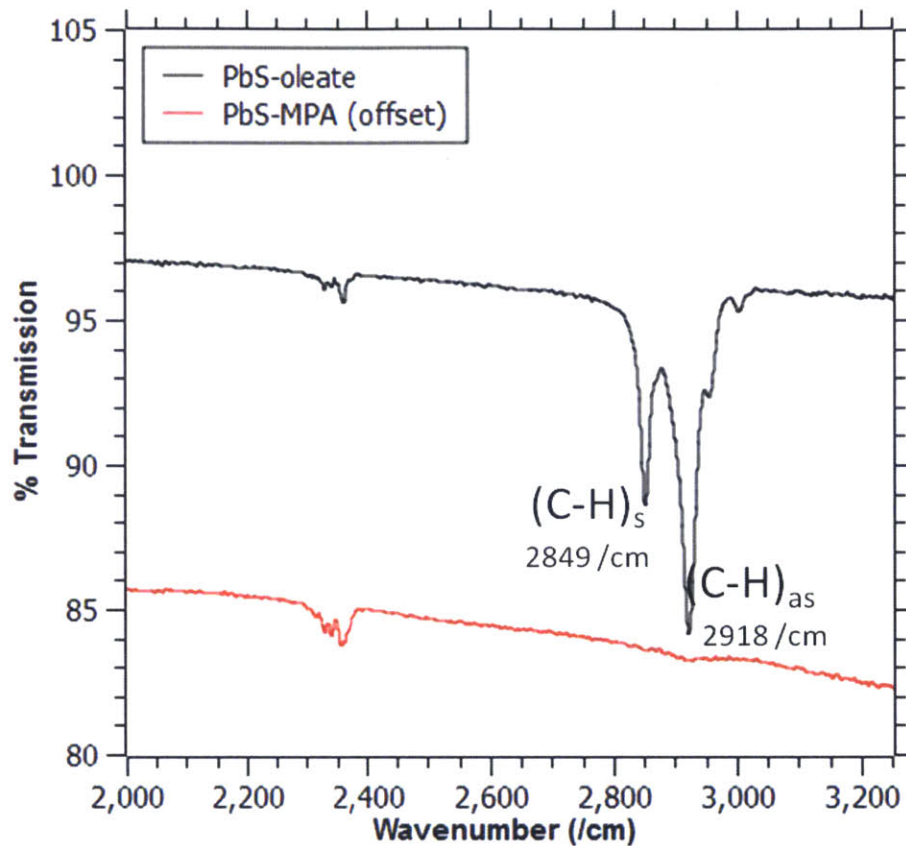
Figure 22. FTIR spectra of PbS quantum dots capped in oleate (as-synthesized) and capped with 3-mercaptopropionic acid (ligand exchanged during device fabrication).

This is necessary to do to fabricate high performing devices. With such long chain (and electronically insulating) ligands like oleate, PbS dots can't pack nearly as close to each other when deposited as a thin film in a device. But, in order to facilitate efficient inter-particle charge carrier transport through the device, the dots must be packed as close to each other as possible. Completely removing the ligand so that the dots may pack directly against one another isn't a feasible option either, as the dots must still be electronically passivated to prevent rampant

oxidation and the introduction of surface defect trap states that would critically hinder device operation. Thus, by exchanging a long chain ligand with a small molecule ligand, the dots can pack much more closely to each other to enable charge carrier transport between dots and through a film or device, while still retaining their surface electronic passivation.

Aside from the steric benefits afforded to the QDs upon ligand exchange with a much shorter chain molecule, MPA has also been shown to have a relatively improved distribution of midgap trap states relative to other ligands such as oleate and even EDT [52]. That is, the distribution of midgap trap states present in MPA passivated QDs is much shallower. As a result, charge carriers that fall into those traps have a comparatively easier time gaining the necessary energy to escape them. Ligands such as oleate and EDT have trap distributions that are relatively deeper, causing carriers that fall into them to remain trapped for longer periods of time, resulting in a loss of useful photocurrent.

While we don't have direct evidence that our dots are packing more closely or more densely in a film when they are passivated with MPA, rather than with oleate, previous research has indicated that this is very likely the case [78]. Kuo, et al., used TEM and synchrotron X-ray reflectivity to show that when they replaced the oleate ligands on PbSe dots with shorter chain ligands, such as ethanedithiol (EDT), the average film density increases quite significantly (from 1.86g/cc for oleate-PbSe to 4.69g/cc for EDT-PbSe) and the spacing between particles decreased significantly as well (thin film surface normal d-spacing dropped from 6.83nm for oleate-PbSe to 4.72nm for EDT-PbSe). This latter observation is particularly critical for device operation, as charge carriers must travel along the suface normal in order to be extracted by the electrodes.

Finally, we used surface XPS surveys to confirm that our dots, in addition to being capped and passivated with oleate, are also capped and passivated with Cl⁻ anions in the desired "hybrid

passivated" scheme. As shown in Figure 23, in addition to the expected peaks for Pb and S, additional significant peaks are also present for chloride 2s and 2p orbitals, confirming the existence of surface bound halide ions on our dots. These additional atomic passivating ligands provide an additional barrier to surface oxidation of the dots and the resulting electronic degradation that follows. Density functional theory was previously used to show that these atomic halide ligands are small enough to occupy the trenches in between cations on the surface of the dots, valleys that can't be occupied by the larger organic ligands due to steric hindrance [53].
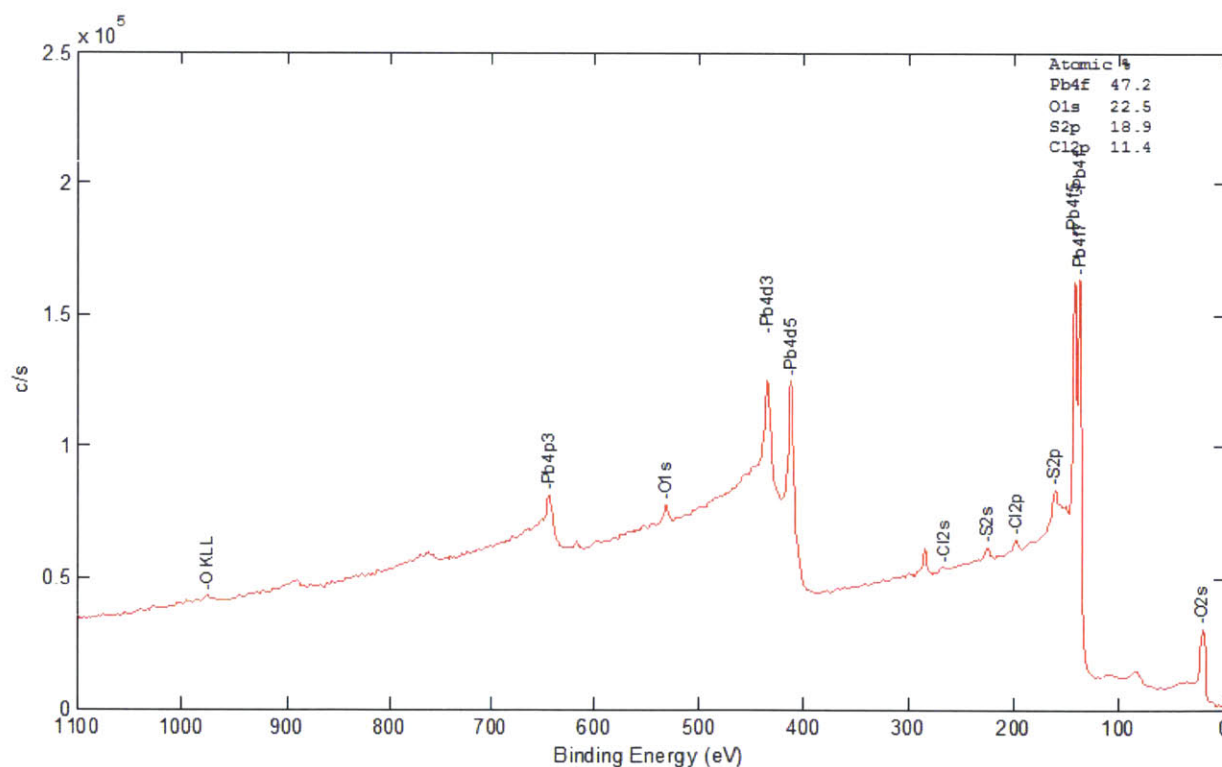
Figure 23. XPS survey of PbS quantum dots surface passivated with oleate and with Cl⁻ anions.

Synthesis and Characterization of TiO$_2$ Nanocrystals

Materials

Titanium (IV) butoxide (97%), oleylamine (technical grade, 70%), and oleic acid (technical grade, 90%) (OA) were purchased from Sigma-Aldrich and used as received.

Methods

In a typical synthesis, 5mmol of titanium butoxide, 30mmol of oleic acid, and 20mmol of oleylamine were mixed thoroughly with 100mmol of ethanol. The solution was then transferred to a Teflon-lined stainless steel autoclave and baked in a high temperature furnace for the desired time and temperature. After being allowed to cool down naturally to room temperature, the nanocrystals were isolated and washed with several centrifugation cycles. The nanocrystals were precipitated with excess acetone and re-dispersed in toluene. After at least 3 similar wash cycles, the precipitates were stored as a dry powder in a vacuum dessicator.

To control particle size, we primarily used baking time and temperature. While the other synthesis parameters (such as titanium and ligand concentrations) from similar synthetic routes have also been shown to influence particle size, many also influence particle shape [79-81]. For the purposes of this work, however, we sought particles that were as close to spherical as possible. This was a critical requirement. In order to form densely packed thin film blends for our bulk heterojunction devices, we needed particles that were spherical or spheroid, not faceted, branched, or otherwise less symmetric, since they were to be mixed, blended, and deposited with PbS QDs, another spherical nanocrystal. Accordingly, we modified a pre-existing synthesis

procedure for such "shape-controlled" anatase titania nanocrystals to obtain spherical or spheroid particles instead.

Transmission electron microscopy (TEM) was performed on a JEOL 2010 TEM. Powder X-ray diffraction (XRD) spectra were obtained on a PANalytical X'Pert Pro X-ray powder diffractometer. Fourier transform infrared spectroscopy (FTIR) was performed on a Jasco FTIR spectrometer. Image analysis of TEM micrographs was performed using ImageJ in order to analyze particle size distributions. Ninety-seven particles were counted for each analyzed image.

Nanocrystal Structure

We studied the synthesized titania nanocrystals through transmission electron microscopy. Figure 24 presents TEM micrographs of various nanocrystal samples synthesized over a range of different temperatures, but at a constant reaction time of 8 hours. With an increase in reaction temperature from 175°C up to 250°C, the obtained nanocrystals grow slightly larger. In all samples, the synthesized nanocrystals were generally spherical or only slightly elongated. Because our synthesized nanocrystals were not highly faceted, branched, or otherwise strongly asymmetrically shaped, they were easily mixed and blended with our spherical PbS quantum dots and subsequently cast into dense blended thin films for use in our solar cells.

It is also qualitatively evident from the micrographs that the particles have a very large particle size distribution. Unlike our PbS quantum dots, the titania nanocrystals produced here are not tightly monodisperse. While this lack of precise size control could seem undesired, polydisperse particles have been found to form more densely packed solids [82]. The reason for this is that the smaller particles will fill the void space in between neighboring large particles or by layering on top of or in between adjacent layers of larger particles [83]. Thus, when mixed with our PbS

quantum dots, we expect our approximately spherical, polydisperse titania nanocrystals to pack very well and to form highly dense solid films, ideal for use in bulk heterojunction solar cells. Aside from the advantages that polydisperse particle collections have when forming solid films, it is not strictly necessary for our titania nanocrystals to be monodisperse in order for proper electronic functioning of our devices. This is largely because anatase titania has an energy gap well beyond that of visible light (~3.2eV) [84]. Accordingly, it does not participate in light absorption in the device to an appreciable degree and any quantum confinement effects that the nanocrystals may exhibit would only increase that absorption edge even further beyond the useful operating range for a solar cell.
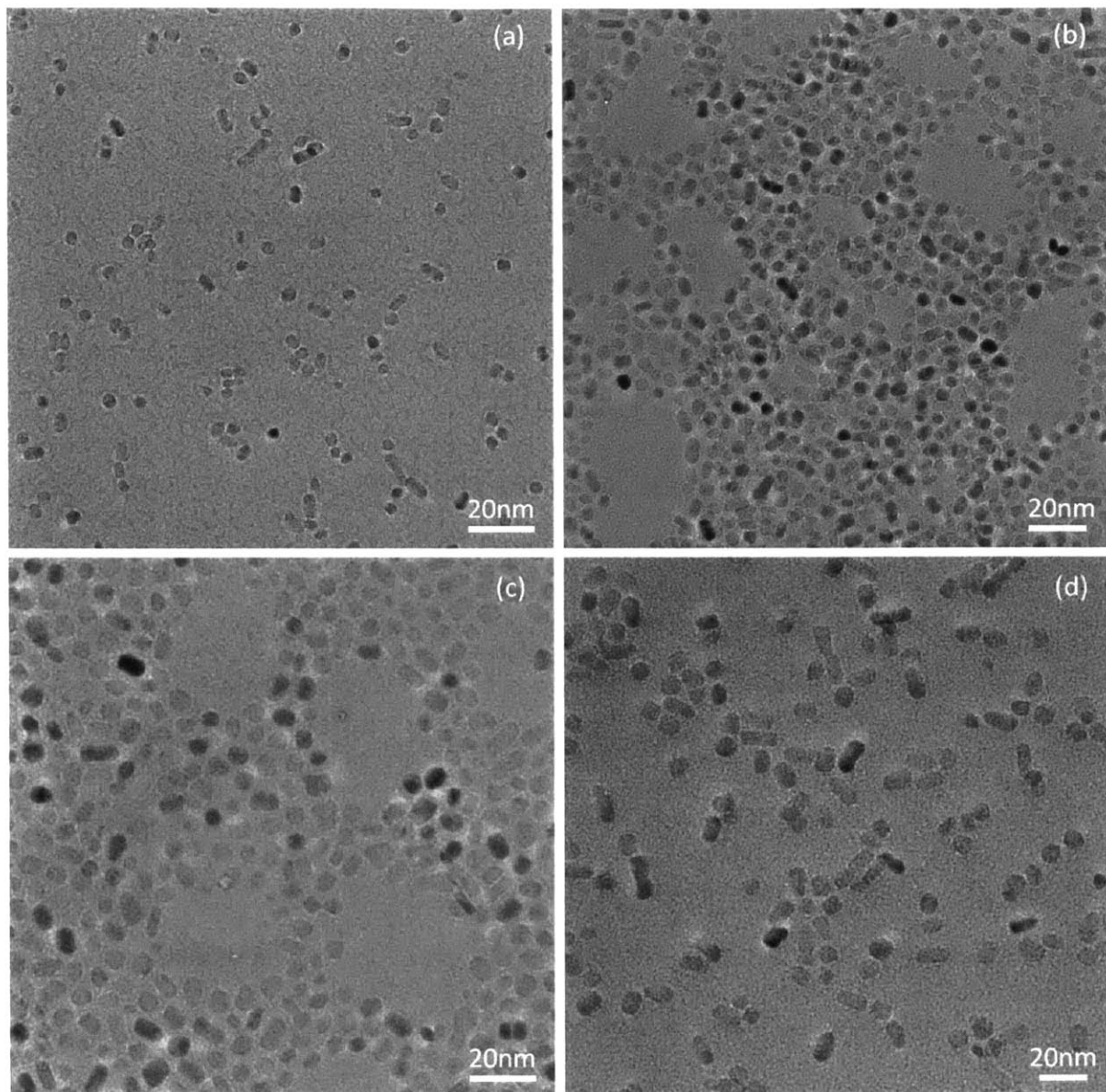
Figure 24. TEM micrographs for titania nanocrystals synthesized for 8hr at (a) 175°C, (b) 200°C, (c) 225°C, and (d) 250°C.

We also investigated the effect of reaction time on the growth of our titania nanocrystals (at constant reaction temperature). Figure 25 presents TEM micrographs of various nanocrystal samples that were grown at 175°C for times ranging from 8 hours up to 20 hours. The produced nanocrystals are, as expected, extremely similar in nature to those produced by varying the reaction temperature. Larger particles are produced at longer reaction times. They appeared to be approximately 10nm in size, approximately spherical or only slightly elongated, and polydisperse.

It might be expected that nanocrystals synthesized at higher temperatures would be more spherical, due to the greater energy supplied for enabling the growth of even high energy crystal facets. That is, at low synthesis temperatures, it is not unreasonable to expect faceting, as there is only enough energy to enable the growth of the lowest energy (and thus growth favored) crystal planes. At higher temperatures, however, these considerations become less critical, as even higher energy crystal planes should grow. In our rudimentary qualitative survey of the nanocrystals produced here, it appears as though nanocrystals synthesize at 175°C are similar in shape to those synthesized at 250°C. It is possible that even 250°C is not high enough for the growth of all crystal planes, not just the lowest energy facets, to be favored. It is also possible that the relative concentrations of the titanium precursor and the two ligands (oleic acid and oleylamine) restrict the growth kinetics in such a way that even slight elongation of the nanocrystals is unavoidable, regardless of the reaction temperature. It was, in fact, these relative concentrations that have previously been used to obtain anatase nanocrystals of different, well defined shapes [80]. The two different ligands have different binding strengths for the various crystal facets of the growing titania nanocrystals and, as a result, they can be used to tune the comparative growth rates of the different facets to obtain nanocrystals of different shapes.
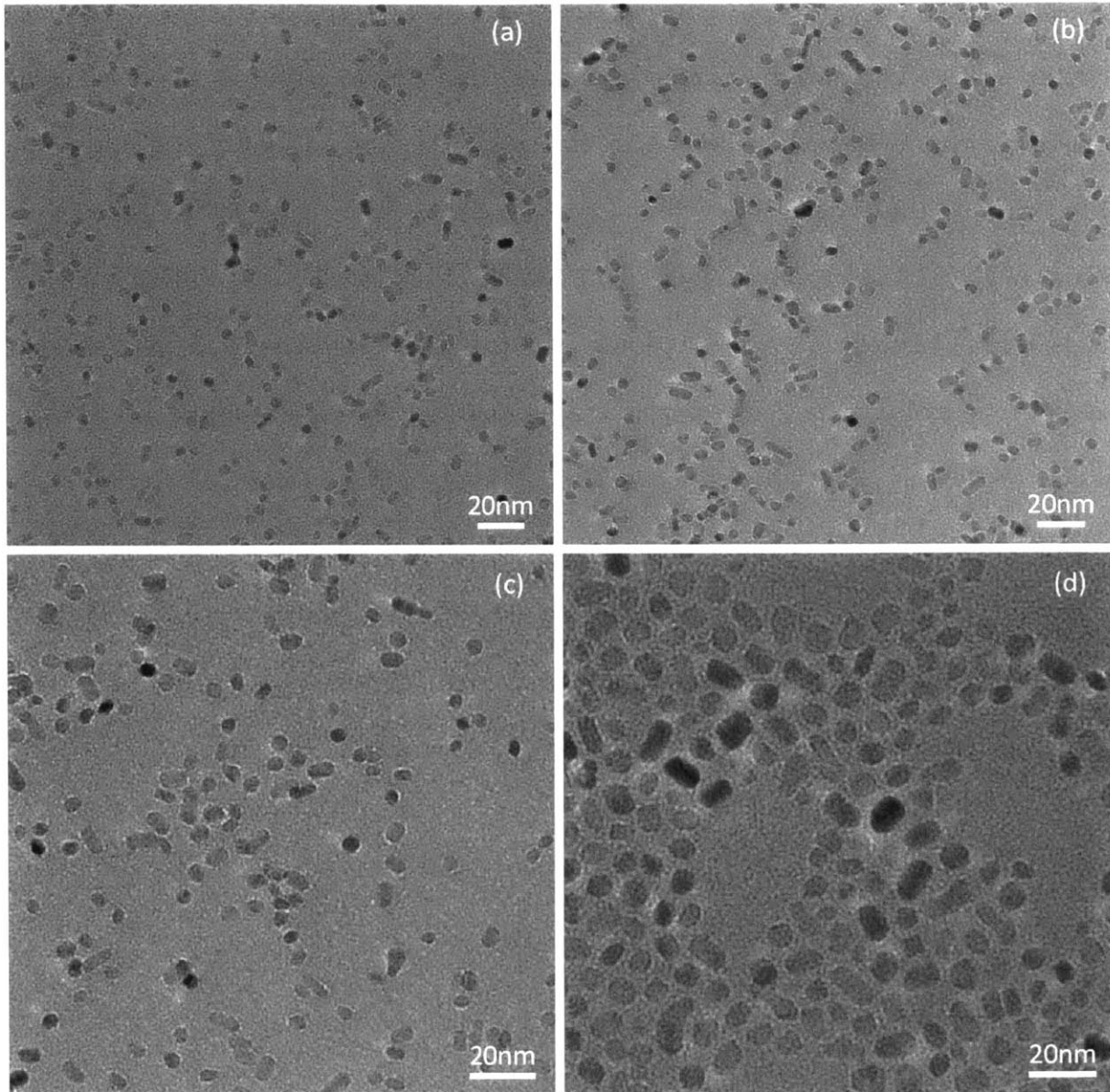
Figure 25. TEM micrographs for titania nanocrystals synthesized at 175°C for (a) 8hr, (b) 12hr, (c) 16hr, and (d) 20hr.

To further illustrate the polydispersity of our titania nanocrystals, size histograms at the various time and temperature reaction conditions are presented in Figure 26. The degree of polydiserpsity is evident from the broad distributions and tails illustrated in the various

histograms. With the exception of the samples in Figure 26(c) and (f), the particle size distributions are fairly symmetrical around the mean. And in most cases, the longer tail of the distribution extends out toward larger nanocrystal sizes. This may be a result of the procedure used to calculate particle size from the image analysis. Because most of the particles are approximately spherical or only slightly elongated, the areas calculated from image analysis were assumed to be areas of a circular particle. Particle sizes (diameters) were then calculated based on the area of a circle. As a result, particles that were slightly elongated yielded larger areas that resulted in larger calculated diameters. Meanwhile, the diameters of many of the spherical particles were similar to the lengths of the short axes of the elongated particles, not the long axes. The ultimate effect of this is that the elongated particles were calculated to have larger "effective diameters," resulting in broad particle size distributions that contained particles of many different sizes, and most often skewing out toward larger particle sizes.
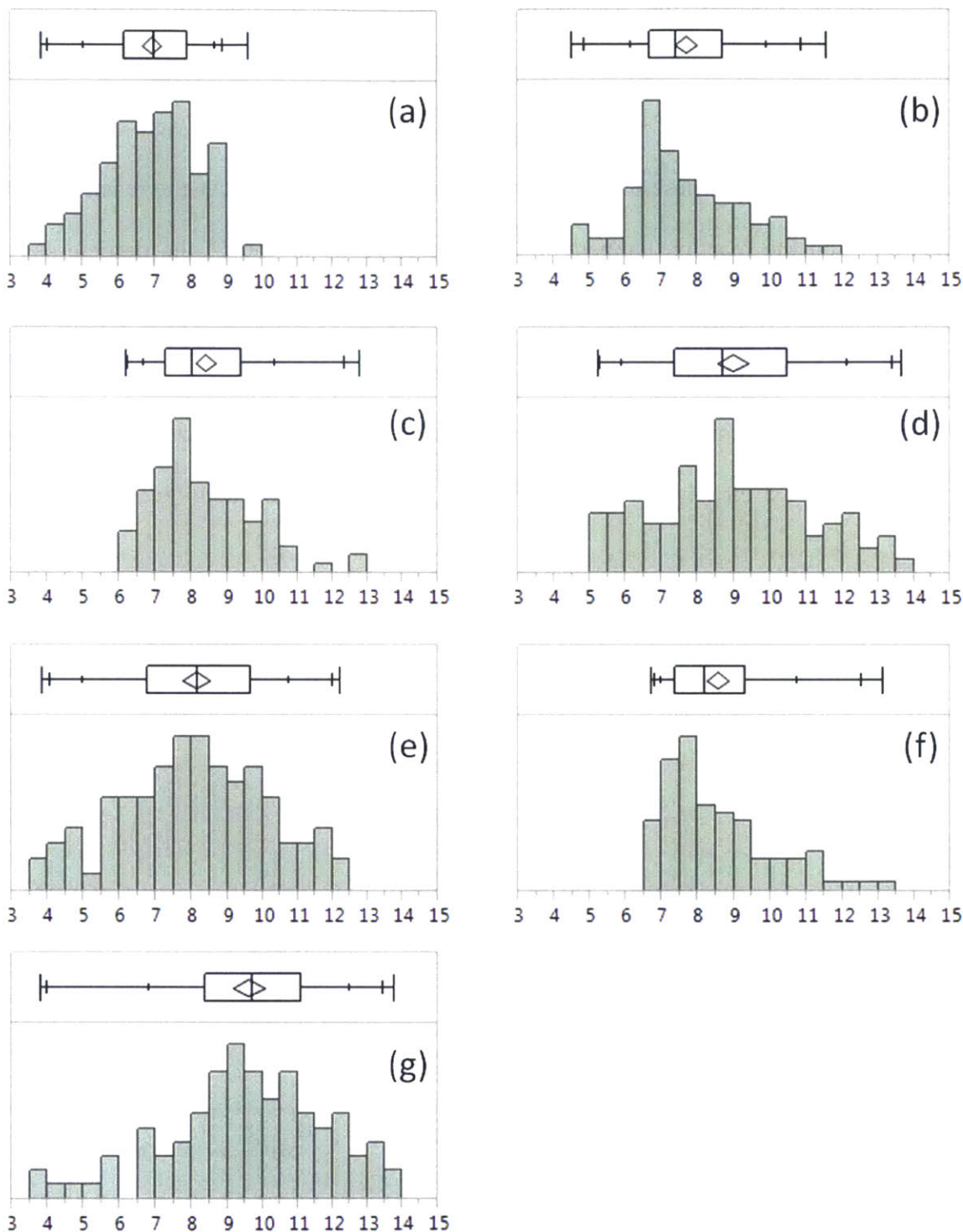
Figure 26. Size histograms for titania nanocrystals synthesized at (a) 175°C for 8 hours, (b) 200°C for 8 hours, (c) 225°C for 8 hours, (d) 250°C for 8 hours, (e) 175°C for 12 hours, (f) 175°C for 16 hours, and (g) 175°C for 20 hours. Quantile boxes for each histogram are also presented. The rectangle boxes bound the standard deviation around the mean (indicated by the diamond) and the median (indicated by the short vertical line in the middle of each box).

To more clearly illustrate the dependence of nanocrystal size on our studied synthesis parameters, Figure 27 presents plots of nanocrystal size as a function of synthesis temperature and, separately, as a function of synthesis time. The smallest nanocrystals were obtained from 8 hour reactions at 175°C. These had an average diameter of 6.92nm. As the reaction time was held constant and the reaction temperature was increased up to 250°C, the particle size grew slowly to 8.97nm. When the reaction time was increased up to 20 hours, at a constant reaction temperature of 175°C, the nanocrystals grew to an average size of 9.45nm. For the purposes of solar cell fabrication, the smallest obtained nanocrystals, those 6.92nm in size, were used, as they are the particles most closely matched in size to our PbS quantum dots (average diameter of 3.1nm).
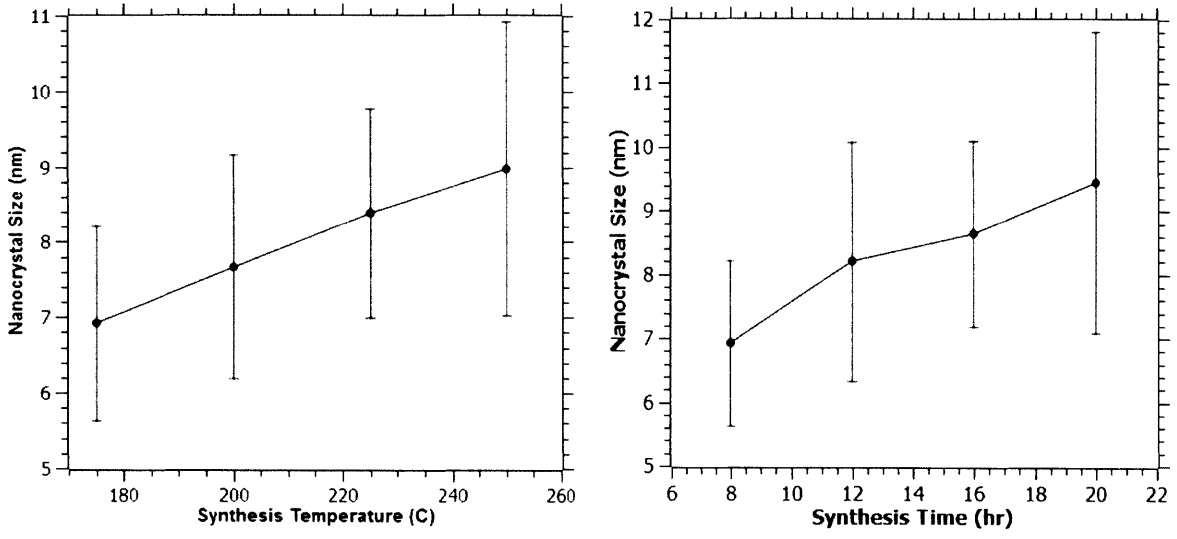
Figure 27. Titania nanocrystal size vs. synthesis temperature (at an 8 hour reaction time) and time (at a reaction temperature of 175°C).

Further insight into the structure of our titania nanocrystals was obtained from powder X-ray diffraction studies of our particles. As presented in Figure 28, our titania nanocrystals are indeed antase crystalline, matching the diffraction peaks for anatase titania, a tetragonal crystalline material. Anatase, rather than rutile, is the preferred titania phase for use in solar cell applications, given that it has more favorable energy level positioning relative to the photoactive semiconductors, like PbS, typically used in photovoltaics. The bulk anatase exhibits very sharp, high intensity, low width peaks, characteristic of a highly crystalline material with large crystallite sizes. By comparison, the diffraction peaks for our nanocrystals are much shorter or lower intenseity, and they exhibit comparatively larger peak widths, indicative of a small grained or nanocrystalline material. This is consistent with the small particle sizes of our nanocrystals. For illustrative purposes, Figure 28 also presents the spectrum of amorphous titania, which doesn't exhibit any well defined scattering peaks.
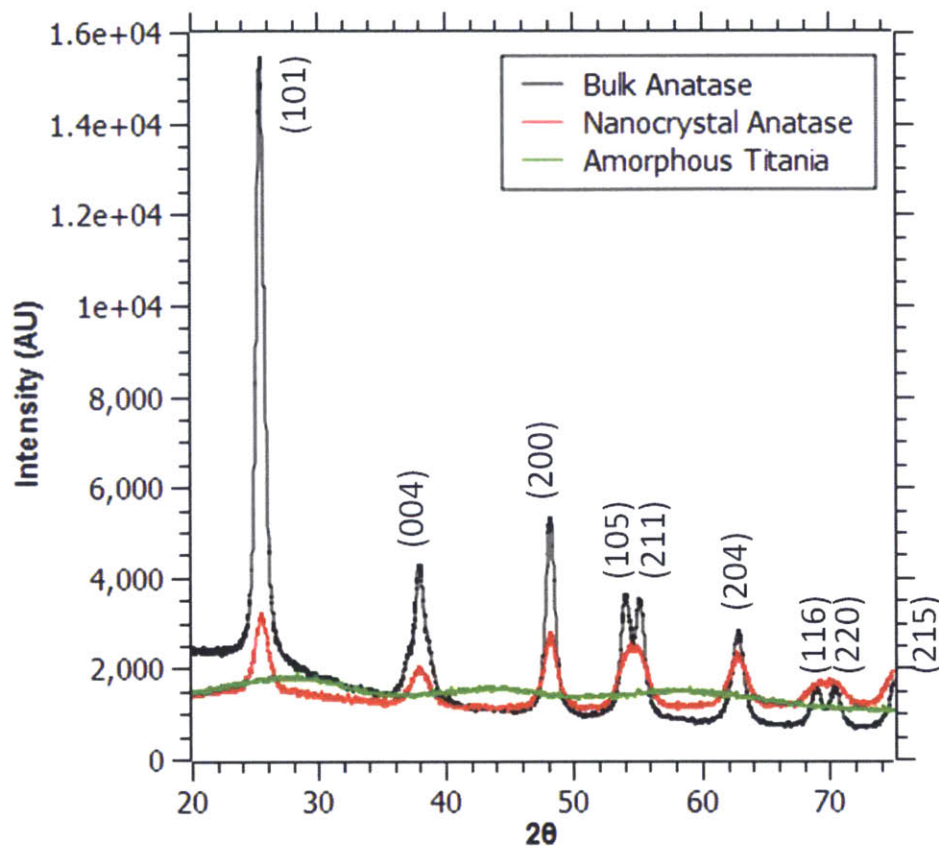
Figure 28. XRD spectra of bulk crystalline anatase titania, amorphous titania, and our synthesized anatase titania nanocrystals.

XRD analysis was performed on our titania nanocrystals over the temperature and time ranges of study here. As seen in Figure 29, very little difference is observed between nanocrystals synthesized at 175°C versus those synthesized at 250°C (and similarly, for those synthesized under constant reaction conditions for 8 hours versus those synthesized under the same reaction conditions for 20 hours). The similarity of these diffractograms results from the small change in size over the reaction conditions studied here. Furthermore, the nanocrystals synthesized at all reaction conditions remained anatase and were all approximately spherical or only slightly

elongated. This latter attribute is evident in the diffraction patterns as well. Were our nanocrystals extremely elongated or, for that matter, nanorods or nanowires, the second peak (that representing the (004) plane) would have a significantly higher relative peak height [79, 80] compared to the other remaining peaks, especially the (200) peak. Because it does not and because the relative peak heights of our nanocrystals follows those of bulk anatase titania, it provides supporting evidence that many of our nanocrystals are approximately spherical crystallites.
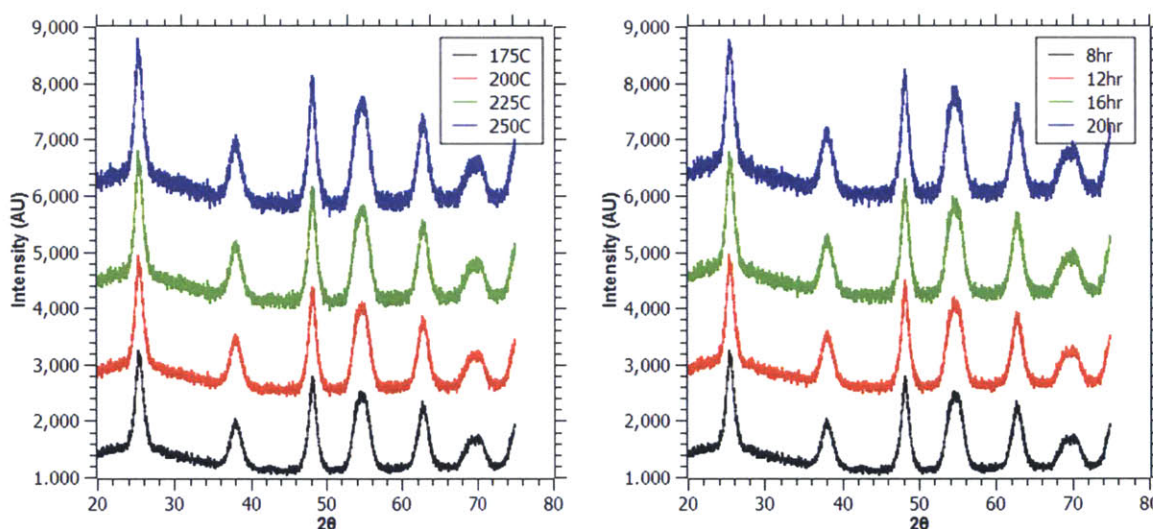
Figure 29. Evolution of titania nanocrystal structure over the reaction temperature and reaction time ranges studied.

Nanocrystal Ligands

Finally, to ensure that our as-synthesized anatase nanocrystals possess the proper ligands for dispersion stability in the same organic solvents as our PbS quantum dots, we analyzed our

nanocrystals under FTIR. As shown in Figure 30, our anatase nanocrystals exhibit the same strong C-H stretching vibration peaks that our quantum dots exhibited, indicative of the C-H bonds in the long chain hydrocarbons, oleic acid and oleylamine, capping their surfaces. Furthermore, upon solid state ligand exchange during device fabrication, the oleic acid and oleylamine ligands were easily removed upon treatment with MPA ligand. A small peak is still visible in the FTIR spectrum, likely indicating that the much smaller molecule MPA remains surface bound to our nanocrystals in the same way they bind to our quantum dots.
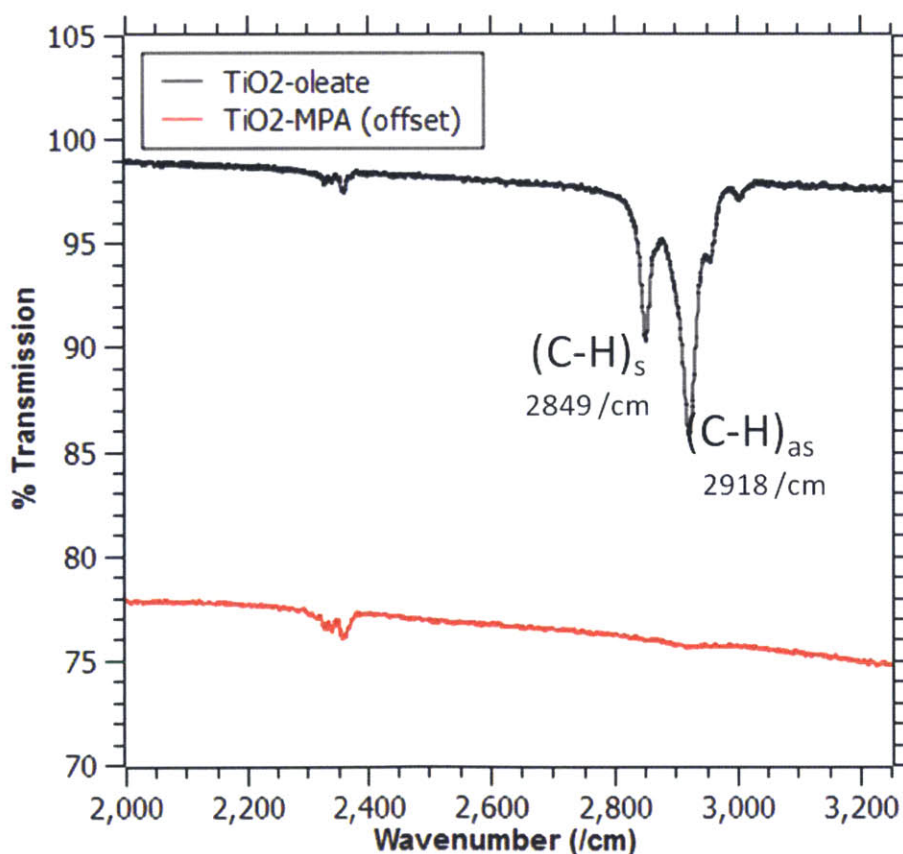
Figure 30. FTIR spectra of as-synthesized titania nanocrystals with oleate (and, to a lesser extent, oleylamine) capping ligands compared with nanocrystals whose ligands have been exchanged for MPA.

Chapter 3: Effect of Composition on Nanocrystal Bulk Heterojunction Photovoltaics

In this chapter, we fabricate, characterize, and test bulk heterojunction solar cells and study the effect that bulk heterojunction composition has on device performance. In particular, we find that PbS and titania are extremely evenly distributed throughout our bulk heterojunction blends (in both the in plane and normal to the place directions) at the length scales studied, such that charge carriers generated anywhere within the blend are well within a carrier collection length of a heterojunction interface. We studied bulk heterojunctions at three primary compositions, a PbS-rich blend, a TiO_2-rich blend, and a blend with equal volume fractions of each. We found that devices with a TiO_2-rich bulk heterojunction composition consistently outperformed devices employing other compositions. As a result of the size difference between the PbS quantum dots and the titania nanocrystals which compose the blends, the likelihood of forming a truly complete, bicontinuous bulk heterojunction network is maximized at a TiO_2-rich blend composition, and not at an even volume fraction split as would be the case for binary particle mixtures with equal sized constituents. In particular, enhanced light absorption and current generation was observed at infrared wavelengths, validating the ability of bulk heterojunctions to spatially extend the reach of the charge separating driving force, such that the previously missed red and infrared photons may be captured.

Materials and Methods

Titanium tetrachloride and 3-mercaptopropionic acid (>99%) (MPA) were purchased from Sigma-Aldrich and used as received. TEC 15 glass substrates coated in fluorine doped tin oxide (FTO) were purchased from Pilkington Glass. FTO, rather than the more widely used indium

doped tin oxide (ITO), was preferred because it does not degrade at the high temperatures required for various steps in the processing of anatase titania. When subjected to these high temperatures (~500°C), the electrical resistance of ITO substrates rises dramatically, beyond the range needed for practical usage in solar cells. Ti-Nanoxide HT/SC (titania nanoparticle paste) was purchased from Solaronix. This paste is a concentrated mixture of anatase titania nanoparticles (15-20nm in size), along with alcohol, water, and various organic binders. In order to be used in solar cells, these binding materials must be burned off in a high temperature bake, which also anneals the titania nanoparticles together. For all devices studied here, we used titania nanocrystals that were produced via the synthesis conditions that generated the smallest particles (typically 175°C for 8 hours). As previously described, the average size of these nanocrystals was approximately 6.92nm.

Lithographically patterned FTO substrates were cleaned sequentially in Micro-90 detergent, water, acetone, and isopropanol, followed by a 2min oxygen plasma treatment. A thin layer of TiO_2 was nucleated on the substrates by baking them in a 120mM $TiCl_4$ solution in water at 80°C for 30min. The substrates were then rinsed off in water and annealed at 500°C for 1 hour in a high temperature furnace. The thin anatase titania layer that results from this treatment helps the subsequently spincast titania or PbS nanocrystals to adhere to the substrate.

For devices employing unannealed anatase titania nanocrystal base layers (to be referred to as "nanocrystal base layers"), a 50mg/mL dispersion of titania nanocrystals in octane was dropped onto the substrate until it was completely covered. The substrate was then spun at 2500rpm for 10s. To exchange the as-synthesized oleate ligands on the nanocrystals with MPA, a 1% v/v MPA solution in methanol was then applied to the substrate and the substrate was then spun at

2500rpm for 10s. The substrate was then rinsed with methanol and spun again at 2500rpm for 10s. These three spincoating steps were repeated until a 150nm thick base layer was deposited.

For devices employing the commercial Solaronix titania paste base layers (to be referred to as "paste base layers"), the as-received Solaronix solution was dropped onto the substrate which was spincast for 60s at 3000rpm in order to achieve a film thickness of approximately 150nm. The substrate was then baked at 500°C for 1 hour in a high temperature furnace to sinter the particles together and remove the solvents and organic binders present in the paste.

The blend layers were prepared by mixing concentrated octane solutions of titania nanocrystals and PbS QDs in the desired volume fractions (obtained by using the material's density to convert from mg/mL) and then diluting the solution to 50mg/mL for spincoating. The mixed solution was dropped onto substrates, which were then spun at 2500rpm for 10s. MPA ligand exchange was carried out and the substrate was rinsed. These steps were repeated until a 100nm thick blend layer was deposited.

Finally, the cover layer of pure PbS was deposited by dropping a 50mg/mL solution of PbS QDs onto the substrate and spinning the substrate at 2500rpm for 10s. MPA ligand exchange was carried out and the substrate was rinsed. These steps were repeated until a 150nm thick PbS layer was deposited.

Top electrical contacts composed of 25nm of MoO_x and 100nm of Au were then thermally evaporated onto the devices.

Scanning electron microscopy (SEM), and the accompanying energy dispersive X-ray (EDX) analysis, was performed on a JEOL 6700F field emission scanning electron microscope. Cross sectional SEM imaging was done on a Helios Nanolab 600 Dual Beam Focused Ion Beam Milling System. X-ray photoelectron spectroscopy (XPS) analysis was performed on a PHI

Versa-Probe II spectrometer with a scanning monochromated Al source (1,486.6eV; 50W; spot size, 200μm). An argon source was used for sputtering and the zalar rotation was set at 1rpm. Roughness measurements were performed using a Veeco Dimension 3100 atomic force microscope (AFM). Thin film thickness measurements were determined using a Veeco Dektak 150 profilometer. Device performance data was measured using a solar simulator (150W Newport 96000 xenon arc-lamp, with AM1.5G filter and diffuser lens) that was calibrated to 100mA/cm^2 using a silicon reference cell. An external bias was applied to devices and the photocurrent was measured using a Keithley 6487 picoammeter.

Device Composition

The devices under study in this work have one of two general device structures illustrated in Figure 31. Bilayer devices were constructed in which PbS dots are deposited upon a titania base layer composed of either a nanoparticle paste (the commercially available Solaronix paste) or the anatase nanocrystals synthesized and studied in this work. Bulk heterojunction devices were constructed in which a blend layer is inserted in between the pure PbS layer and the pure titania layer. This blend layer is a binary mixture of PbS QDs and anatase titania nanocrystals. We studied three different blend layer compositions and their effect of device performance: blends with 25% PbS volume fraction, 50% PbS volume fraction, and 75% PbS volume fraction.
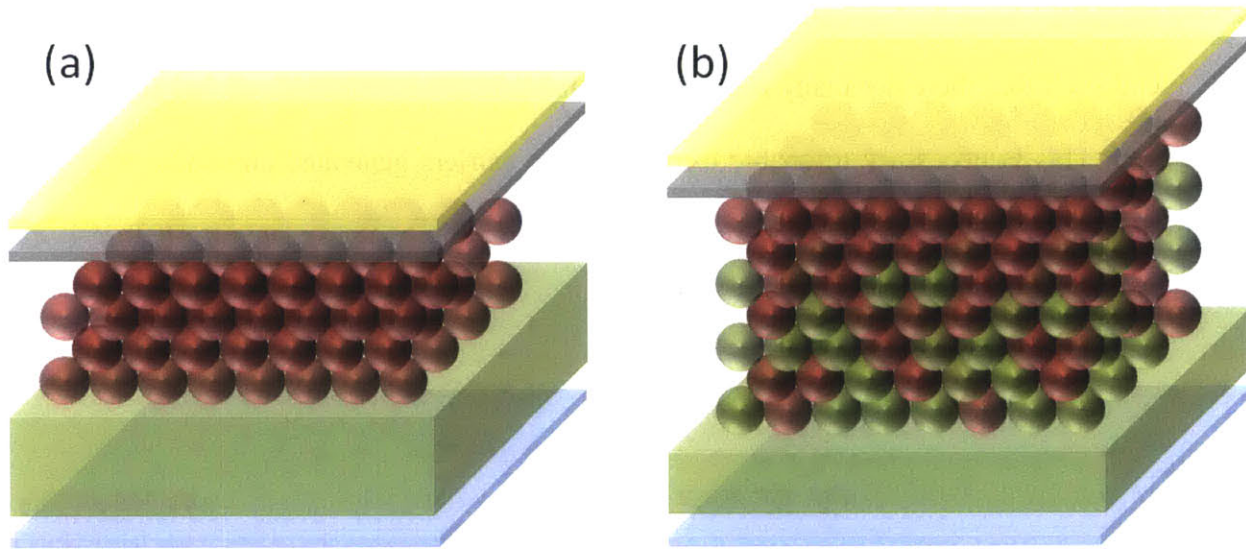
Figure 31. Schematic illustrations of (a) bilayer heterojunction device of PbS QDs and titania base layer composed of either nanoparticle paste or anatase nanocrystals, and (b) bulk heterojunction device of PbS QDs, a blend layer of QDs and titania nanocrystals, and a titania base layer composed of either nanoparticle paste or anatase nanocrystals. Blue = fluorine-doped tin oxide, Green = TiO_2, Red = PbS, Grey = MoO_3, Yellow = Au. Not to scale.

To examine the surface composition and uniformity of the blend layers used in the bulk heterojunction devices under study, EDX surface mapping was carried out. Spectral maps showing the distribution of Ti, O, Pb, and S across a large section of the blend layer's surface are presented in Figure 32. At this length scale and resolution, the distribution of PbS and titania across the surface plane of the film appears to be fairly even. Neither PbS nor titania appears to be forming large scale aggregates or isolated domains (certainly not at any length scales comparable to the carrier collection length of ~250nm), a morphological feature which would be deleterious to optimal charge carrier collection and device performance. The desired blend is one in which PbS and titania form a fine, even mixture throughout the length and depth of the device, similar to the way in which high performing polymer-fullerene bulk heterojunction solar cells have active layers that exhibit a fine scale, even blend with domains on the order of tens of

77

nanometers [85]. Similarly, for our devices to perform well, PbS and titania need to form a fine scale blend such that there are many bicontinuous channels of each phase spanning the depth of the device. This is necessary to enable excited charge carriers generated anywhere within the film to separate from each other and reach the appropriate extracting electrode before it can recombine.
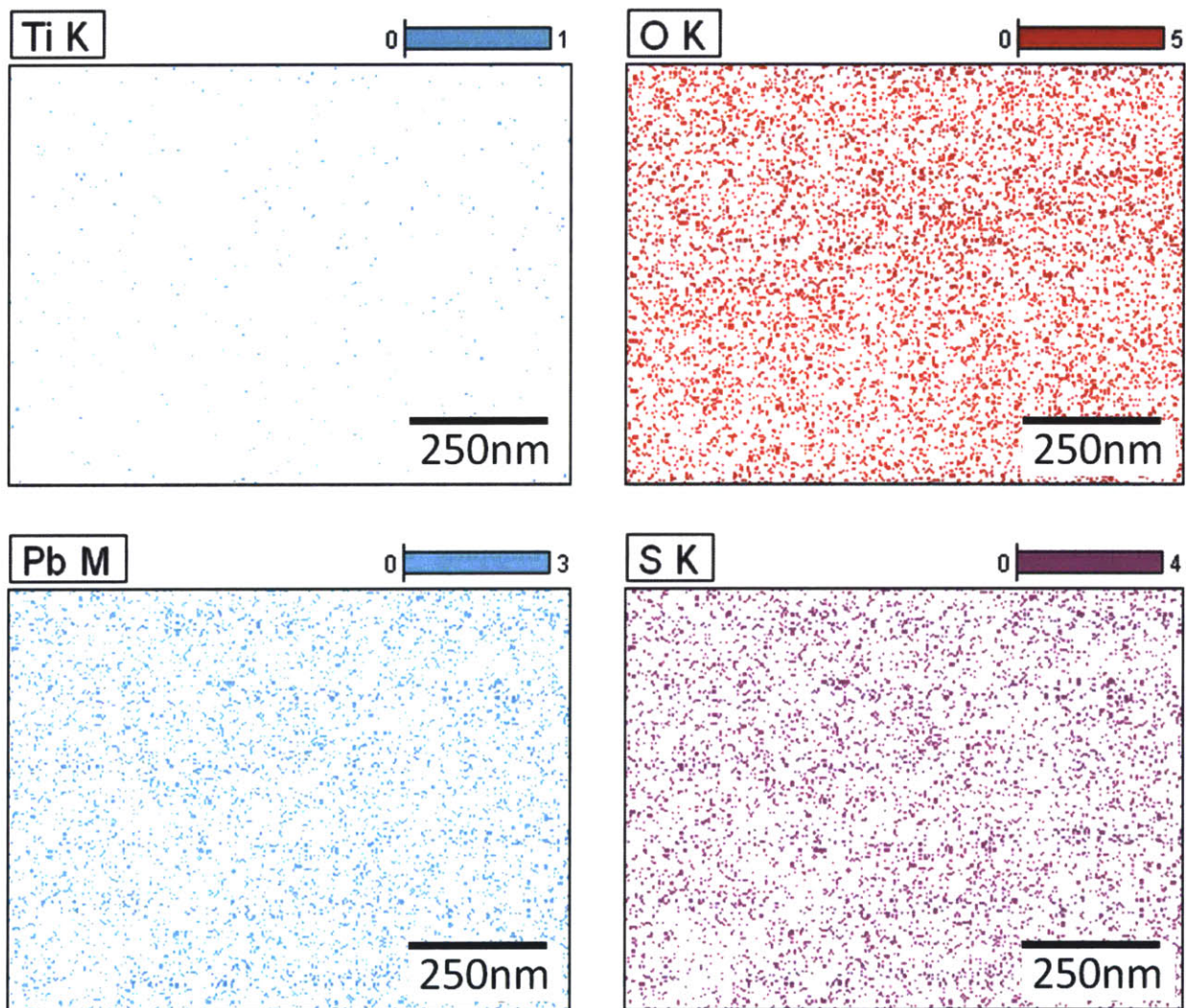
Figure 32. EDX surface maps of thin film blends of PbS quantum dots and titania nanocrystals from a bulk heterojunction device.

We also surveyed the surface of our device's layers with an XPS probe. The resulting elemental survey is presented in Figure 33. For comparison, we analyzed a pure film of PbS from a traditional bilayer device and a blend layer from a bulk heterojunction device. For the PbS layer from a bilayer device, labeled "layers" in Figure 33, peaks corresponding to Pb and S are expectedly present, while those for Ti and O are absent, indicating a pure PbS film, with little to no intermixing with the underlying titania layer of the device. In contrast, the XPS survey of the blend layer from the bulk heterojunction device shows peaks corresponding to Pb, S, Ti, and O, indicating the presence of both PbS quantum dots and titania nanocrystals across the exposed surface of the blend layer in the device, as was found with the EDX mapping.
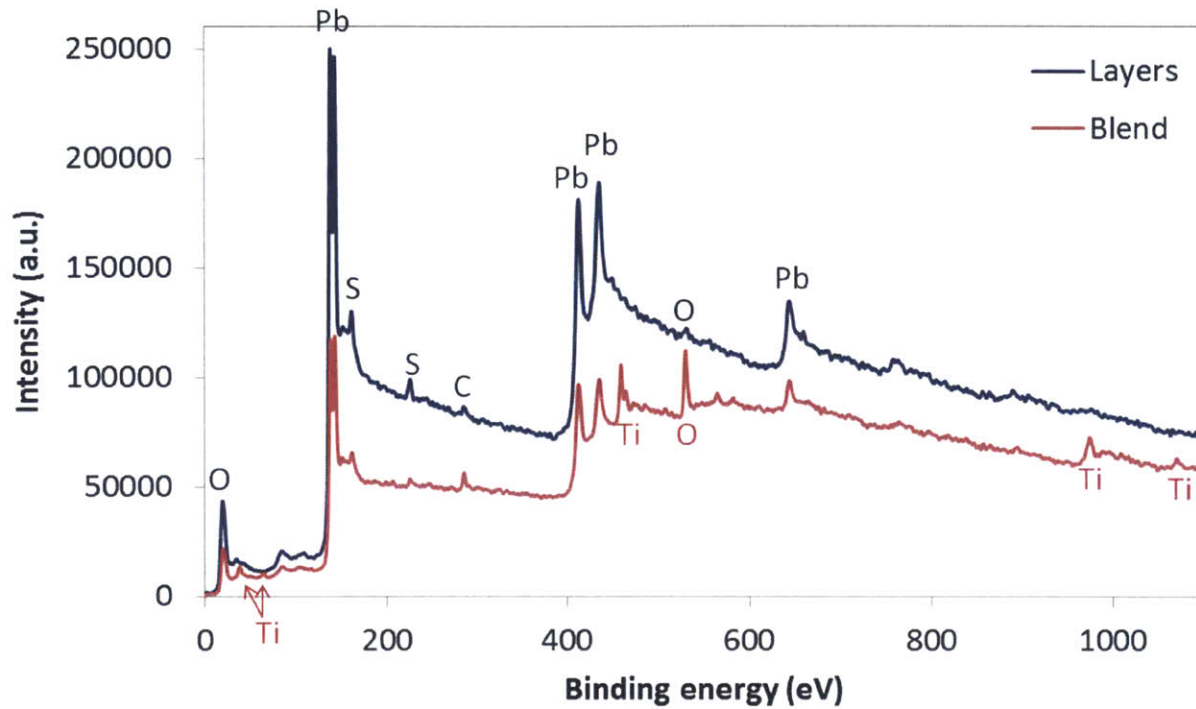
Figure 33. Surface XPS survey of a bulk heterojunction blend layer of PbS quantum dots and titania nanocrystals and a pure layer of PbS deposited over an underlying pure layer of titania.

While EDX and XPS surface elemental mapping provided insight into the distribution and composition of our device's layers, specifically the bulk heterojunction's blend layer, XPS depth profiling was used to examine the composition of the layers through the depth of our devices. Figure 34 presents an XPS depth profile of a pure PbS layer (100nm thickness) deposited on top of an underlying titania paste base layer, i.e., a traditional bilayer solar cell. A high concentration of Pb and S is present through the first approximately 80nm of the device. Over the next 40nm of depth, however, the concentrations of Pb and S decline while those for Ti and O increase. The atomic concentrations of O are almost twice those of Ti, consistent with titania's stoichiometric ratio. The atomic concentrations of Pb, however, are well above those of S, however. Previous reports have noted that the atomic ratio of Pb to S in PbS quantum dots

can indeed diverge significantly from the stoichiometric ratio, ranging anywhere from a Pb/S ratio of 1.2 to upwards of nearly 2 [44, 77, 86].

While the device analyzed in Figure 34 was a bilayer device in which the PbS layer was deposited on top of a planar titania paste base layer, it is evident from the XPS depth profile that the transition from PbS to titania is far from perfectly planar or discrete. The transition from the PbS layer to the titania layer appears to take place over the course of 40nm or more, indicating a degree of intermixing or interpenetrating between the two layers. AFM measurements indicate that the underlying titania paste base layer has an RMS roughness that can range from ~15nm to as high as 30nm (when deposited on silicon, the same substrate used for XPS analysis). Therefore it is not surprising that the transition from the "pure" PbS layer to the "pure" titania layer takes place over a wide depth window. This is also perhaps not a deleterious feature of this bilayer or "planar" device. The diffuse interface between the PbS and titania layers increases the interfacial area between the two. As a result, there's greater area or volume over which charge carriers generated in the PbS layer may be extracted through the titania layer. This is very similar to the underlying premise behind the use of a bulk heterojunction architecture in solar cells. By increasing the interfacial area between the p-type and n-type phases, it is possible to extend the volume over which light may be absorbed and charge carriers may be generated in the PbS that can still be efficiently extracted from the device. The interpenetration of the two phases allows charge carriers excited deep in the device or shallow in the device to still be extracted by separating and efficiently transferring to their respective phases (electrons in the titania and holes in the PbS). So while this is not strictly the case for the device analyzed in Figure 34, the diffuseness of the interface between the two layers likely has a similar, if more subdued, effect, owing to the roughness of the underlying titania paste base layer.
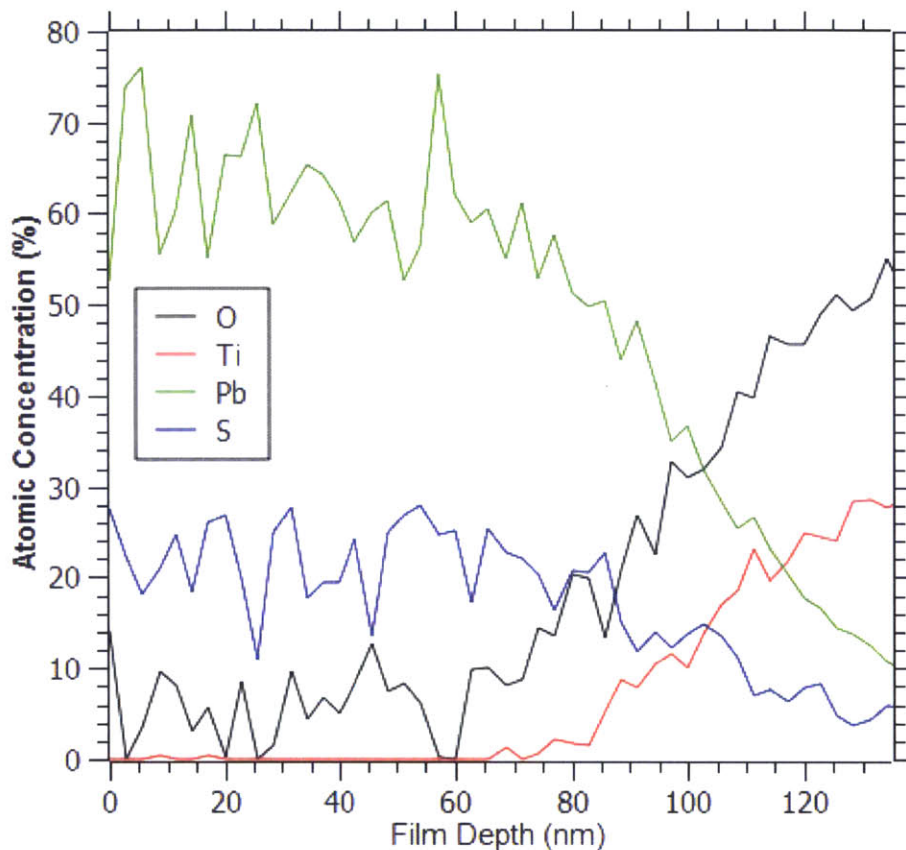
Figure 34. XPS depth profile of a bilayer device in which PbS is deposited on top of an underlying titania paste base layer.

We also examined the elemental composition through the depth of the blend layers used in our bulk heterojunction devices with XPS. For the present work, we examined three different bulk heterojunction blend layer compositions: (a) 25% volume fraction PbS, (b) 50% volume fraction PbS, and (c) 75% volume fraction PbS. Depth profiles for these three compositions are presented in Figure 35. The atomic concentrations obtained by the XPS can be roughly converted to volume fractions by using the molecular weight and density of PbS and titania. For instance, while the film analyzed in Figure 35(b) has extremely high atomic concentrations of O

and Ti relative to the concentrations of Pb and S, this particular blend layer had an approximate volume concentration of 50% PbS quantum dots and 50% titania nanocrystals. Throughout the 100nm blend layer film depth (normal to the plane) analyzed, the film composition remained relatively consistent, with only small scale variations in local composition, for all compositions studied. Together with our previous elemental analysis of the surface (in plane) of our bulk heterojunction blend layers, this indicates that the distribution of PbS quantum dots and titania nanocrystals throughout the volume our device's blend layers is relatively even, for all blend layer compositions currently under study.
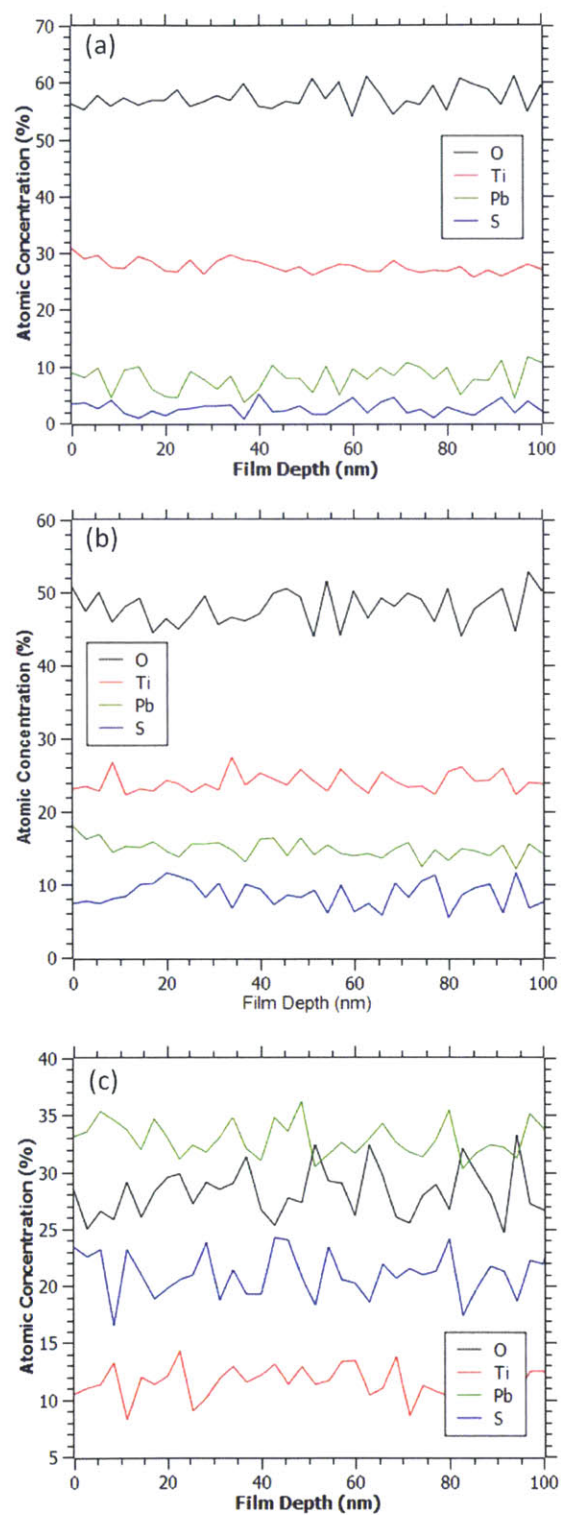
Figure 35. XPS depth profiles of bulk heterojunction blend layers composed of varying ratios of PbS QDs and titania nanocrystals. (a) 25% volume fraction PbS, (b) 50% volume fraction PbS, (c) 75% volume fraction PbS.

This elemental analysis indicates that PbS and titania are extremely well distributed and mixed throughout the volume of the bulk heterojunction, in both the plane of the device and through the depth of the device, at the length scales and resolutions studied. A significant implication of this is that charge carriers generated anywhere within the bulk heterojunction blend are well within a carrier collection length of a heterojunction interface and can, thus, be efficiently separated and extracted. Recall that this collection length is ~250nm and is the sum of the depletion width and minority carrier diffusion length in PbS. Carriers generated at distances greater than this length from a heterojunction interface are not likely to reach the charge separating drive force required to separate them and enable them to be collected as useful current. However, given the resolution of our EDX and XPS analyses, our results indicate that our bulk heterojunction blends are finely nanostructured and that whatever domains or film morphology may have formed, those features are at a length scale well less than the upper carrier collection length limit needed for efficient charge carrier separation and extraction.

Device Performance

The performance of our bulk heterojunction solar cells employing PbS-rich blend layers was notably worse than that of our devices employing TiO_2-rich blend layers. Figure 36 presents J-V curves for individual representative bulk heterojunction devices employing both titania nanocrystal base layers and titania paste base layers. In both cases, devices with TiO_2-rich blend layers (25% volume fraction PbS in the blend layer) outperformed devices with PbS-rich blend layers (75% volume fraction PbS in the blend layer). While the open circuit voltage remained relatively constant between devices with different blend layer compositions, there was a marked

increase in photocurrent for the TiO$_2$-rich devices. Additionally, the fill factor appears qualitatively higher for the same devices, which results in higher overall power conversion efficiencies.

The performance of the devices employing the titania paste base layers was also generally much higher than that employing the unannealed titania nanocrystal base layers, as photocurrents, photovoltages, and fill factors all appear higher for paste base layer devices.
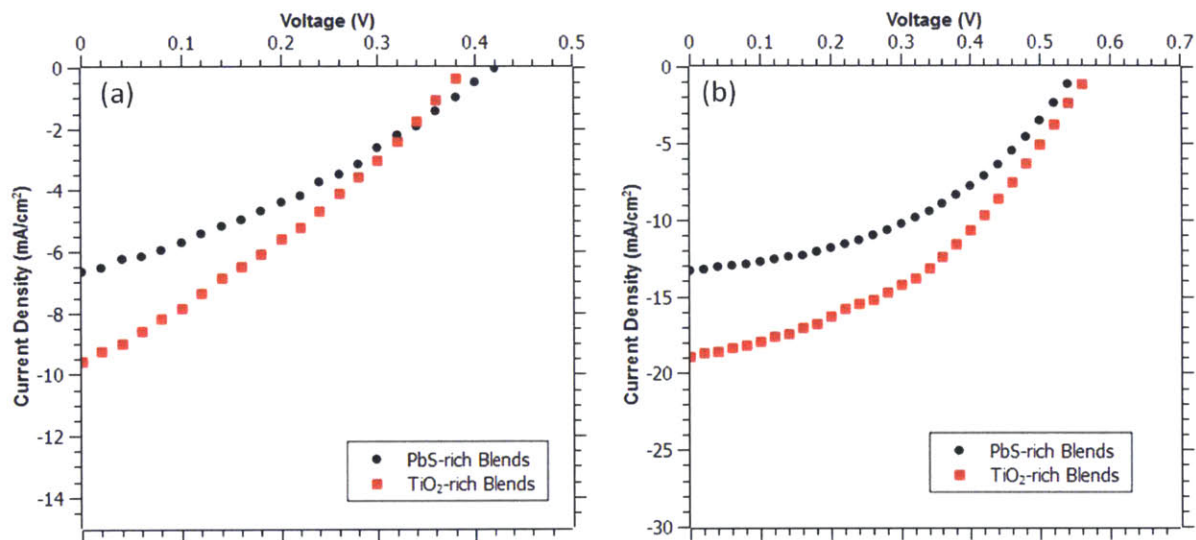
Figure 36. J-V curves for representative bulk heterojunction solar cells comparing devices with Pb-rich blend layers (75% volume fraction PbS) and TiO$_2$-rich blend layers (25% volume fraction PbS) for devices with (a) titania nanocrystal base layers and (b) titania paste base layers.

Origin of Device Performance

Figure 37 presents the averaged overall power conversion efficiency of the bulk heterojunction devices studied here as a function of PbS volume fraction of the blend layer used. For devices

using a nanocrystal base layer, the efficiency is maximized at 1.35% for devices with TiO_2-rich blend layers. It drops significantly to a low of less than 1% for devices with higher amounts of PbS in the blend. Similarly, for devices employing a titania paste base layer, the efficiency is maximized at 4.66% for devices using a TiO_2-rich blend layer. Those using blend layers with more PbS exhibit a drop in efficiency to below 3%.

Figure 37. Averaged power conversion efficiency as a function of PbS volume fraction in the bulk heterojunction blend layer for devices employing (a) a titania nanocrystal base layer or (b) a titania paste base layer.

The averaged photocurrent of these bulk heterojunction devices as a function of blend layer composition follows a similar trend (Figure 38). For devices using a nanocrystal base layer, photocurrent is miaxmized at 9.5mA/cm² for TiO_2-rich blend layers. It steadily drops to a low of 6.44mA/cm² for devices with PbS-rich blends. For devices with paste base layers, the

photocurrent maximizes at nearly 20mA/cm^2 for devices using TiO_2-rich blend layers and is minimized at a low of 13.5mA/cm^2 for PbS-rich devices.
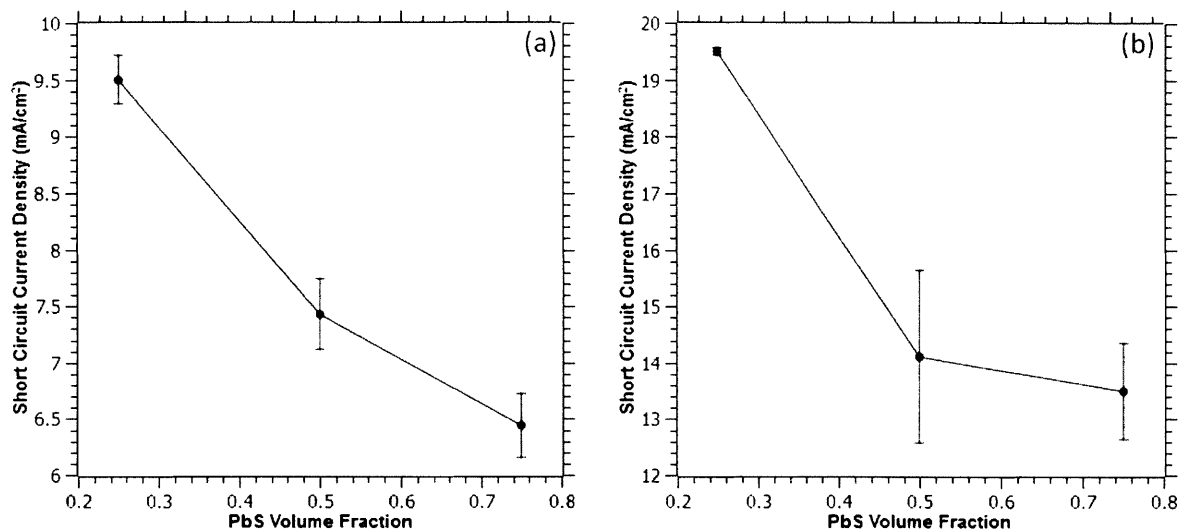
Figure 38. Averaged photocurrent as a function of PbS volume fraction in the bulk heterojunction blend layer for devices employing (a) a titania nanocrystal base layer or (b) a titania paste base layer.

Another major contribution to the differences in device performance is the fill factor. As presented in Figure 39, the averaged fill factor for all devices is maximized for those using TiO_2-rich blend layers. For devices with nanocrystal base layers, this maximum value is 0.315, while that for devices using a paste base layer is 0.386.
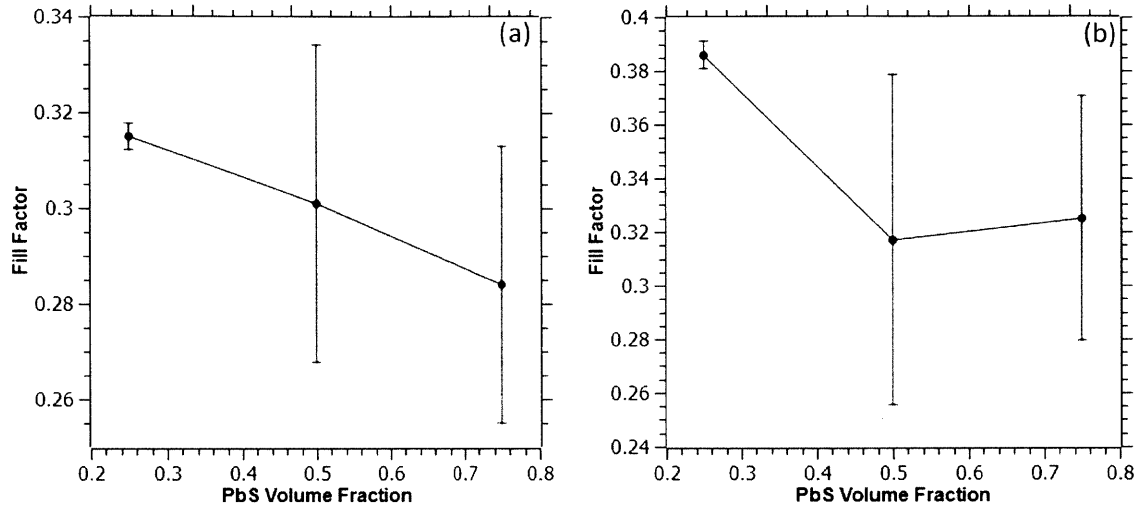
Figure 39. Averaged fill factor as a function of PbS volume fraction fraction in the bulk heterojunction blend layer for devices employing (a) a titania nanocrystal base layer or (b) a titania paste base layer.

The major determinant of the fill factor's decrease with an increase in PbS volume fraction in the bulk heterojunction blend layer is the shunt resistance (presented in Figure 40). For devices with a nanocrystal base layer, it decreases from a maximum of just over $73\Omega cm^2$ for devices with TiO_2-rich blend layers to a low of about $52\Omega cm^2$ for devices using PbS-rich blend layers. Similarly, for devices using a paste base layer, the shunt resistance is maximized at $93\Omega cm^2$ and decreases dramatically at higher PbS blend layer volume fractions.
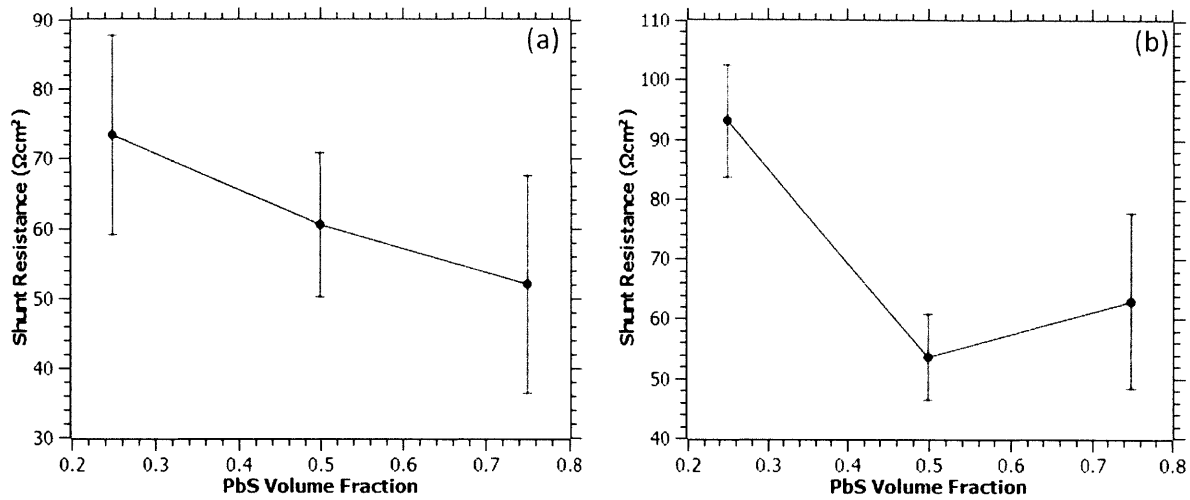
Figure 40. Averaged shunt resistance as a function of PbS volume fraction fraction in the bulk heterojunction blend layer for devices employing (a) a titania nanocrystal base layer or (b) a titania paste base layer.

That the major contribution to the decrease in the fill factor stems from the decrease in shunt resistance is supported by the relatively constant value of the series resistance across all blend layer compositions. As shown in Figure 41, the series resistance doesn't exhibit any well defined trends as a function of blend layer PbS volume fraction and remains comparatively unchanged in absolute value across the various compositions. For devices with nanocrystal base layers, the series resistance of the cells varies between 20 and $35\Omega cm^2$ while for devices employing paste base layers, it varies between only 10 and $15\Omega cm^2$.
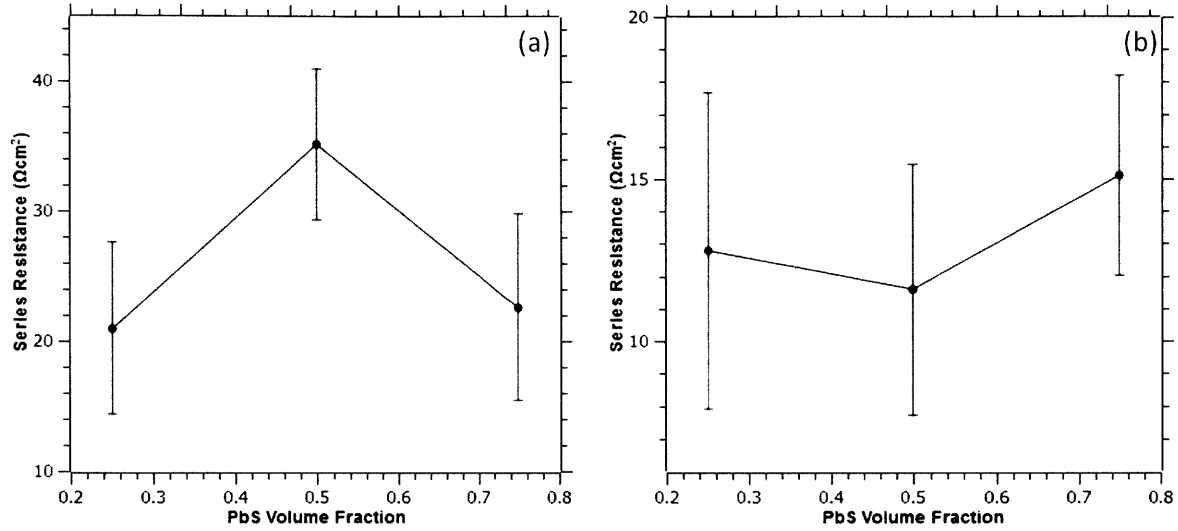
Figure 41. Averaged series resistance as a function of PbS volume fraction fraction in the bulk heterojunction blend layer for devices employing (a) a titania nanocrystal base layer or (b) a titania paste base layer.

Similarly, the open circuit voltage doesn't exhibit any well defined trends either, an expected result. As presented in Figure 42, the V_{oc} for devices employing nanocrystal base layers varies between 0.45 and 0.5V. For devices which used paste base layers, the V_{oc} varied more widely between 0.5 and 0.6V.
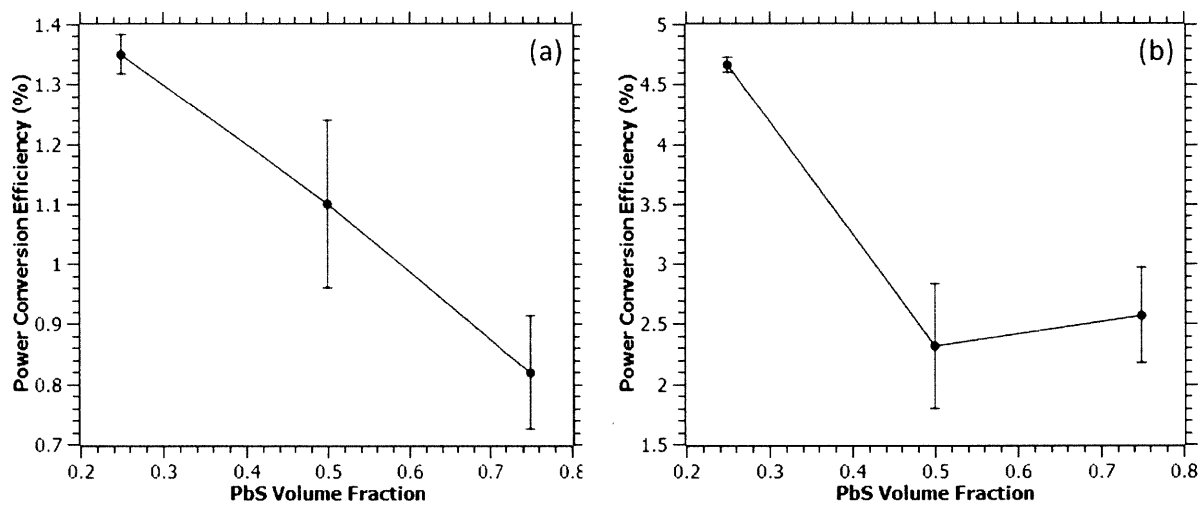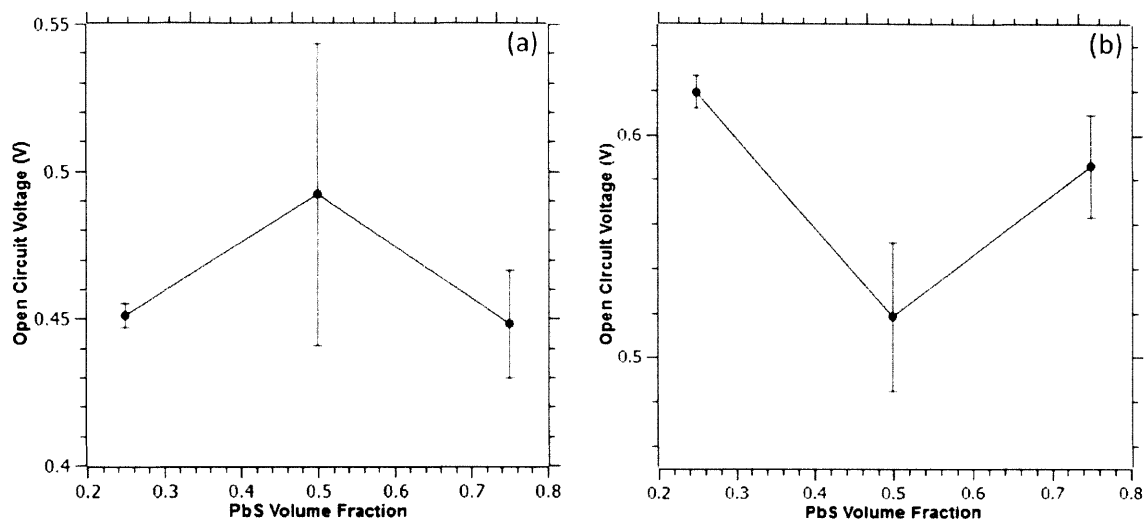
Figure 42. Averaged photovoltage as a function of PbS volume fraction in the bulk heterojunction blend layer for devices employing (a) a titania nanocrystal base layer or (b) a titania paste base layer.

The high performance observed in bulk heterojunction devices using TiO_2-rich blend layers results from the likelihood of forming complete and continuous pathways of each phase through the depth of the blend layer at TiO_2-rich blend layer compositions. To achieve high efficiency, both phases must be simultaneously continuous and the blend layer itself must be essentially bicontinuous. It has been previously predicted that in binary particle mixtures such as the blend layers employed here (i.e., a blend of two components or materials, each of which is composed of particles of a given size), a band of volume fractions exists over which this is the case. Furthermore, this band is dependent on the size mismatch between the particles that constitute each of the two phases that constitute the blend. As the particle size ratio increases (i.e., a greater difference in particle sizes), the region of bicontinuity shifts to lower volume fractions of the smaller particle. For instance, when the particles of the two constituent phases of the blend are the same size, bicontinuity is predicted for volume fractions of either particle between

approximately 0.3 and 0.7, centered, as one would intuitively expect, around an even volumetric split. However, as the size of the particles constituting phase 1 decreases below the size of the particles constituting phase 2, the region of bicontinuity shifts to lower volume fractions of the phase with the smaller particles. Thus, it is predicted that for the blend layers here, in which the particle size mismatch is between 2 and 3, bicontinuity only exists for PbS volume fractions (the smaller particle) of approximately 0.1 to 0.4 [87]. Our highest performing devices were composed of blend layers with PbS volume fractions of 0.25. The effect of particle size mismatch and film composition on the bicontinuity of binary particle mixtures is graphically illustrated in Figure 43.
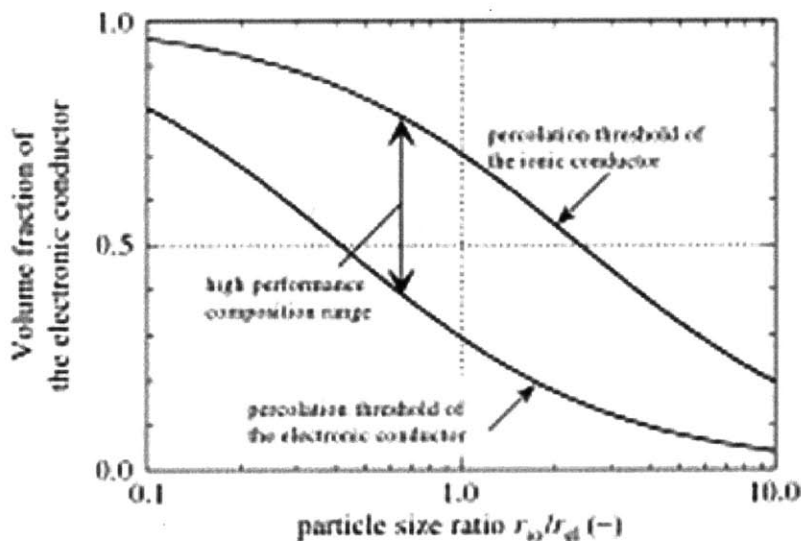
Figure 43. Effect of particle size mismatch on bicontinuity threshold (expressed as film composition) in binary particle mixtures [87].

This makes intuitive sense as well. Because the titania nanocrystals are larger, there are fewer of them for a given volume than there would be of the smaller PbS quantum dots in the same

occupied volume. As a result, there's a lower probability that a continuous pathway can be formed by the titania nanocrystals. Accordingly, to achieve a bicontinuous blend, the volume fraction occupied by the larger particles (titania nanocrystals in this case) must be greater than that occupied by the smaller particles. This ensures that are enough of the larger particles to form a continuous pathway.

When this is the case, a true bulk heterojunction is created. Charge carriers generated with the large volume occupied by the blend layer can be efficiently extracted, since a much greater volume of the device is depleted than is the case for a more traditional bilayer device. The electric field of the depletion region helps separate excited charge carriers and sweep them out to the appropriate electrodes. This manifests itself as a higher observed photocurrent for bulk heterojunction devices with bicontinuous blend layers, consistent with the findings presented in Figure 38, where the J_{sc} was maximized for devices using blend layers with PbS volume fractions of 0.25, the only composition where bicontinuity is predicted.

Additionally, for devices whose blend layers aren't entirely bicontinuous, such as those with PbS volume fractions of 0.5 and 0.75, the blend layers likely contain dead ends and incomplete pathways of titania nanocrystals. Because of this, charge carriers that were once excited and then separated have a high probability of recombining when they encounter a dead end or incomplete pathway before they can be extracted from the device. This would manifest itself as a lower shunt resistance (shunt resistance being an indicator of the probability that charge carriers will recombine or be lost to other mechanisms other than charge extraction), and thus, a lower overall fill factor, consistent with our observations in Figure 39 and Figure 40.

Finally, as was readily observed in all the data, devices with paste base layers consistently outperformed, by a wide margin, those with nanocrystal base layers, regardless of blend layer

composition. The high temperature treatment required to burn off the solvents and organic binders in the titania nanoparticle paste also serve to anneal and sinter the anatase nanoparticles together, providing an easy pathway for charge carriers to traverse. In contrast, the unannealed nanocrystal base layers are composed of separate and discrete titania nanocrystals capped in short chain, relatively insulating organic ligands. It is, thus, comparatively more difficult for charge carriers to continually hop between these separated titania nanocrystals than it is for them to pass through the relatively more connected titania of the annealed paste base layers. As a result, devices using the annealed titania paste base layers will yield higher overall efficiencies. This effect is also readily apparent in the different values for series resistance between devices with the different base layers. As previously presented in Figure 41, the series resistances of devices with annealed paste base layers were consistently lower than series resistances for those with unannealed nanocrystal base layers.

Another way to visualize the relatively enhanced performance of the devices using TiO_2-rich blends over those using the PbS-rich blends is to compare their external quantum efficiency spectra. Figure 44 presents such spectra for devices utilizing both nanocrystal and paste base layers. The EQE for devices that used TiO_2-rich blend layers (those that most likely had bicontinuous pathways through the device, forming a true bulk heterojunction) exhibited enhanced quantum efficiency over a wide range of wavelengths. In particular, for devices that used a nanocrystal base layer, the devices that used TiO_2-rich blend layers exhibited a greater than 50% enhancement in the EQE at the excitonic peak. For devices consisting of the paste base layers, this enhancement was around 44%. This broad enhancement of the quantum efficiency is indicative of the enhanced photocurrent generated by devices with TiO_2-rich blend layers, particularly from red and near-infrared photons absorbed deep in the cell. These photos

are typically lost in traditional bilayer devices since the depletion region doesn't extend deep into the cell far away from the planar interface. However, because of the bulk heterojunction architecture used here, a much greater volume of the device is depleted and, thus, low energy photons absorbed deep in the device can still be used to generate charge carriers that are separated and extracted.
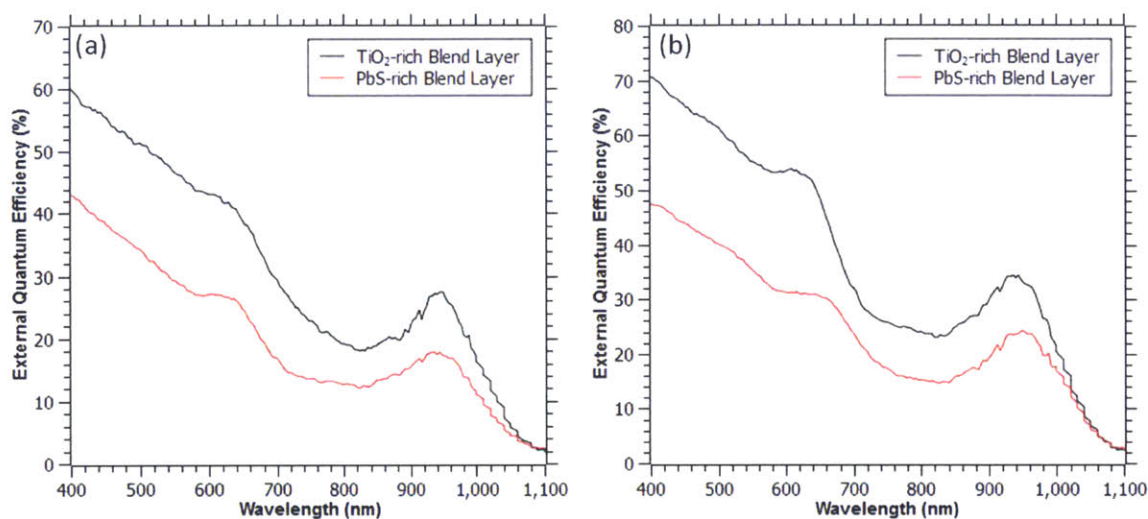
Figure 44. EQE spectra for bulk heterojunction devices employing TiO_2-rich blend layers (25% volume fraction PbS) and PbS-rich blend layers (75% volume fraction PbS) for devices using (a) a titania nanocrystal base layer or (b) a titania paste base layer.

Chapter 4: Effect of Structure on Nanocrystal Bulk Heterojunction Photovoltaics

In this chapter we fabricate, characterize, and test bulk heterojunction solar cells and study the effect that device structure has on performance. Upon closer examination of our bulk heterojunction blends, we find that diffuse interfaces exist between adjacent layers as a result of interfacial surface roughness. Rather than being deleterious, this can have a bulk heterojunction-like effect in which the increased interfacial area extends the spatial extent of the depletion region over a greater volume of our devices. Furthermore, from available evidence and previous work in the literature, we infer that our bulk heterojunction blends form well packed, high density binary particle mixtures, particularly at the TiO_2-rich composition that was previously found to be optimal for device performance. Not only are binary particle mixtures such as ours most likely to form high density films at that particular composition, but it is likely that this peak in packing density helps to enable the formation of the truly complete, bicontinuous pathways needed for the bulk heterojunction to efficiently separate and extract photogenerated charge carriers. We studied the effects of titania nanocrystal size and blend layer thickness on the performance of our bulk heterojunctions. Efficiency was maximized for bulk heterojunctions employing the smallest titania nanocrystals, an indication that at constant volume fractions, larger titania nanocrystals decrease the total number of titania particles available to form complete pathways through the depth of the bulk heterojunction. Furthermore, a peak in device performance was observed at intermediate blend layer thicknesses. This results from the balance between two opposing effects: an increase in light absorption and photocurrent with thicker bulk heterojunctions and an increased likelihood of recombination with thicker bulk heterojunctions. Again, enhanced light absorption and current generation was observed at infrared wavelengths,

validating the ability of bulk heterojunctions to spatially extend the reach of the charge separating driving force, such that the previously missed red and infrared photons may be captured.

Materials and Methods

Titanium tetrachloride and 3-mercaptopropionic acid (>99%) (MPA) were purchased from Sigma-Aldrich and used as received. TEC 15 glass substrates coated in fluorine doped tin oxide (FTO) were purchased from Pilkington Glass. FTO, rather than the more widely used indium doped tin oxide (ITO), was preferred because it does not degrade at the high temperatures required for various steps in the processing of anatase titania. When subjected to these high temperatures (~500°C), the electrical resistance of ITO substrates rises dramatically, beyond the range needed for practical usage in solar cells. Ti-Nanoxide HT/SC (titania nanoparticle paste) was purchased from Solaronix. This paste is a concentrated mixture of anatase titania nanoparticles (15-20nm in size), along with alcohol, water, and various organic binders. In order to be used in solar cells, these binding materials must be burned off in a high temperature bake, which also anneals the titania nanoparticles together.

Lithographically patterned FTO substrates were cleaned sequentially in Micro-90 detergent, water, acetone, and isopropanol, followed by a 2min oxygen plasma treatment. A thin layer of TiO_2 was nucleated on the substrates by baking them in a 120mM $TiCl_4$ solution in water at 80°C for 30min. The substrates were then rinsed off in water and annealed at 500°C for 1 hour in a high temperature furnace. The thin anatase titania layer that results from this treatment helps the subsequently spincast titania or PbS nanocrystals to adhere to the substrate.

For devices employing unannealed anatase titania nanocrystal base layers (to be referred to as "nanocrystal base layers"), a 50mg/mL dispersion of titania nanocrystals in octane was dropped onto the substrate until it was completely covered. The substrate was then spun at 2500rpm for 10s. To exchange the as-synthesized oleate ligands on the nanocrystals with MPA, a 1% v/v MPA solution in methanol was then applied to the substrate and the substrate was then spun at 2500rpm for 10s. The substrate was then rinsed with methanol and spun again at 2500rpm for 10s. These three spincoating steps were repeated until the desired film thickness was reached.

For devices employing the commercial Solaronix titania paste base layers (to be referred to as "paste base layers"), the as-received Solaronix solution was dropped onto the substrate which was spincast for 60s at varying speeds in order to achieve the desired approximate film thickness. The substrate was then baked at 500°C for 1 hour in a high temperature furnace to sinter the particles together and remove the solvents and organic binders present in the paste.

The blend layers were prepared by mixing concentrated octane solutions of titania nanocrystals and PbS QDs to obtain mixtures with a composition of 25% PbS volume fraction (obtained by using the material's density to convert from mg/mL) and then diluting the solution to 50mg/mL for spincoating. The mixed solution was dropped onto substrates, which were then spun at 2500rpm for 10s. MPA ligand exchange was carried out and the substrate was rinsed. These steps were repeated until the desired film thickness was reached.

Finally, the cover layer of pure PbS was deposited by dropping a 50mg/mL solution of PbS QDs onto the substrate and spinning the substrate at 2500rpm for 10s. MPA ligand exchange was carried out and the substrate was rinsed. These steps were repeated until the desired film thickness was reached.

Top electrical contacts composed of 25nm of MoO_x and 100nm of Au were then thermally evaporated onto the devices.

Scanning electron microscopy (SEM), and the accompanying energy dispersive X-ray (EDX) analysis, was performed on a JEOL 6700F field emission scanning electron microscope. Cross sectional SEM imaging was done on a Helios Nanolab 600 Dual Beam Focused Ion Beam Milling System. X-ray photoelectron spectroscopy (XPS) analysis was performed on a PHI Versa-Probe II spectrometer with a scanning monochromated Al source (1,486.6eV; 50W; spot size, 200μm). An argon source was used for sputtering and the zalar rotation was set at 1rpm. Roughness measurements were performed using a Veeco Dimension 3100 atomic force microscope (AFM). Thin film thickness measurements were determined using a Veeco Dektak 150 profilometer. Device performance data was measured using a solar simulator (150W Newport 96000 xenon arc-lamp, with AM1.5G filter and diffuser lens) that was calibrated to $100mA/cm^2$ using a silicon reference cell. An external bias was applied to devices and the photocurrent was measured using a Keithley 6487 picoammeter.

Device Structure

The devices fabricated here utilized both titania nanocrystal base layers and titania paste base layers. Two structural parameters of interest were varied. First, we studied bulk heterojunction devices that used different sizes of the titania nanocrystals synthesized and studied here. We used titania nanocrystals synthesized from procedures that produced particles with average sizes of 6.92nm, 7.67nm, 8.38nm, and 8.97nm. The thickness of the blend layer in these bulk

heterojunction devices was held constant at 100nm. The underlying titania base layer was deposited with a thickness of 150nm, as was the top layer of pure PbS.

Second, bulk heterojunction devices were made in which the thickness of the blend layer was varied between 0 (a bilayer device) and 200nm, while keeping the total thickness of the photoactive layer stack at 400nm. For example, in the bilayer devices, a 200nm layer of titania was deposited, followed by a 200nm layer of PbS QDs, while for bulk heterojunction devices with a 200nm blend layer, a titania base layer of 100nm was used, and the final cover layer of PbS was also only 100nm in thickness. For all devices fabricated in this second investigation, small titania nanocrystals with an average size of 6.92nm were used.

To visualize the general structure of our devices, we imaged thin films made in the same way as our devices. Figure 45 presents cross sectional SEM micrographs of a bilayer heterojunction of PbS QDs deposited atop a titania paste base layer on a silicon substrate (the same substrate used for XPS depth profiling and AFM analysis). While the titania layer exhibits a rough, dark, and granular surface, that of the PbS layer appears significantly less rough, lighter in color shade, and much finer. These observations were confirmed by AFM roughness measurements. PbS QD films on silicon can have RMS roughness values as low as 2-3nm. In large contrast, the roughness of titania paste base layers can have roughness values an order of magnitude larger.
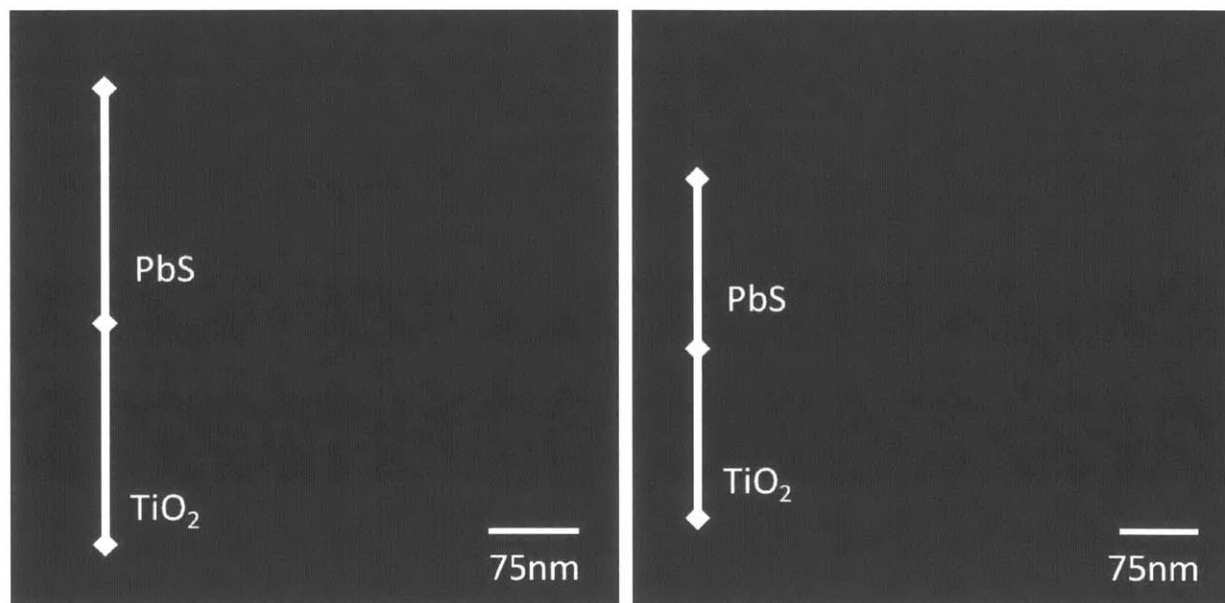
Figure 45. Cross sectional SEM micrograph of PbS QD layer on top of titania paste base layer.

When a blend layer is present, as in Figure 46, its appearance is intermediate between that of the titania and PbS layers. While rougher than the PbS layer, it's less so than the underlying titania base layer. In Figure 46, this blend layer appears as a very lightly colored band between the darker, but smoother, PbS layer above it and the even darker and rougher, more granular titania layer below it. This is an expected result given the presence of both titania and PbS in the blend layer. Again, AFM roughness measurements lend support to these qualitative observations. Roughness measurements on blend layers of PbS dots and titania nanocrystals yielded roughness values between 5 and 10nm, intermediate between those of pure PbS and pure titania nanoparticle paste. It should be noted that these roughness measurements were taken on the exposed surfaces of spin cast thin films of these materials, not the mechanically fractured cross sections seen in the SEM micrographs. Due to the fractured nature of the films seen in the SEM

images, they likely appear significantly rougher as a whole than they would typically be in undisturbed thin films, such as those used in our devices.
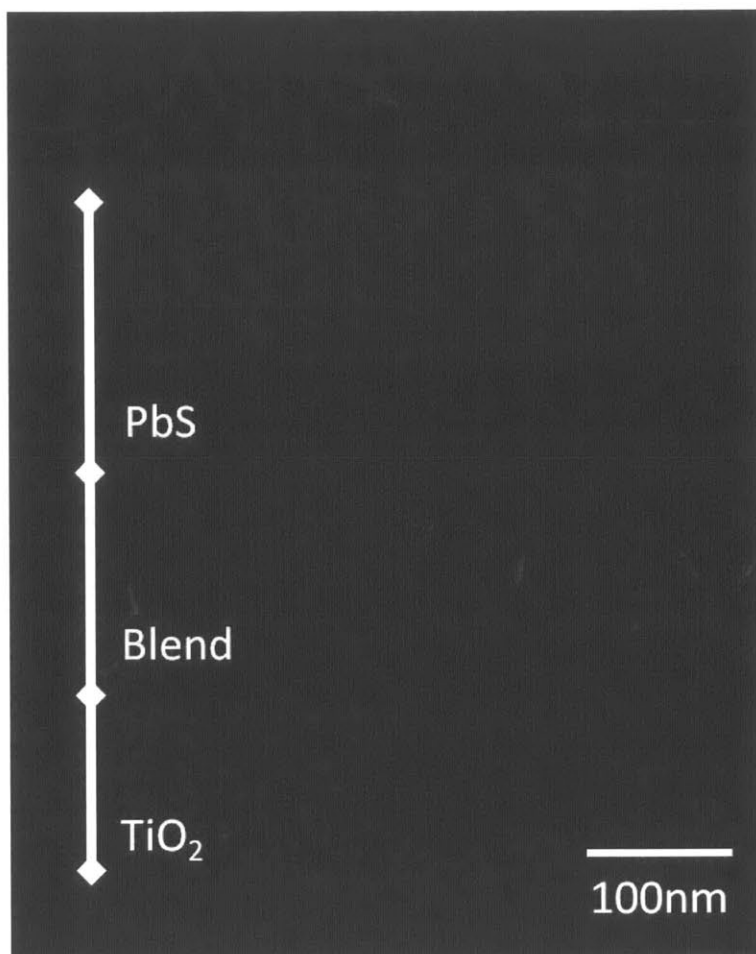
Figure 46. Cross sectional SEM micrograph of PbS QD layer on top of a blend layer of PbS dots and titania nanocrystals, with an underlying base layer of titania nanoparticle paste.

The variance in surface roughness of these different layers is also evident in XPS depth profiles of the interfaces. Figure 47 presents elemental depth profiles of pure PbS QD layers on top of a pure titania nanocrystal base layer and a TiO_2-rich blend layer. Given the extremely low surface

roughness of the blended layers, it is not surprising that the transition between pure PbS and the blend takes place over a much shorter depth window than the transition between pure PbS and a titania paste base layer (as previously presented in Figure 34). Because of the relatively high surface roughness of the titania paste, the transition between the pure PbS layer and the underlying titania base took place over several tens of nanometers, likely indicating a large degree of interpenetrating between the two layers. By contrast, the much smoother blend layer provides comparatively little opportunity for the same degree of intermixing with the overlying PbS that was seen in Figure 34. The interface is much less diffuse.

When PbS is deposited on a pure titania nanocrystal base layer, however, the depth window over which the atomic concentrations change between the adjacent layers is intermediate between that of the titania paste and the blend layers. This likely indicates an intermediate degree of interpenetration between the PbS and titania nanocrystal layers. This is further supported by the surface roughness of the nanocrystal layers. Using AFM measurements, surface roughness values of titania nanocrystal layers on silicon were observed to be greater than 10nm, but consistently lower than those for the titania paste films. This is consistent with our observation that the interface between PbS and the titania nanocrystal layer is of an intermediate degree of diffuseness.
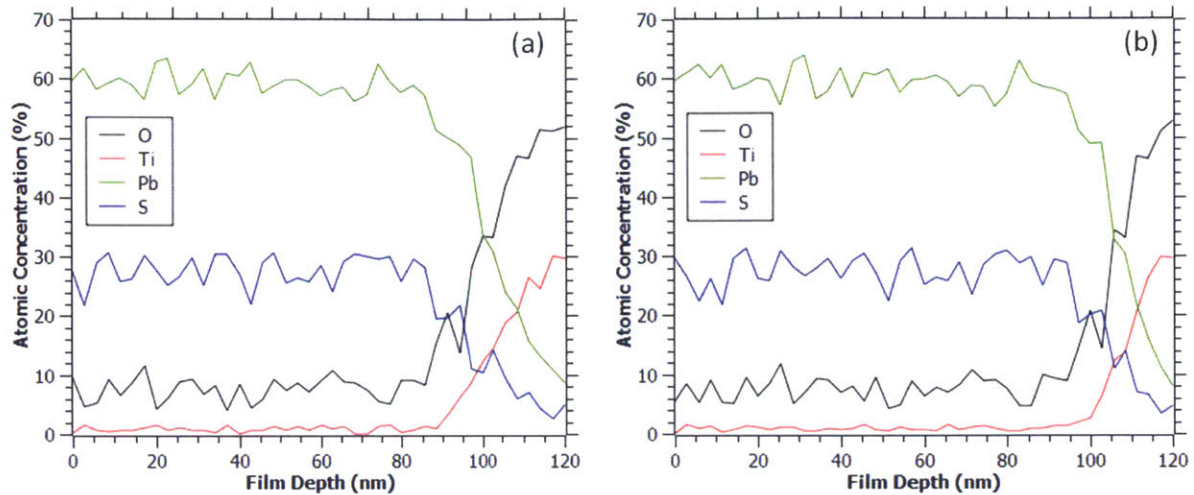
Figure 47. XPS depth profiles of PbS QDs deposited on top of (a) a titania nanocrystal base layer, and (b) a blend layer of PbS dots and titania nanocrystals with 25% PbS volume fraction.

Our roughness measurements can provide additional insight into the structure of the various layers of our devices beyond how much interpenetration there is between the particles of adjacent layers. For instance, it has been observed that an inverse correlation exists between packing density and surface roughness in spincast films of PbSe quantum dots [78]. It's reasonable to assume that a similar effect is at work in our films as well. Layers with lower surface roughness could indicate that the particles are packing more closely and densely with each other (among films composed of the same particles). Furthermore, there's much evidence to suggest that more polydisperse particles tend to have higher packing density [82, 83]. Our own AFM measurements show that our blend layers have slightly lower surface roughness than our pure titania nanocrystal layers. This could indicate that our blend layers are very highly packed, at least relative to the packing density of the pure titania nanocrystal layers. And because our blend layers are mixtures of PbS QDs and titania nanocrystals, they are more

polydisperse than either component by itself. The tendency for such polydisperse particle collections to form solids of high packing density lends further support to the notion that our blend layers are, indeed, high density and well packed.

As previously described, the roughness of our blend layers varied between 5 and 10nm. Intuitively, one would expect films with a greater volume fraction of PbS to exhibit the lowest roughness, given the smaller size of PbS dots compared to that of titania nanocrystals. However, we found that our highest performing blend layer composition, 25% PbS volume fraction, exhibited the lowest surface roughness of our various studied blend layer compositions. Films at this TiO_2-rich composition had surface roughnesses of approximately 6nm, while films with increased PbS volume fractions typically exhibited slightly elevated surface roughness values of approximately 8-10nm. This could be an indication that while the TiO_2-rich blends contained fewer of the small PbS quantum dots, the ratio of large and small particles at that particular composition provided the best mixture for forming very densely packed (and, as a result, very smooth) films.

Previously, Sohn, et al., found that maxima in packing density occur for binary particle mixtures at weight % concentrations of the larger component ranging from 55% to 75%, depending on the particle size ratio of the two components [82], presented in Figure 48. For size ratios similar to that of our present work, the maxima in packing density occur closer to 50-60 weight % of the larger component. Interestingly, in our devices with the highest performing blend layer compositions, that of 25% PbS volume fraction, the weight % composition of the larger component in the blend, the titania, is approximately 55-60%. Thus, while we previously noted that the primary reason behind the peak in device performance at this particular blend layer composition stems from high likelihood of a truly bicontinuous mixture in the bulk

heterojunction blend, it could also be that the blend layer at that particular composition is exceptionally well packed and high density, as predicted by Sohn.
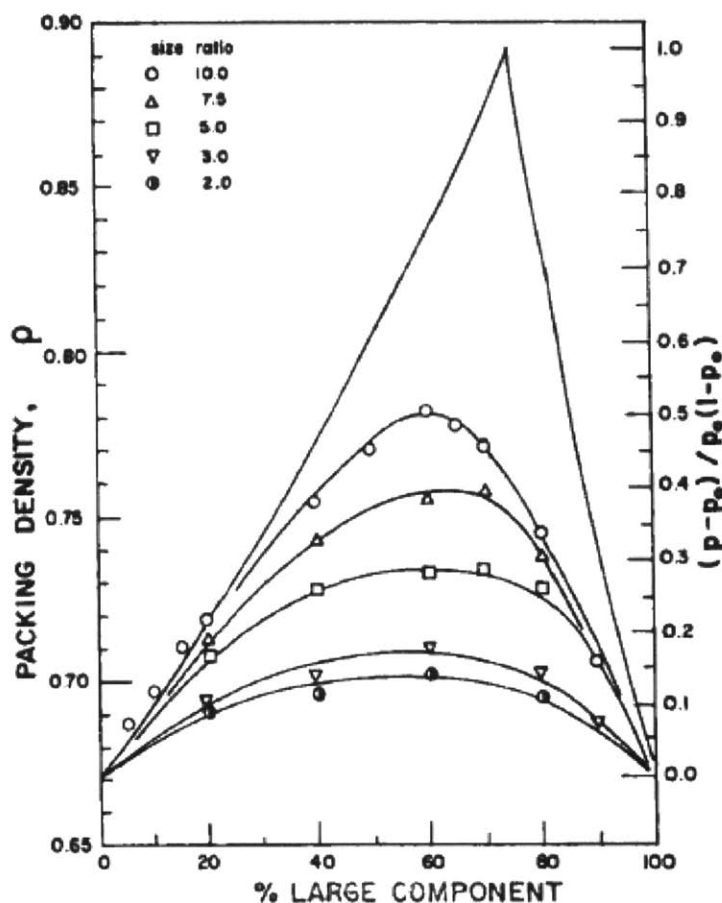
Figure 48. Effect of film composition on film packing density (at various particle size ratios) for binary particle mixtures (of millimeter-scale particles) [82].

Taken together, this evidence likely indicates that at TiO_2-rich film compositions, such as the 25% PbS volume fraction studied here, our binary particle mixtures are packing together exceptionally well and better than blended film mixtures of other compositions, as predicted by previous work in the literature and by our own AFM measurements. That this coincides with the binary mixture film compositions most likely to yield a bicontinuous blend is perhaps not

happenstance. When the particles in a film pack extremely well, this maximizes the likelihood that adjacent particles are in direct contact with each other and minimizes the film volume occupied by void space. As a result of this increase in particle-to-particle contact, there's a higher likelihood that both PbS and titania can form unbroken, continuous pathways through the complete depth of the film, creating the bicontinuous network that's so necessary for high performance bulk heterojunctions.

Effect of TiO$_2$ Nanocrystal Size

For both types of titania base layers, it is evident that smaller titania nanocrystals produce higher performing devices (Figure 49). While the V$_{oc}$ remains similar between devices with large and small titania nanocrystals, devices with small titania nanocrystals exhibit enhanced photocurrent, and as a result, larger fill factors and higher overall power conversion efficiencies. And as before, devices using titania paste base layers significantly outperformed their counterparts composed of unannealed titania nanocrystal base layers.
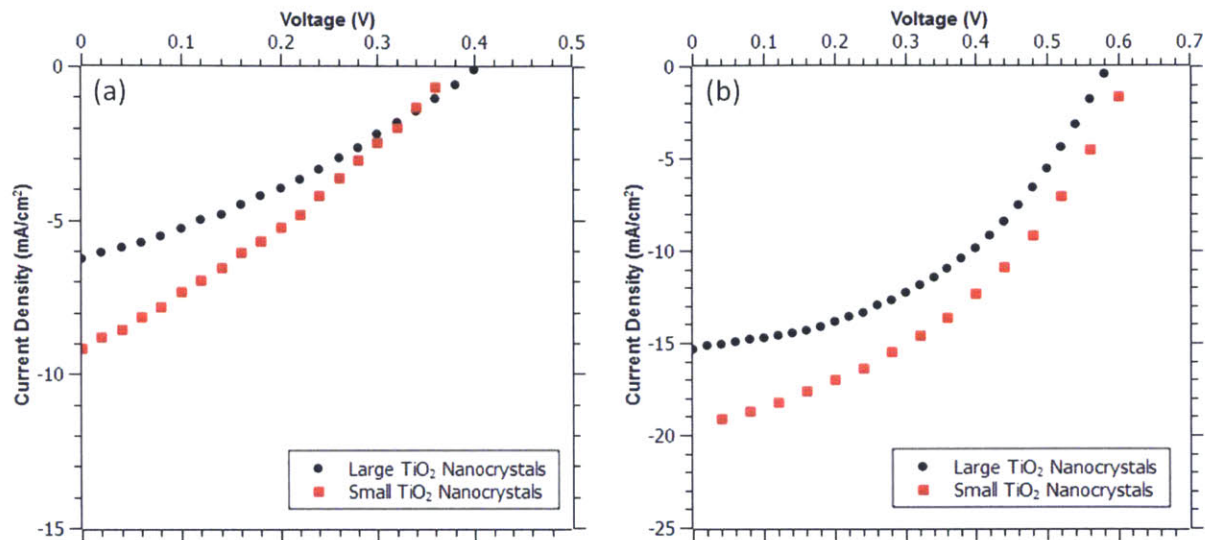
Figure 49. J-V curves for representative bulk heterojunction solar cells comparing devices with large titania nanocrystals and small titania nanocrystals (6.92nm average size) for devices with (a) titania nanocrystal base layers and (b) titania paste base layers.

The averaged device efficiencies peak at the smallest titania nanocrystal sizes (Figure 50). For devices with nanocrystal base layers, efficiency peaks at 1.35% but falls to a low of 0.77% for devices with the largest titania nanocrystals. For devices with paste base layers, the efficiency peaks at 4.66% and drops to a low of 3.22% for larger titania nanocrystal sizes.

Figure 50. Averaged power conversion efficiency as a function of titania nanocrystal size for bulk heterojunction devices employing (a) a titania nanocrystal base layer or (b) a titania paste base layer.

A large contribution to the maxima in device performance is the increase in photocurrent with decreasing titania nanocrystal size (Figure 51). For devices with nanocrystal base layers, the J_{sc} falls from its peak at nearly $10mA/cm^2$ to a low of just under $6.5mA/cm^2$. For devices with paste base layers, photocurrent drops from $19.5mA/cm^2$ to $15.8mA/cm^2$ for devices using the largest titania nanocrystals.

Figure 51. Averaged short circuit current density as a function of titania nanocrystal size for bulk heterojunction devices employing (a) a titania nanocrystal base layer or (b) a titania paste base layer.

Another large contribution to the high efficiencies observed at small titania nanocrystal sizes is the maxima in fill factor observed for devices at the same small particle sizes (Figure 52). For devices with nanocrystal base layers, the fill factor increases from 0.291 to 0.315 as the titania nanocrystals decrease in size. Similarly, the fill factor for devices employing paste base layers increases from 0.347 to 0.386 over the same titania nanocrystal size range.

Figure 52. Averaged fill factor as a function of titania nanocrystal size for bulk heterojunction devices employing (a) a titania nanocrystal base layer or (b) a titania paste base layer.

The primary determiner of the changes observed in device fill factor is the shunt resistance (Figure 53). For nanocrystal base layer devices, it increases from just over $50\Omega cm^2$ to a high of $73.3\Omega cm^2$ for devices using the smallest titania nanocrystals. Similarly, for paste base layer devices, the shunt resistance increases from $57.3\Omega cm^2$ to $93\Omega cm^2$ for the smallest nanocrystal sizes.
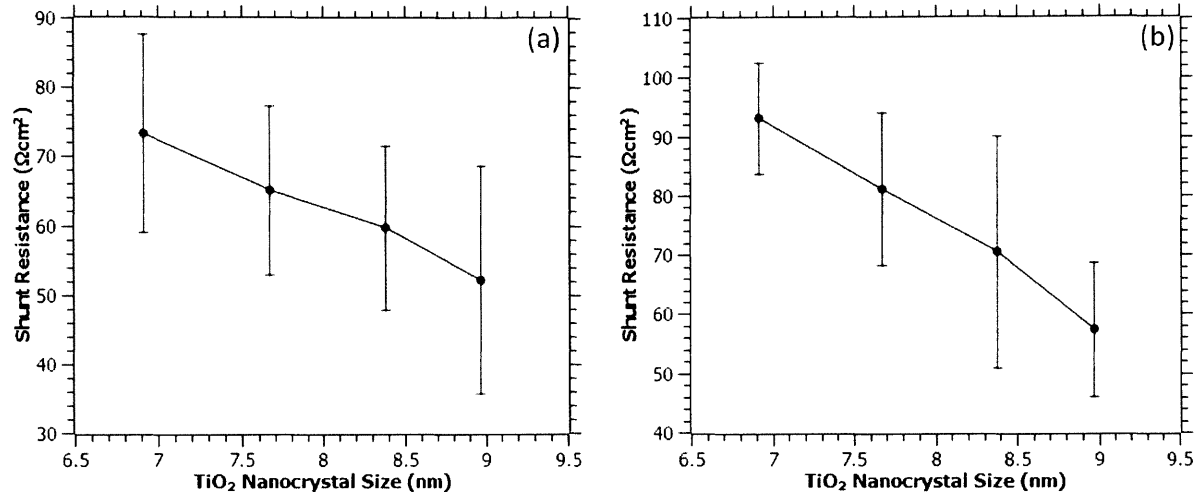
Figure 53. Averaged shunt resistance as a function of titania nanocrystal size for bulk heterojunction devices employing (a) a titania nanocrystal base layer or (b) a titania paste base layer.

In contrast, however, the series resistance doesn't exhibit any well defined trends (Figure 54). For nanocrystal base layer devices, the series resistance varies between 20 and $35\Omega cm^2$, while for paste base layer devices, it remains confined to just $12\text{-}18\Omega cm^2$.
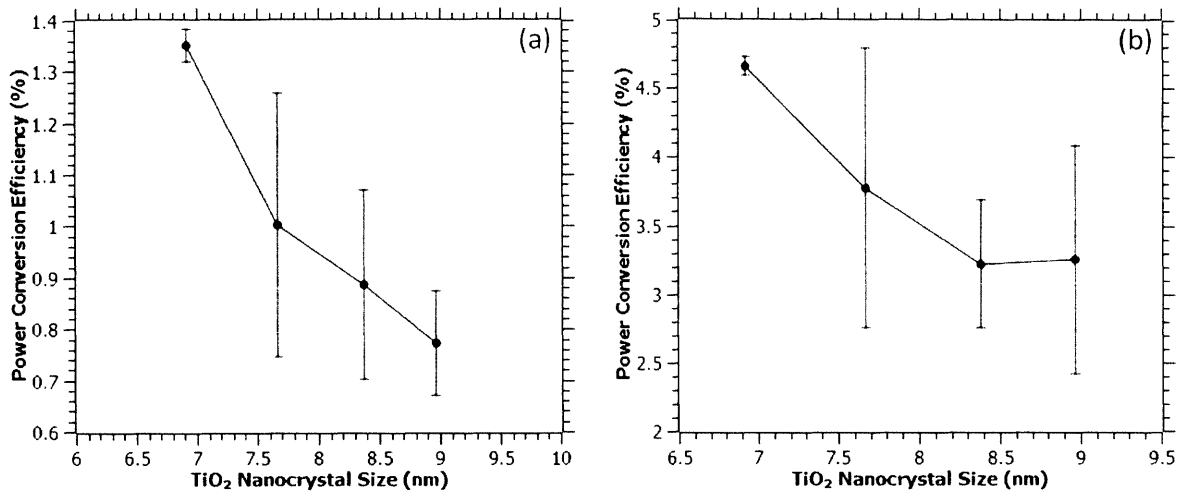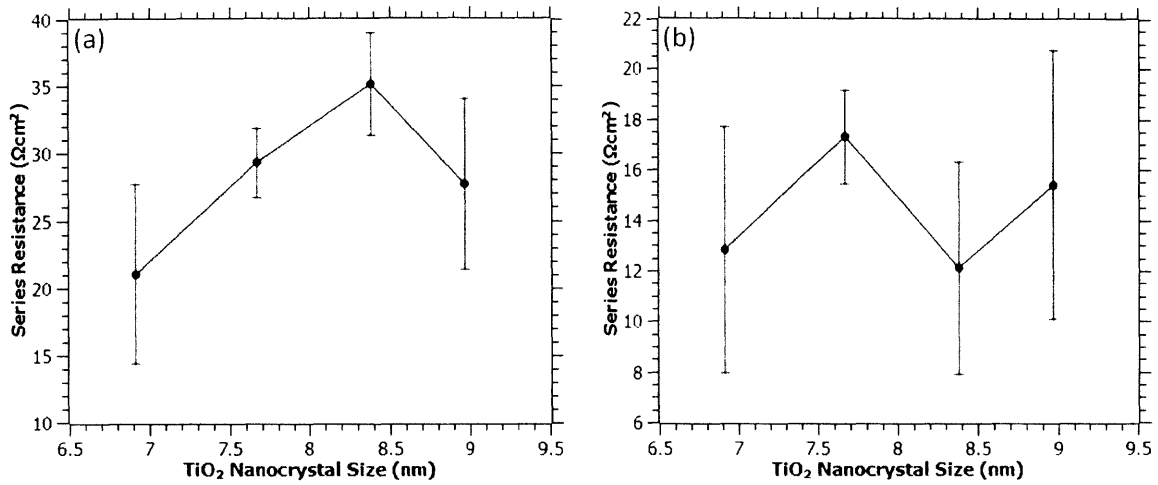
Figure 54. Averaged series resistance as a function of titania nanocrystal size for bulk heterojunction devices employing (a) a titania nanocrystal base layer or (b) a titania paste base layer.

Similarly, the V_{oc} doesn't exhibit any well defined trends over the titania nanocrystal size range studied (Figure 55). For the devices with nanocrystal base layers, the photovoltage varied slightly between 0.41 and 0.45V. For devices with titania paste base layers, the V_{oc} varied more widely between 0.512V and 0.619V.
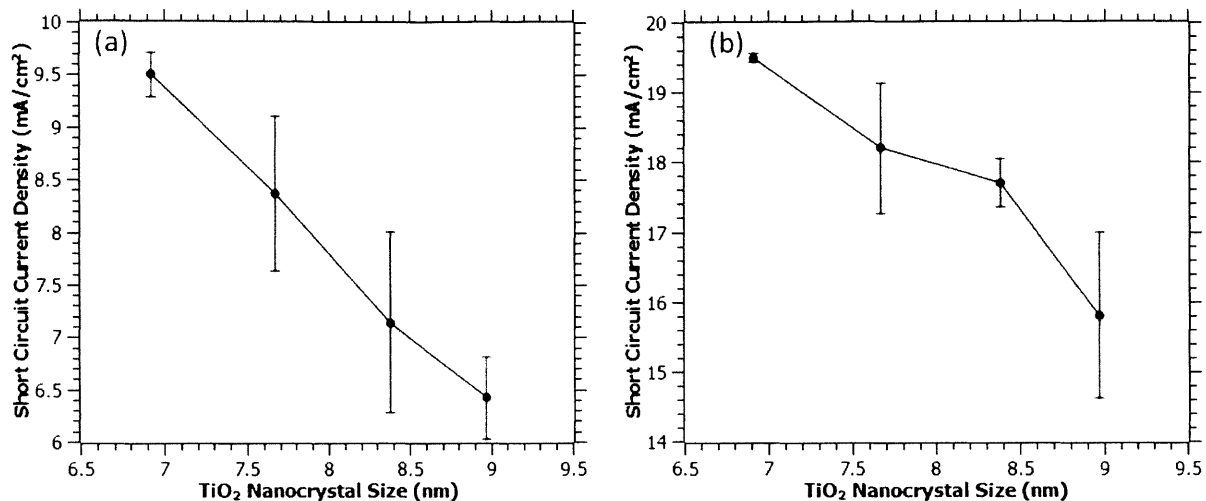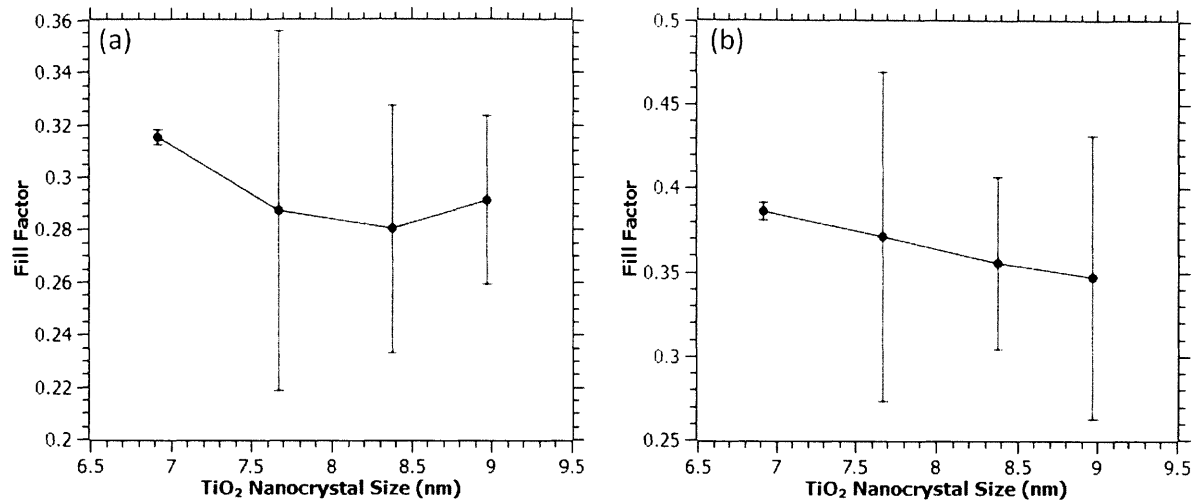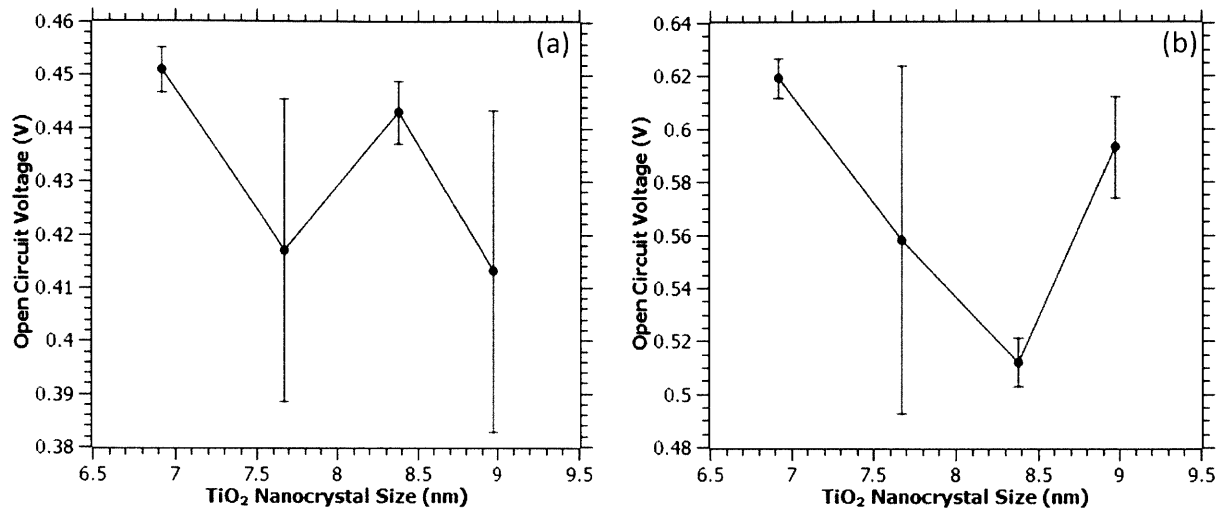
Figure 55. Averaged open circuit voltage as a function of titania nanocrystal size for bulk heterojunction devices employing (a) a titania nanocrystal base layer or (b) a titania paste base layer.

The photocurrent and fill factor were the primary driving forces behind the observed trends in device performance over the range of different titania nanocrystals studied. The shunt resistance, in particular, largely determined the observed variations in fill factor among these solar cells. For a given, set composition in the blend layer of these bulk heterojunctions, as the average size of the titania nanocrystals is increased, the average number of titania nanocrystals in the blends decreases. As a result, for bulk heterojunction blend layers using larger titania nanocrystals, there's a decreased likelihood that there are enough titania particles in the blend to form a completely continuous pathway through the entire depth of the bulk heterojunction. As a result, there are more incomplete and dead end titania pathways. This is apparent from the low shunt resistance and fill factor values observed for devices employing large titania nanocrystals. Charge carriers that had once been excited and separated cannot be efficiently extracted. They become lost to recombination mechanisms when they encounter these discontinuous and

incomplete titania pathways. On the other hand, when the given volume fraction is occupied by smaller titania nanocrystals, there are a greater number of them and, thus, a higher likelihood that they can form continuous transport pathways through the depth of the blend. This enables charge carriers generated anywhere in the large volume of the blend layer to be efficiently separated and extracted. The ultimate manifestation of this is the increase in photocurrent for devices employing smaller titania nanocreystals. As with the effect of blend layer composition on the likelihood of bicontinuity in the film, the effect of particle size (and, thus, particle size mismatch) on film bicontinuity can also be visualized in Figure 43.

As before, devices using titania paste base layers, as a whole, perform better than their counterparts using titania nanocrystal base layers. The high temperature treatment required to burn off the solvents and organic binders in the titania nanoparticle paste also serve to anneal and sinter the anatase nanoparticles together, providing an easy pathway for charge carriers to traverse. In contrast, the unannealed nanocrystal base layers are composed of separate and discrete titania nanocrystals capped in short chain, relatively insulating organic ligands. It is, thus, comparatively more difficult for charge carriers to continually hop between these separated titania nanocrystals than it is for them to pass through the relatively more connected titania of the annealed paste base layers. As a result, devices using the annealed titania paste base layers will perform better. This particular effect is most evident in the higher series resistance exhibited by devices with nanocrystal base layers (Figure 54).

Effect of Blend Layer Thickness

For both types of titania base layers, Figure 56 indicates that a bulk heterojunction structure can outperform its traditional bilayer counterpart. Photovoltages remain relatively unchanged between the two device structures, while photocurrent exhibits a dramatic increase for the BHJ. The corresponding increase in fill factor as well leads to higher overall device efficiencies for those adopting a bulk heterojunction architecture.

And as before, devices with titania paste base layers significantly outperformed those with titania nanocrystal base layers.
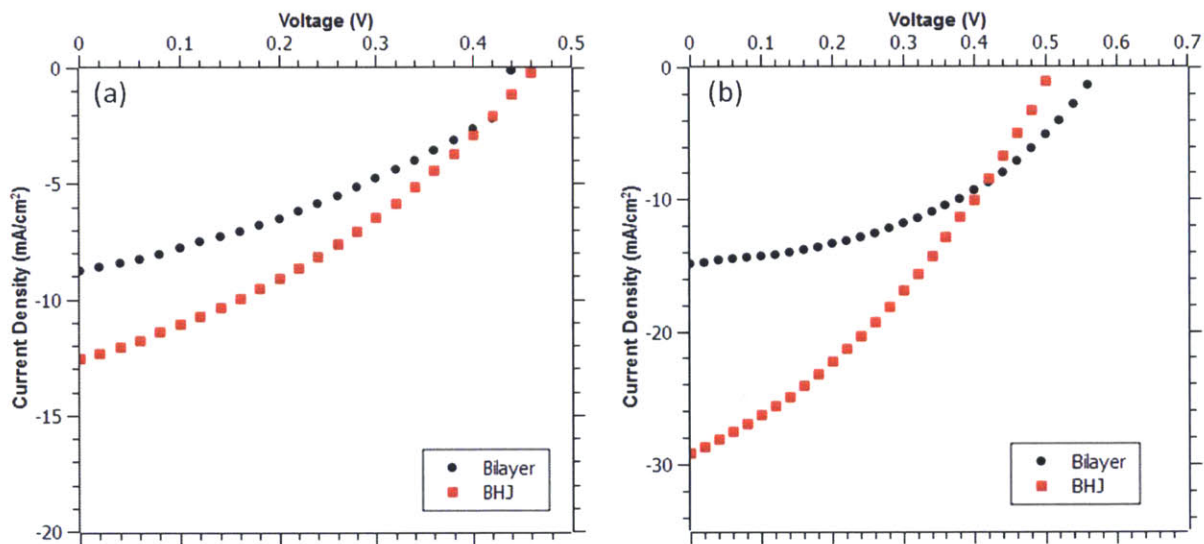
Figure 56. J-V curves for representative bulk heterojunction solar cells comparing devices with a bilayer architecture vs. a bulk heterojunction architecture for devices with (a) titania nanocrystal base layers and (b) titania paste base layers.

The averaged efficiency of devices exhibits a peak with blend layer thickness (Figure 57). For devices using a nanocrystal base layer, the efficiency peaks at 1.47% at a 150nm blend layer.

For devices using the titania paste base layer, the peak efficiency of 4.66% is observed at an intermediate blend layer thickness of 100nm.

Figure 57. Averaged power conversion efficiency as a function of blend layer thickness for bulk heterojunction devices employing (a) a titania nanocrystal base layer or (b) a titania paste base layer.

With an increase in blend layer thickness, the observed photocurrent steadily increases for devices fabricated with either titania base layer type (Figure 58). For those with nanocrystal base layers, the J_{sc} steadily increases from 6.84mA/cm^2 for a bilayer device to 13.4mA/cm^2 for bulk heterojunctions with a 200nm blend layer. For devices using the paste base layers, the photocurrent increases from 13mA/cm^2 for a bilayer structure to a maximum averaged value of 24.2mA/cm^2 for devices with the thickest blend layers.

Figure 58. Averaged short circuit current density as a function of blend layer thickness for bulk heterojunction devices employing (a) a titania nanocrystal base layer or (b) a titania paste base layer.

Unlike the short circuit current density, the fill factor exhibits a steady decline in value with an increase in blend layer thickness (Figure 59). For devices with nanocrystal base layers, the fill factor plummets from 0.35 to 0.221, while for paste base layer devices, the fill factor drops with increasing blend layer thickness from a high of 0.427 to a low 0.319.

Figure 59. Averaged fill factor as a function of blend layer thickness for bulk heterojunction devices employing (a) a titania nanocrystal base layer or (b) a titania paste base layer.

Similar to the way in the fill factor drops with increasing blend layer thickness, so too does the averaged shunt resistance (Figure 60). For nanocrystal base layer devices, it falls from a high of $117\Omega cm^2$ for bilayer architectures to a low of $26.2\Omega cm^2$ for devices with 200nm thick blend layers. Similarly, for devices with paste base layers, the shunt resistance drops rapidly from a high of $155\Omega cm^2$ to a low of $27\Omega cm^2$ over the same thickness range.
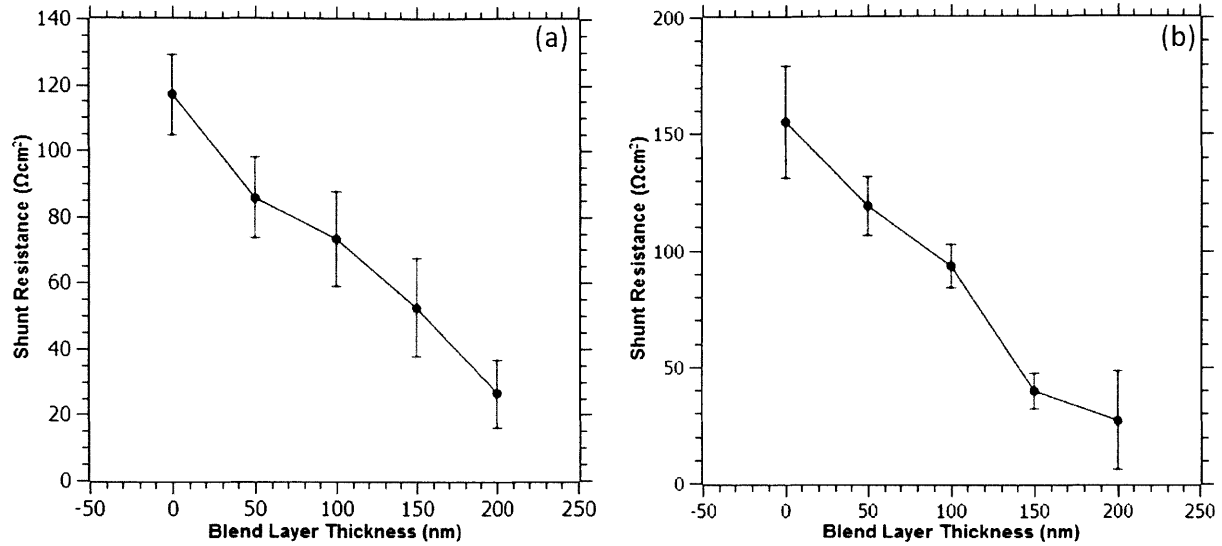
Figure 60. Averaged shunt resistance as a function of blend layer thickness for bulk heterojunction devices employing (a) a titania nanocrystal base layer or (b) a titania paste base layer.

Figure 61 presents the averaged series resistance of these bulk heterojunction devices as a function of blend layer thickness. Unlike photocurrent and fill factor, the series resistance doesn't exhibit a strong trend over the studied thickness range. For devices with nanocrystal base layers, the series resistance varies between 20 and $40\Omega cm^2$, while for devices that utilized titania paste base layers, the series resistance narrowly varies between only 8 and $16\Omega cm^2$.
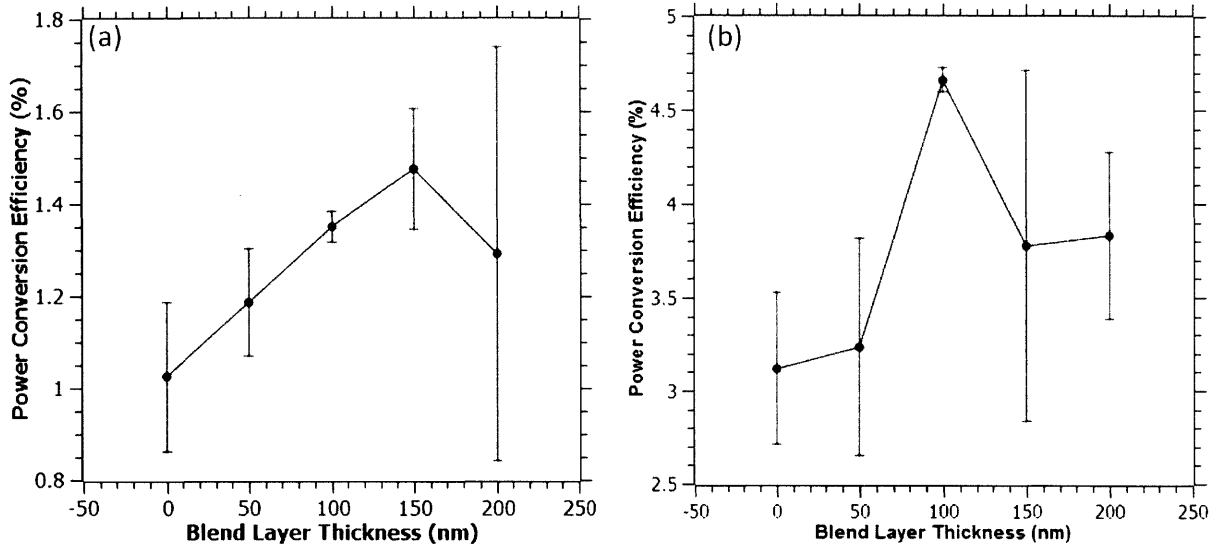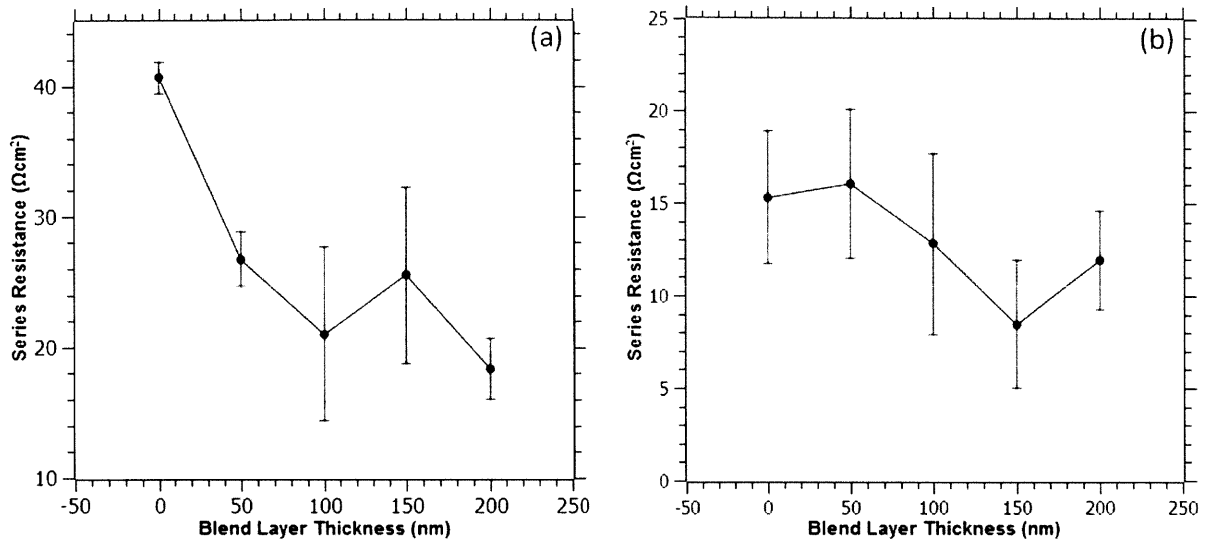
Figure 61. Averaged series resistance as a function of blend layer thickness for bulk heterojunction devices employing (a) a titania nanocrystal base layer or (b) a titania paste base layer.

Similarly, the V_{oc} does not exhibit a cohesive trend. As presented in Figure 62, the photovoltage of devices with nanocrystal base layers varies between 0.428 and 0.480 while that of devices with titania paste base layers varies between 0.488 and 0.619.
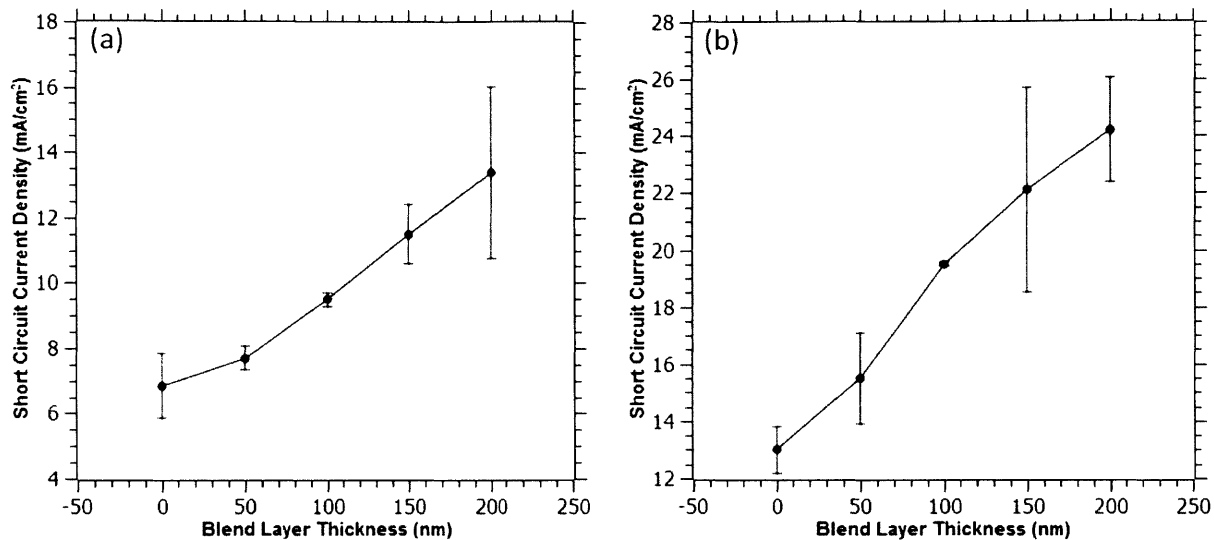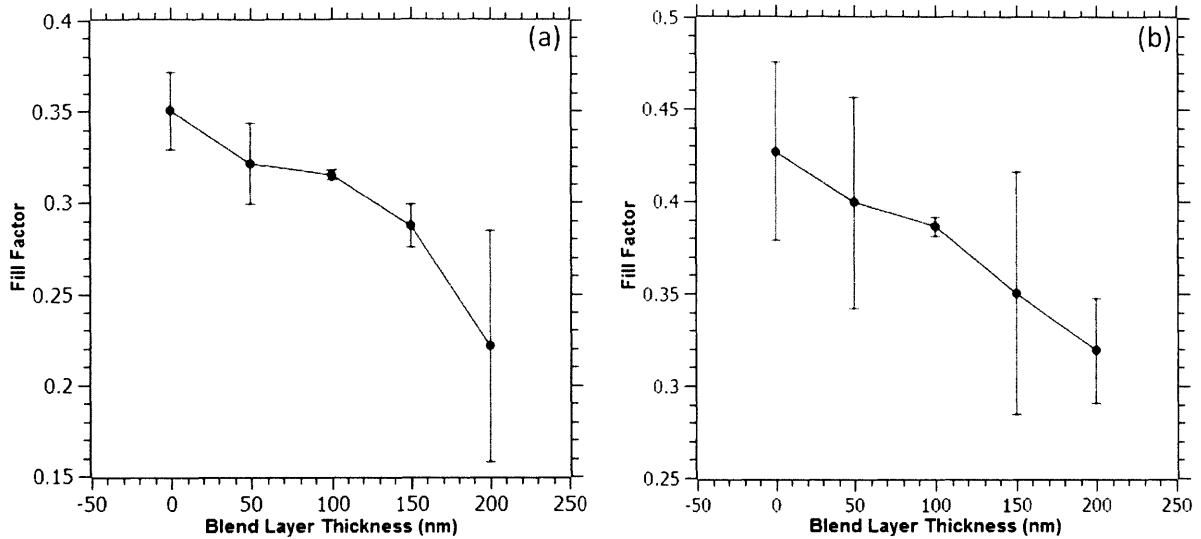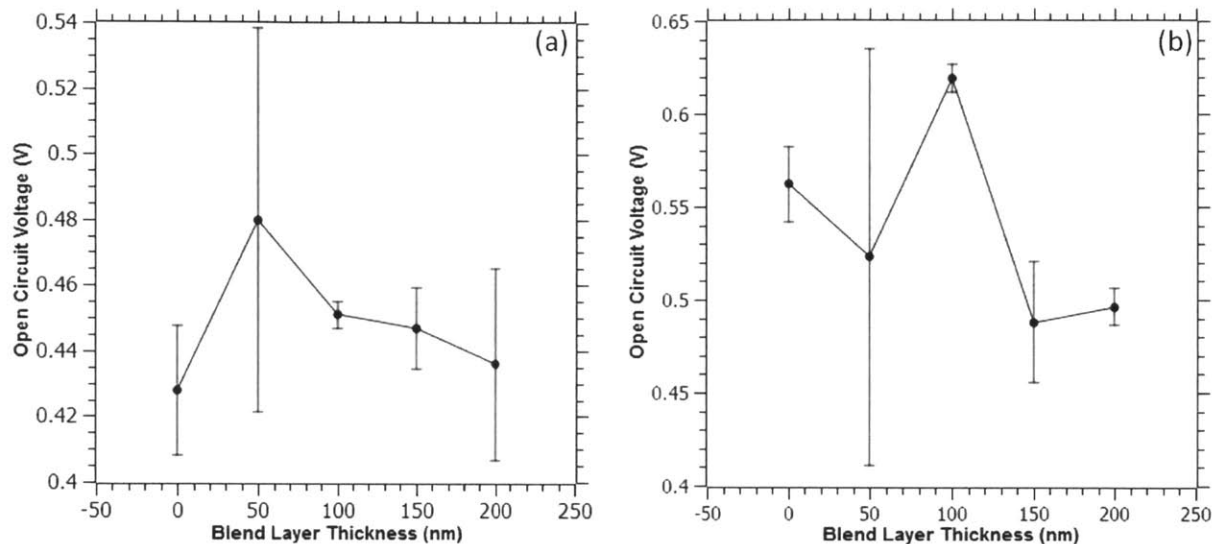
Figure 62. Averaged open circuit voltage as a function of blend layer thickness for bulk heterojunction devices employing (a) a titania nanocrystal base layer or (b) a titania paste base layer.

The peak in efficiency at intermediate blend layer thicknesses for the solar cells studied here results from the balance between two competing effects of the bulk heterojunction architecture. On the one hand, thicker blend layers allow a larger volume of the device to be depleted, i.e., they allow the electric field localized at the heterojunction to permeate a greater volume of the device than would otherwise be possible in a traditional bilayer heterojunction. The presence of this driving force over a greater portion of the device allows charge carriers generated nearly anywhere in the cell to be efficiently separated and extracted, leading to very high photocurrents. However, as the blend layer increases in thickness, so too does the interfacial area between the PbS and TiO_2 components of the blend. While all of this interfacial area is beneficial in enabling charge carriers to be separated, it also presents many opportunities for electrons and holes to recombine. And the often tortuous and random pathways charge carriers must take to travel

through the randomly ordered bulk heterojunction blend can have very large pathlengths. When charge carriers must stay in the cell for longer periods of time before being extracted, there is an increasing chance that those carriers will be lost to bimolecular recombination, given the extremely high interfacial area between the two components of the blend layer. Because of these competing effects, that of increased light absorption / current generation and that of increased recombination, a peak in overall device efficiency exists at an intermediate blend layer thickness, indicating the existence of an "optimal" bulk heterojunction design.

As before, devices using titania paste base layers, as a whole, perform better than their counterparts using titania nanocrystal base layers. The high temperature treatment required to burn off the solvents and organic binders in the titania nanoparticle paste also serve to anneal and sinter the anatase nanoparticles together, providing an easy pathway for charge carriers to traverse. In contrast, the unannealed nanocrystal base layers are composed of separate and discrete titania nanocrystals capped in short chain, relatively insulating organic ligands. It is, thus, comparatively more difficult for charge carriers to continually hop between these separated titania nanocrystals than it is for them to pass through the relatively more connected titania of the annealed paste base layers. As a result, devices using the annealed titania paste base layers will perform better. This particular effect is most evident in the higher series resistance exhibited by devices with nanocrystal base layers (Figure 61).

Another way to visualize the relatively enhanced performance of the bulk heterojunctions over their bilayer counterparts is to compare their external quantum efficiency spectra. Figure 63 presents such spectra for devices utilizing both nanocrystal and paste base layers. The EQE for bulk heterojunctions exhibited enhanced quantum efficiency over a wide range of wavelengths. In particular, for devices that used a nanocrystal base layer, the bulk heterojunction exhibited an

approximately 80% enhancement in the EQE at the excitonic peak. For devices consisting of the paste base layers, this enhancement was approximately 70%. This broad enhancement of the quantum efficiency is indicative of the enhanced photocurrent generated by devices employing a bulk heterojunction architecture, particularly from red and near-infrared photons absorbed deep in the cell. These photos are typically lost in traditional bilayer devices since the depletion region doesn't extend deep into the cell far away from the planar interface. However, because of the bulk heterojunction architecture used here, a much greater volume of the device is depleted and, thus, low energy photons absorbed deep in the device can still be used to generate charge carriers that are separated and extracted.
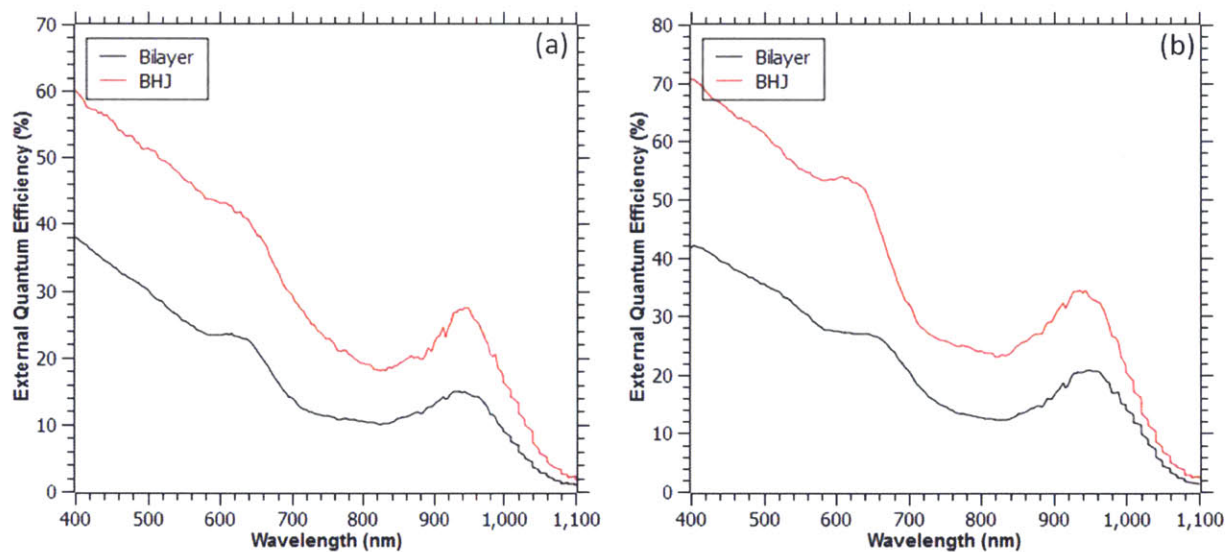
Figure 63. EQE spectra comparing bilayer and bulk heterojunction device architectures for devices using (a) a titania nanocrystal base layer or (b) a titania paste base layer.

Chapter 5: Conclusions and Outlook

In this work, we fabricated and studied bulk heterojunction solar cells composed of PbS quantum dots and anatase TiO_2. In particular, we studied the effect of bulk heterojunction blend composition and device structure on the resulting device performance. In contrast to previous work in this area, our approach enables us to form a bulk heterojunction in a single processing step, eliminating the need for a second step to infiltrate QDs into a previously fabricated or deposited host structure. Additionally, by mixing our p-type and n-type materials in the solution phase and casting the solid bulk heterojunction blend in a single step, we avoid the possibility that incomplete infiltration will result in the creation of deleterious voids and gaps throughout the photoactive layer of the device. Moreover, by fabricating bulk heterojunctions composed of binary nanocrystal mixtures, we were able to create nanostructured and finely mixed blends, ensuring that charge carriers generated anywhere in the bulk heterojunctino were well within a carrier collection length from the heterojunction interface.

Of the bulk heterojunction compositions we studied, optimal device performance was found for devices which employed a TiO_2-rich blend composition. This is a result of the size mismatch between the PbS quantum dots and the larger titania nanocrystals. The likelihood of forming a truly bicontinuous bulk heterojuction peaks at TiO_2-rich compositions, not at an even volume fraction split as would be the case for binary particle mixtures with equal sized constituents. We also found that device performance was maximized for bulk heterojunctions employing the smallest available titania nanocrystals, a consequence of the fact that for a given volume fraction, larger titania nanocrystals decrease the total number of titania particles available to form completely continuous pathways through the bulk heterojunction. Device performance was also maximized for blend layers of intermediate thicknesses. With thicker blends, our devices are

able to absorb more light and generate more current. However, when the blend layers become too thick, charge carrier recombination dominates and outweighs the benefits of enhanced photocurrent. As a result, performance peaks when a balance is struck between these two competing effects.

And finally, we observed enhanced light absorption and current generation at a broad range of wavelengths up to and including red and infrared. This is further validation that a bulk heterojunction device structure spatially extends the reach of the depletion region, such that some of the red and infrared photons not previously captured by the device can now be converted to useful current.

While the ultimate results of this work are satisfying, it is far from complete. As with other areas of photovoltaic research (and probably scientific and technological research in general), researchers are independently pursuing a variety of different routes as a means of further elevating the performance of quantum dot based solar cells, with little agreement or consensus on which routes are the most promising. Some researchers remain focused on engineering the quantum dots themselves. They are investigating new ways to improve them through things like better passivation. Other researchers, such as me, investigate how novel device structures and architectures may be used to further enhance the ability of the device to separate and collect photogenerated charge carriers. And still others are focused other kinds of materials engineering, in particular, the engineering of other parts of the device besides the quantum dots. This includes the engineering of the electrodes, the n-type electron acceptor, and any interfacial layers that may be added. It's reasonable to expect that as this particular field of photovoltaic research matures (it's an extremely young field of solar cell research, with the first PbS quantum dot based solar cells appearing approximately only a decade ago), some of these disparate

advances and approaches may become integrated. For instance, bulk heterojunction researchers may also seek to dope or otherwise engineer the energy band offsets of their n-type materials or implement the newest and greatest passivation strategies in their own quantum dots. Much of this, of course, has to do with a particular researcher's or research group's expertise and field of study. Some naturally have more depth in materials science and may gravitate toward approaches that engineer the surface of the quantum dots, while electrical engineers may be more inclined to study new device architectures and the accompanying device physics. As a consequence, close collaboration between research groups entrenched in these disparate approaches could serve to accelerate the development of these solar cells as a whole.

As exciting of a field as quantum dot solar cells were a few years ago, another field has emerged with even more shocking speed and excitement: perovskite sensitized solar cells [88-91]. In only a few years, the power conversion efficiencies of these devices have skyrocketed from only a few % in 2009 to nearly 20% today. An equally telling measure of how much fanfare exists around this type of solar cell is the three separate pieces that Nature Publishing Group journals (*Nature Materials* and *Nature Photonics*) published in a three month time span last year, all written by some of the world's foremost researchers of emerging solar cells: Michael Gratzel, Michael McGehee, Henry Snaith, and Martin Green. Despite the rapid rise in the performance of these devices, a great deal still remains lacking in terms of the fundamental understanding of the underlying operating mechanisms, an understanding which will be necessary if these solar cells are ever to be successfully commercialized.

What are research groups to do? Should they abandon their current research trajectories and jump on the perovskite bandwagon as well? While the answer may be a matter of opinion, and considerable heated debate, I have several thoughts. First, by jumping from hot topic to new hot

topic, researchers risk never developing deep expertise in any given field of study or technology development. That would seem to be a necessary requirement for the discovery of true, lasting breakthroughs that have long term impact on a technology's real world development and deployment, rather than just superficial headlines and ephemeral attention. Second, in the race to achieve ever higher efficiencies, it might be tempting for some researchers to adopt a trial-and-error method of investigation to find whatever works and yields the highest efficiencies. While higher efficiencies are certainly important for the development and widespread adoption of a particular photovoltaic technology, the basic science should not be skipped either. The process to discover the underlying mechanisms of how and why these materials and devices behave the way they do benefits not only the immediate development of those particular technologies, but also, these fundamental scientific discoveries could have significant spillover benefits into adjoining fields of study and areas of technology development. When viewed as a financial investment, funding of basic scientific research is outrageously profitable [92], with beneficial gains accruing significantly over time and spilling over into other, often unpredictable fields of work. Accordingly, let us not forget that the race to the highest efficiencies may not actually be the course that provides the most social good over the long term. And finally, while power conversion efficiency is certainly a helpful figure of merit for comparing the performance of various solar cells, an even more critical measure of a solar cell technology's promise is $ / watt. Thus, while complex new light absorbers and intricate new device structures may yield sky high power conversion efficiencies, ultimately, the success or failure of these devices can be reduced down to cost. Academic solar cell researchers should remain cognizant that while certain approaches to solar cell development may be academically interesting or may temporarily yield a record setting efficiency, to develop a truly high impact photovoltaic technology, materials cost

and processing cost must be much more of an ever present consideration when selecting which materials and technologies to focus on.

References

[1]   A. Grubler, *Technology and Global Change*: Cambridge University Press, 1998.

[2]   "BP Statistical Review of World Energy," British Petroleum2014.

[3]   *World Population Prospects: The 2012 Revision*. Available:
        http://esa.un.org/unpd/wpp/index.htm

[4]   *The Energy Industry in the United States*. Available: http://selectusa.commerce.gov/industry-
        snapshots/energy-industry-united-states

[5]   *Spot prices for crude oil and petroleum products*. Available:
        http://www.eia.gov/dnav/pet/pet_pri_spt_s1_d.htm

[6]   S. Gorman, "Electricity Grid in US Penetrated by Spies," in *Wall Street Journal*, ed, 2009.

[7]   A. Thompson. (2014, *CO2 Levels above 400 PPM Threshold for Third Month in a Row*.
        Available: http://www.scientificamerican.com/article/co2-levels-above-400-ppm-threshold-for-
        third-month-in-a-row/

[8]   J. Schmidhuber and F. Tubiello, "Global food security under cliamte change," *Proceedings of the
        National Academy of Sciences of the United States of America*, vol. 104, pp. 19703-19708, 2007.

[9]   A. J. McMichael, *et al.*, "Climate change and human health: present and future risks," *The Lancet*,
        vol. 367, pp. 859-869, 2006.

[10]   "Synthesis Report. Contribution of Working Groups I, II, and III to the Fourth Assessment
        Report of the Intergovernmental Panel on Climate Change," 2007.

[11]   S. Pacala and R. Socolow, "Stabilization Wedges: Solaving the Climate Problem for the Next 50
        Years with Current Technologies," *Science*, vol. 305, pp. 968-972, 2004.

[12]   *Electricity Data Browser*. Available: http://www.eia.gov/electricity/data/browser/

[13]   *Table 1-11: Number of U.S. Aircraft, Vehicles, Vessels, and Other Conveyances.* . Available:
        http://www.rita.dot.gov/bts/sites/rita.dot.gov.bts/files/publications/national_transportation_statisti
        cs/html/table_01_11.html

[14]   *How many alternative fuel and hybrid vehicles are there in the U.S.?* . Available:
        http://www.eia.gov/tools/faqs/faq.cfm?id=93&t=4

[15]   "Basic Research Needs for Solar Energy Utilization," U.S. Department of Energy2005.

[16]   V. Smil. 2006, *Energy at the Crossroads*. Available: http://www.vaclavsmil.com/wp-
        content/uploads/docs/smil-article-2006-oecd.pdf

[17]   A. V. Herzog, *et al.*, "Renewable Energy Sources," University of California, Berkeley.

[18]   *International Energy Statistics - Total Energy*. Available:
        http://www.eia.gov/cfapps/ipdbproject/IEDIndex3.cfm?tid=44&pid=44&aid=2

[19]   *International Energy Statistics - Electricity*. Available:
        http://www.eia.gov/cfapps/ipdbproject/IEDIndex3.cfm?tid=2&pid=2&aid=2

[20]   C. L. Archer and M. Z. Jacobson, "Evaluation of global wind power," *Journal of Geophysical
        Research* vol. 110, 2005.

[21]   J. A. Turner, "A realizable renewable energy future," *Science*, vol. 285, pp. 687-689, 1999.

[22]   Bundesnetzagentur. *Photovoltaikanlagen: Datenmeldungen sowie EEG-Vergütungssätze*.
        Available:
        http://www.bundesnetzagentur.de/DE/Sachgebiete/ElektrizitaetundGas/Unternehmen_Institutione
        n/ErneuerbareEnergien/Photovoltaik/DatenMeldgn_EEG-VergSaetze/DatenMeldgn_EEG-
        VergSaetze_node.html

[23]   *NREL: Dynamic Maps, GIS Data, & Analysis Tools*. Available:
        http://www.nrel.gov/gis/solar.html

[24]   K. Ardani and R. Margolis, "Solar Market Trends Report," U.S. National Renewable Energy
        Laboratory2010.

[25]   S. A. Kalogirou, "Solar thermal collectors and applications," *Progress in Energy and Combustion
        Science*, vol. 30, pp. 231-295, 2004.

[26]   *Solar Power Tower*. Available:
         http://assets.careerspot.com.au/files/news/Solar%20Power%20Tower.jpg
[27]   *Solartechnik2*. Available:
         http://www.dlr.de/dlr/en/Portaldata/1/Resources/bilder/portal/portal_2011_2/solartechnik2.jpg
[28]   *Stirling Energy Systems*. Available:
         http://theirearth.com/uploads/news/1626016863_stirling_energy_systems_(new_technology).jpg
[29]   G. A. Heath and J. J. B. III, "Meta-Analysis of Estimates of Life Cycle Greenhouse Gas
         Emissions from Concentrating Solar Power," U.S. National Renewable Energy Laboratory2011.
[30]   *Wholesale electricity and natural gas market data*. Available:
         http://www.eia.gov/electricity/wholesale/
[31]   *SunShot Concentrating Solar Power Program*. Available:
         http://energy.gov/sites/prod/files/2014/02/f7/sunshot_csp_poster.pdf
[32]   D. M. Chapin, *et al.*, "A new silicon p-n junction photocell for converting solar radiation into
         electrical power," *Journal of Applied Physics*, vol. 25, pp. 676-677, 1954.
[33]   *Best Research-Cell Efficiencies*. Available: http://www.nrel.gov/ncpv/images/efficiency_chart.jpg
[34]   M. Green, *Third generation photovoltaics: advanced solar energy conversion*. Berlin: Springer
         Verlag, 2003.
[35]   *Photovoltaics*. Available: http://energy.gov/eere/sunshot/photovoltaics
[36]   O. E. Semonin, *et al.*, "Peak External Photocurrent Quantum Efficiency Exceeding 100% via
         MEG in a Quantum Dot Solar Cell," *Science*, vol. 334, pp. 1530-1533, Dec 16 2011.
[37]   X. Huang, *et al.*, "Enhancing solar cell efficiency: the search for luminescent materials as spectral
         converters," *Chemical Society Reviews*, vol. 42, pp. 173-201, 2013 2013.
[38]   J. Tang and E. H. Sargent, "Infrared Colloidal Quantum Dots for Photovoltaics: Fundamentals
         and Recent Progress," *Advanced Materials*, vol. 23, pp. 12-29, Jan 4 2011.
[39]   L. E. Brus, "ELECTRON ELECTRON AND ELECTRON-HOLE INTERACTIONS IN SMALL
         SEMICONDUCTOR CRYSTALLITES - THE SIZE DEPENDENCE OF THE LOWEST
         EXCITED ELECTRONIC STATE," *Journal of Chemical Physics*, vol. 80, pp. 4403-4409, 1984
         1984.
[40]   L. E. Brus, "A SIMPLE-MODEL FOR THE IONIZATION-POTENTIAL, ELECTRON-
         AFFINITY, AND AQUEOUS REDOX POTENTIALS OF SMALL SEMICONDUCTOR
         CRYSTALLITES," *Journal of Chemical Physics*, vol. 79, pp. 5566-5571, 1983 1983.
[41]   S. Banerjee and B. Streetman, *Solid State Electronic Devices*, 7th ed.: Prentice Hall, 2014.
[42]   J. Tang, *et al.*, "Quantum Dot Photovoltaics in the Extreme Quantum Confinement Regime: The
         Surface-Chemical Origins of Exceptional Air- and Light-Stability," *Acs Nano*, vol. 4, pp. 869-
         878, Feb 2010.
[43]   Q. Dai, *et al.*, "Size-Dependent Composition and Molar Extinction Coefficient of PbSe
         Semiconductor Nanocrystals," *Acs Nano*, vol. 3, pp. 1518-1524, Jun 2009.
[44]   I. Moreels, *et al.*, "Size-Dependent Optical Properties of Colloidal PbS Quantum Dots," *Acs
         Nano*, vol. 3, pp. 3023-3030, Oct 2009.
[45]   I. Moreels, *et al.*, "Surface Chemistry of Colloidal PbSe Nanocrystals," *Journal of the American
         Chemical Society*, vol. 130, pp. 15081-15086, Nov 12 2008.
[46]   N. B. Pendyala and K. S. R. K. Rao, "Identification of surface states in PbS quantum dots by
         temperature dependent photoluminescence," *Journal of Luminescence*, vol. 128, pp. 1826-1830,
         Nov 2008.
[47]   G. Konstantatos, *et al.*, "Engineering the temporal response of photoconductive photodetectors
         via selective introduction of surface trap states," *Nano Letters*, vol. 8, pp. 1446-1450, May 2008.
[48]   D. A. R. Barkhouse, *et al.*, "Thiols Passivate Recombination Centers in Colloidal Quantum Dots
         Leading to Enhanced Photovoltaic Device Efficiency," *Acs Nano*, vol. 2, pp. 2356-2362, Nov
         2008.
[49]   J. M. Luther, *et al.*, "Structural, optical and electrical properties of self-assembled films of PbSe
         nanocrystals treated with 1,2-ethanedithiol," *Acs Nano*, vol. 2, pp. 271-280, Feb 2008.

[50]   Y. Liu, *et al.*, "Dependence of Carrier Mobility on Nanocrystal Size and Ligand Length in PbSe Nanocrystal Solids," *Nano Letters*, vol. 10, pp. 1960-1969, May 2010.

[51]   W. K. Bae, *et al.*, "Highly Effective Surface Passivation of PbSe Quantum Dots through Reaction with Molecular Chlorine," *Journal of the American Chemical Society*, vol. 134, pp. 20160-20168, Dec 12 2012.

[52]   J. Tang, *et al.*, "Colloidal-quantum-dot photovoltaics using atomic-ligand passivation," *Nature Materials*, vol. 10, pp. 765-771, Oct 2011.

[53]   A. H. Ip, *et al.*, "Hybrid passivated colloidal quantum dot solids," *Nature Nanotechnology*, vol. 7, pp. 577-582, Sep 2012.

[54]   J. M. Luther, *et al.*, "Schottky Solar Cells Based on Colloidal Nanocrystal Films," *Nano Letters*, vol. 8, pp. 3488-3492, Oct 2008.

[55]   K. W. Johnston, *et al.*, "Efficient Schottky-quantum-dot photovoltaics: The roles of depletion, drift, and diffusion," *Applied Physics Letters*, vol. 92, Mar 24 2008.

[56]   W. Ma, *et al.*, "Photovoltaic Performance of Ultrasmall PbSe Quantum Dots," *Acs Nano*, vol. 5, pp. 8140-8147, Oct 2011.

[57]   L.-Y. Chang, *et al.*, "Low-Temperature Solution-Processed Solar Cells Based on PbS Colloidal Quantum Dot/CdS Heterojunctions," *Nano Letters*, vol. 13, pp. 994-999, Mar 2013.

[58]   A. G. Pattantyus-Abraham, *et al.*, "Depleted-Heterojunction Colloidal Quantum Dot Solar Cells," *Acs Nano*, vol. 4, pp. 3374-3380, Jun 2010.

[59]   J. M. Luther, *et al.*, "Stability Assessment on a 3% Bilayer PbS/ZnO Quantum Dot Heterojunction Solar Cell," *Advanced Materials*, vol. 22, pp. 3704-+, Sep 1 2010.

[60]   X. Lan, *et al.*, "Charge-extraction strategies for colloidal quantum dot photovoltaics," *Nat Mater*, vol. 13, pp. 233-240, 2014.

[61]   G. I. Koleilat, *et al.*, "Efficient, stable infrared photovoltaics based on solution-cast colloidal quantum dots," *Acs Nano*, vol. 2, pp. 833-840, May 2008.

[62]   J. Jean, *et al.*, "ZnO Nanowire Arrays for Enhanced Photocurrent in PbS Quantum Dot Solar Cells," *Advanced Materials*, vol. 25, pp. 2790-2796, May 28 2013.

[63]   E. H. Sargent, "Colloidal quantum dot solar cells," *Nature Photonics*, vol. 6, pp. 133-135, Mar 2012.

[64]   S. H. Park, *et al.*, "Bulk heterojunction solar cells with internal quantum efficiency approaching 100%," *Nature Photonics*, vol. 3, pp. 297-U5, May 2009.

[65]   P. Peumans, *et al.*, "Efficient bulk heterojunction photovoltaic cells using small-molecular-weight organic thin films," *Nature*, vol. 425, pp. 158-162, 2003.

[66]   K. S. Leschkies, *et al.*, "Nanowire-quantum-dot solar cells and the influence of nanowire length on the charge collection efficiency," *Applied Physics Letters*, vol. 95, Nov 9 2009.

[67]   D. A. R. Barkhouse, *et al.*, "Depleted Bulk Heterojunction Colloidal Quantum Dot Photovoltaics," *Advanced Materials*, vol. 23, pp. 3134-+, Jul 26 2011.

[68]   I. J. Kramer, *et al.*, "Ordered Nanopillar Structured Electrodes for Depleted Bulk Heterojunction Colloidal Quantum Dot Solar Cells," *Advanced Materials*, vol. 24, pp. 2315-2319, May 2 2012.

[69]   X. Lan, *et al.*, "Self-Assembled, Nanowire Network Electrodes for Depleted Bulk Heterojunction Solar Cells," *Advanced Materials*, vol. 25, pp. 1769-1773, Mar 25 2013.

[70]   H. Wang, *et al.*, "PbS-Quantum-Dot-Based Heterojunction Solar Cells Utilizing ZnO Nanowires for High External Quantum Efficiency in the Near-Infrared Region," *Journal of Physical Chemistry Letters*, vol. 4, pp. 2455-2460, Aug 1 2013.

[71]   A. K. Rath, *et al.*, "Solution-processed inorganic bulk nano-heterojunctions and their application to solar cells," *Nature Photonics*, vol. 6, pp. 529-534, Aug 2012.

[72]   H. Liu, *et al.*, "Electron Acceptor Materials Engineering in Colloidal Quantum Dot Solar Cells," *Advanced Materials*, vol. 23, pp. 3832-+, Sep 1 2011.

[73]   P. Maraghechi, *et al.*, "The Donor-Supply Electrode Enhances Performance in Colloidal Quantum Dot Solar Cells," *Acs Nano*, vol. 7, pp. 6111-6116, Jul 2013.

[74] J. Gao, et al., "n-Type Transition Metal Oxide as a Hole Extraction Layer in PbS Quantum Dot Solar Cells," *Nano Letters,* vol. 11, pp. 3263-3266, Aug 2011.

[75] P. R. Brown, et al., "Improved Current Extraction from ZnO/PbS Quantum Dot Heterojunction Photovoltaics Using a MoO3 Interfacial Layer," *Nano Letters,* vol. 11, pp. 2955-2961, Jul 2011.

[76] M. A. Hines and G. D. Scholes, "Colloidal PbS nanocrystals with size-tunable near-infrared emission: Observation of post-synthesis self-narrowing of the particle size distribution," *Advanced Materials,* vol. 15, pp. 1844-1849, Nov 2003.

[77] J. Tang, et al., "Quantum Dot Photovoltaics in the Extreme Quantum Confinement Regime: The Surface-Chemical Origins of Exceptional Air- and Light-Stability," *Acs Nano,* vol. 4, pp. 869-878, Feb 2010.

[78] C. Y. Kuo, et al., "Ligands affect the crystal structure and photovoltaic performance of thin films of PbSe quantum dots," *Journal of Materials Chemistry,* vol. 21, pp. 11605-11612, 2011.

[79] P. D. Cozzoli, et al., "Low-temperature synthesis of soluble and processable organic-capped anatase TiO2 nanorods," *Journal of the American Chemical Society,* vol. 125, pp. 14539-14548, Nov 2003.

[80] C. T. Dinh, et al., "Shape-Controlled Synthesis of Highly Crystalline Titania Nanocrystals," *Acs Nano,* vol. 3, pp. 3737-3743, Nov 2009.

[81] R. Buonsanti, et al., "Hyperbranched Anatase TiO2 Nanocrystals: Nonaqueous Synthesis, Growth Mechanism, and Exploitation in Dye-Sensitized Solar Cells," *Journal of the American Chemical Society,* vol. 133, pp. 19216-19239, Nov 2011.

[82] H. Y. Sohn and C. Moreland, "The effect of particle size distribution on packing density," *The Canadian Journal of Chemical Engineering,* vol. 46, pp. 162-167, 1968.

[83] K. W. Desmond and E. R. Weeks, "Influence of particle size distribution on random close packing of spheres," *Physical Review E,* vol. 90, p. 022204, 2014.

[84] D. O. Scanlon, et al., "Band alignment of rutile and anatase TiO2," *Nat Mater,* vol. 12, pp. 798-801, 2013.

[85] N. D. Treat and M. L. Chabinyc, "Phase Separation in Bulk Heterojunctions of Semiconducting Polymers and Fullerenes for Photovoltaics," *Annual Review of Physical Chemistry, Vol 65,* vol. 65, pp. 59-81, 2014.

[86] D. Kim, et al., "Impact of Stoichiometry on the Electronic Structure of PbS Quantum Dots," *Physical Review Letters,* vol. 110, May 2013.

[87] *Nanoparticle Technology Handbook,* Second ed.: Elsevier, 2012.

[88] M. Gratzel, "The light and shade of perovskite solar cells," *Nat Mater,* vol. 13, pp. 838-842, 2014.

[89] M. D. McGehee, "Perovskite solar cells: Continuing to soar," *Nat Mater,* vol. 13, pp. 845-846, 2014.

[90] M. A. Green, et al., "The emergence of perovskite solar cells," *Nat Photon,* vol. 8, pp. 506-514, 2014.

[91] J.-H. Im, et al., "Growth of CH3NH3PbI3 cuboids with controlled size for high-efficiency perovskite solar cells," *Nat Nano,* vol. 9, pp. 927-932, 2014.

[92] W. H. Press, "What's So Special About Science (And How Much Should We Spend on It?)," *Science,* vol. 342, pp. 817-822, November 15, 2013 2013.